NORTHWESTERN UNIVERSITY

The Actin-Based Motility Machinery of Neuronal Growth Cone Veils.

A DISSERTATION

SUBMITTED TO THE GRADUATE SCHOOL

IN PARTIAL FULFILLMENT OF THE REQUIREMENTS

for the degree

DOCTOR OF PHILOSOPHY

Field of CELL AND MOLECULAR BIOLOGY

BY

Anne Katherine Mongiu

CHICAGO, ILLINOIS

December 2007

ABSTRACT

The Actin-Based Motility Machinery of Neuronal Growth Cone Veils.

Anne K. Mongiu

The growth cone is a highly specialized motile structure with a distinctive and dynamically variable morphology. Current understanding of actin-based protrusive motility has been formulated in terms of the dendritic nucleation/array treadmilling model for lamellipodial protrusion and the convergent-elongation model for filopodial protrusion, that were based upon results obtained primarily with non-neuronal motile cells. A major question in cellular neurobiology is whether the same basic mechanisms operate in the neuronal growth cone or whether they have undergone significant modification. I hypothesized that a treadmilling dendritic network, similar to that observed in other motile cells, would support normal growth cone motility. Using correlative phase and platinum replica electron microscopy I correlated directional motility in individual chick dorsal root ganglion growth cone veils to the underlying actin ultrastructure. Protruding veils appeared to contain dendritic network similar in appearance to that found in motile fibroblasts, and the network stained positively for the actin nucleator Arp2/3. Retracting veils, by contrast, contained few actin filaments; suggesting a rapid and aggressive loss of actin filaments accompanies retrograde flow

of F-actin. The edge of retracting veils is lined with actin bundles oriented parallel to the membrane. The mechanism of bundling is unknown, but preliminary observations suggest a role for myosin II. Analysis of neuronal filopodia revealed that they support complex filopodia-veil dynamics, not previously reported in fibroblasts, indicating that neuronal filopodia may possess unique functional capabilities that should be evaluated further. Studies of targeted Arp2/3 depletion, performed to evaluate its role in growth cone motility, demonstrated an inconsistent knockdown phenotype. From this we concluded that while normal motility appeared supported by a dendritic network, other redundant pathways might also support growth cone motility.

ACKNOWLEDGEMENTS

Dr. Bartles & Dr. Taylor for helping with the paper, and for overseeing the project as it approached the end.
Dr. Smith & Dr. Luxton, for techniques related to chick DRGs, and for generous use of your lab and equipment.
Dr. Jones for insightful comments and questions.
Dr. Goldman & Dr. Helfand, for help with PC-12 cell lines and for generous use of equipment.
Dr. Chaga, for help with the correlative electron microscopy.
Dr. Weitzke
Dr. Kojima
Dr. Borisy

LIST OF ABBREVIATIONS:

DORSAL ROOT GANGLION	DRG
ARP2/3 COMPLEX	ARP2/3
ELECTRON MICROSCOPY	EM
LIGHT MICROSCOPY	LM
CORRELATIVE LIGHT AND ELECTRON MICROSCOPY	COREM
WISCOTT-ALDRICH SYNDROME PROTEIN	WASP
SHORT INTERFERING RNA	SIRNA

DEDICATION

To my mother, Elaine Mongiu, you never cease to inspire me with your strength, calmness, and courage. For my father, John Mongiu, who taught me to always strive for excellence.

To my husband, Daniel, for always believing in me.

In memory of Tressa Ursetti and Timothy Michael Maron. I would never have dreamed high enough without either of you. Thank you for your love and support.

TABLE OF CONTENTS.

TABLE OF FIGURES.

TABLE OF TABLES.

CHAPTER 1

INTRODUCTION

1.1 General Introduction:

Cell motility is intrinsic to all living organisms, functions at the cellular level, and ultimately influences the structure and function of the whole organism. It fuels numerous disparate processes, including, but not limited to, embryogenesis, growth, normal physiologic functions, and disease. Motility is driven by the nano-machinery of the cell that is referred to as the cytoskeleton. In most eukaryotic cells, the cytoskeleton is comprised of three families of cytoskeletal elements of increasing size: the actin-based microfilaments, the intermediate filaments, and the microtubules.

Motility is especially important in neuroscience: from the millions of miles of axonal wiring laid out by growth cones to the synaptic remodeling that underlies memory and learning. The growth cone is a highly specialized motile structure with a distinctive and dynamically variable morphology. The anatomy of the growth cone consists of a microtubule dense central region and an actin rich peripheral domain, with a transitional region in the middle where the two interact. The peripheral domain is composed of parallel bundled actin filaments in filopodia and a thin 'veil-like' structure filled with a poorly defined actin meshwork.

Current understanding of actin-based protrusive motility has been formulated in terms of two models: the dendritic nucleation/array treadmilling model for lamellipodial protrusion and the convergent-elongation model for filopodial protrusion. These models have been developed based upon results obtained primarily with non-neuronal motile cells. A major question in the cellular neurobiology area is whether the same basic mechanisms operate in the neuronal growth cone or whether they have undergone

significant modification. Upstream signaling, substrate interactions and regulatory mechanisms serve to modify the morphology of the growth cone, but they do so ultimately by modulating the molecules that remodel the cytoskeleton. The objective of this thesis was to characterize the actin-based cytoskeleton of the growth cone and to evaluate how it relates to currently accepted models of motility.

1.2 Organization of the actin cytoskeleton in the motility machinery

Motion is important to different cell types for many different reasons. Most motile cells exhibit protrusive motility that is driven by polymerization of the actin cytoskeleton (Pollard et al., 2000). The protrusive organelles driven by the actin polymerization can be roughly grouped into two categories: the lamellipodia and the filopodia. Lamellipodium is a cell biology term derived from the Latin words for “sheet foot”. Abercrombie coined the term while studying chick heart fibroblasts in culture (Abercrombie et al., 1970). By his definition lamellipodia were “thin, sheet-like, mobile, commonly transitory projections from the cell” (Abercrombie et al., 1971). By rudimentary EM, Abercrombie further described the lamellipodia as having “a characteristic thickness of 110 to 160 nm, and contain a fibrous cytoplasm devoid of the polysomes and vacuoles found in the leading lamella from which they spring” (Abercrombie et al., 1971). The definition of the lamellipodium has continued to evolve after Abercrombie. In motile fibroblasts and keratocytes, this definition has been expanded to include specific biomarkers, kinetics, and characteristic ultrastructural organization. The ultrastructure of the lamellipodium is characterized by the dendritic

array of actin filaments nucleated by the biomarker Arp2/3 complex (Svitkina and Borisy, 1999). Speckle analysis of GFP actin demonstrated rapid turnover of actin within the lamellipodium, while polymerization and depolymerization occurred with almost constant kinetics throughout the lamellipodium (except for a 1.3-1.6 fold increase in polymerization in the most distal 1 μm of the lamellipodium) (Watanabe and Mitchison, 2002). Actin polymerization occurs from the barbed, or growing, ends of the network that are oriented towards the plasma membrane (Tilney et al., 1981). Filopodia, meaning “spike foot”, are long thin spikes that protrude from the cell and are comprised of tightly bundled parallel actin filaments (Borisy and Svitkina, 2000). Most cells use a combination of these two forms for motility, though some favor one more exclusively than the other.

The Dendritic Nucleation - Array Treadmilling Model

The dendritic nucleation-array treadmilling model is a conceptual framework that was proposed to explain the protrusive motion of the lamellipodia in a manner consistent with published observations and known molecular components (Figure 1) (Pollard and Borisy, 2003). Broadly, the model functionally describes lamellipodial movement as a steady-state treadmilling that arises from an organized actin network that branches and polymerizes at the free barbed ends, while being depolymerized at the pointed ends. The model arose from correlative light and electron microscopy (CorEM) of keratocyte and fibroblast lamellipodia (Svitkina and Borisy, 1999; Svitkina et al., 1997), *in vitro*

Figure 1 The Array-Treadmilling Model for Lamellipodial Protrusion

The lamellipodia is an actin based protrusive organelle filled with an orthogonal filament array. This model proposes that new actin filaments are nucleated by the Arp2/3 complex at 70 degrees from the mother filament. Filaments that protrude away from the membrane are capped, preventing excessive non-productive polymerization. Actin monomers add to the barbed ends of the filaments at the leading edge of the array. Depolymerization of the array spontaneously occurs at the pointed end and is accelerated by ADF/cofilin.

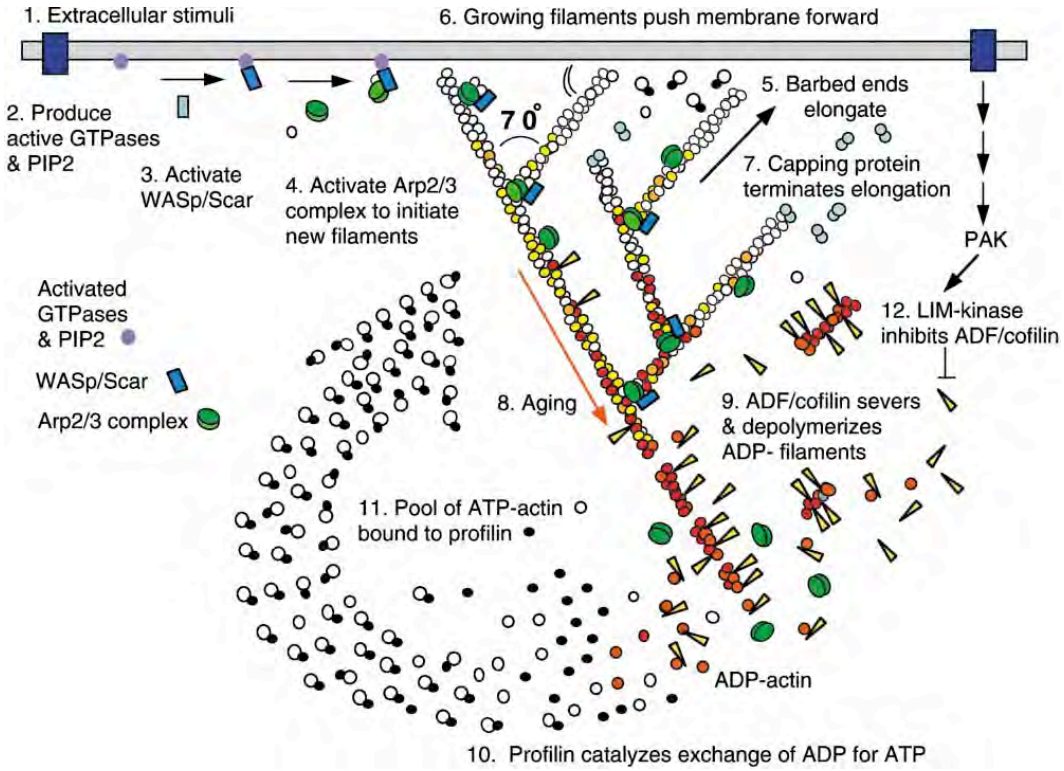

(Pollard and Borisy, 2003)

biochemical assays (Mullins et al., 1998), and mathematical modeling (Mogilner and Oster, 1996).

The lamellipodium contains a branched array of actin filaments that grow fastest from the their barbed ends, which are predominantly oriented towards the plasma membrane (Small et al., 1978). Accordingly, most actin polymerization occurs at the most distal 1μm of the cell, known as the extreme leading edge. New branches are nucleated off of the sides of pre-existing actin filaments at approximately 70˚ angles with their pointed ends capped and protected from depolymerization by the nucleator. Free barbed ends can then elongate for a short period of time, pushing the membrane forward, until they are capped and decommissioned from further polymerization. Capping serves the dual purpose of keeping filaments short for effective pushing, while also limiting the absolute number of free barbed ends produced. De-polymerization occurs from the pointed ends of filaments in the rear of the array, and allows recycling of the network to fuel further polymerization (Svitkina and Borisy, 1999).

1.3 Introduction to Known Parameters of Form and Key Molecular Players

The treadmilling model defines cellular form as a coordinated function of the processes of branching, capping, and bundling of the actin cytoskeleton. A branched actin network lies at the core of the dendritic nucleation/array treadmilling model for lamellipodial protrusion. The Arp2/3 complex has been identified as the major nucleator of the filament branches in this model (Mullins et al., 1998; Svitkina and Borisy, 1999). Rapid capping of the free barbed ends of the actin network is necessary to maintain filaments short enough to efficiently push the membrane forward, while preventing uncontrolled

polymerization that would critically deplete the free actin monomer pool (Pollard et al., 2000). Capping protein (CP) is the major barbed-end capper that is known, and has been shown to be critical in recapitulating actin based motility in an in vitro system (Loisel et al., 1999). Work performed in our laboratory showed that it may also function as a molecular regulator of the balance between lamellipodia and filopodia formation (Mejillano et al., 2004). Bundling of actin filaments from a dendritic array into tight parallel bundles is necessary for filopodia formation. Fascin is an actin bundling protein that has been implicated as the primary bundler in filopodia, and is necessary for filopodial formation (Svitkina et al., 2003).

1.4 The Arp2/3 complex is the primary nucleator of actin filaments in the dendritic network of motile cells

Arp 2/3 is a 7 subunit complex that was originally purified from *Acanthamoeba* (Machesky et al., 1994). The complex consists of two actin related proteins, Arp2 and Arp3, along with 5 novel proteins: with standard nomenclature ARPC1-5 (mammalian homologs are p41-Arc, p34-Arc, p21-Arc, p20-Arc, and p16-Arc respectively) (Machesky et al., 1994; Machesky et al., 1997). The complex is thought to be as old as actin, and is conserved in its entirety from yeast to human (Ma et al., 1998; Machesky et al., 1994; Machesky et al., 1997; Welch et al., 1997; Winter et al., 1997). Deletion of a single subunit in yeast is sufficient to cause lethality or severe growth impairment (Winter et al., 1997; Winter et al., 1999). This is supported by *in vitro* data showing that only three combinations of partial complexes (missing either p21, p16 and p41, or Arp3

and p21) can assemble, and only the first two possess any detectable nucleating activity (Gournier et al., 2001).

The complex was first visualized at the leading edge of crawling cells, in regions of active actin polymerization (Machesky et al., 1997; Svitkina and Borisy, 1999; Welch et al., 1997). It was further localized by immunoEM and cryo-EM reconstruction to the crotch of Y junctions formed between branched actin filaments (Svitkina and Borisy, 1999; Volkmann et al., 2001). Arp2/3 is thought to bind to the side of an actin filament, and to nucleate a new actin filament at a 70˚ angle from the "mother" filament (Mullins et al., 1998; Svitkina and Borisy, 1999). Alone, the complex is incapable of nucleating actin filaments, and requires activation from external cofactors (Machesky and Insall, 1998). Identified activators or nucleation promoting factors (NPF's) include: *Listeria monocytogenes* Act A protein, WASp/N-WASp/Scar (Wiscott-Aldrich Syndrome protein), cortactin, Abp1p, and yeast type I myosins (Higgs, 2001; Jeng and Welch, 2001). The WASp family proteins are the best characterized. An actin filament is also needed for activation. Essentially, the actin filament serves as a co-activator and, together with a WASp family member, insures that the new filament forms as a branch on a pre-existing filament (Mullins et al., 1998; Svitkina and Borisy, 1999).

Models of the complex suggested by functional and genetic studies (Gournier et al., 2001; Volkmann et al., 2001; Winter et al., 1999) were consistent with the recently compiled crystal structure (Robinson et al., 2001). The p20-Arc and p34-Arc subunits have been shown to form the core of the complex, with p34 binding to the side of the actin filament (Borths and Welch, 2002; Gournier et al., 2001; Winter et al., 1999). Arp2

and Arp3 are thought to form the nucleation interface, and p41, p16, and p21 are thought to participate in the activation of the complex (Gournier et al., 2001).

1.5 Other Actin Nucleators & Cross-linkers

The array treadmilling model described above was published by our laboratory in 1999 based upon observations made in motile fibroblasts and keratocytes, and utilized the major cytoskeletal proteins known at that time. It relied upon the Arp2/3 complex as the sole actin branch nucleator. In the time that has since elapsed, two new classes of actin nucleators have been widely studied and published: the formin family proteins and the Drosophila spire proteins. Additionally, it is not entirely understood how the actin filament cross-linking protein, filamin, fits into this model (Figure 2).

Formins – Barbed End Nucleators of Straight Filaments

Formins were first identified in the murine *limb deformity* gene, whose mutation led to limb & kidney formation defects (Kleinebrecht et al., 1982). They were later found to nucleate actin filaments de novo from actin monomers when provided with the actin filament carrier protein, profilin. The formins comprise a diverse family, conserved from slime mold and fruit flies to humans (Wallar and Alberts, 2003). There are nine known mammalian family members, some with several splice variants, and complicated, sometimes overlapping, functions. The Diaphanous-related formins constitute one subset of the formin family, with a regulatory Rho GTPase binding domain. Binding of Rho-family GTPases to N-terminus is thought to relax conformational auto-inhibition of

the DAD (Dia-autoregulatory domain) (Evangelista et al., 2003). However, other formin family members, such as formin-1, are MAP kinase substrates, similar to the Spire family of proteins.

Almost all formins contain two highly conserved domains: the Formin Homology 2 domain (FH2) that binds to the barbed end and can nucleate filaments *in vitro,* and the Formin Homology 1 (FH1) domain that binds profilin (Zigmond, 2004). Some formins also contain FH3 or PDZ domains that aid in cellular localization (Evangelista et al., 2003). Formins form dimers, and *in vitro* the FH1-FH2 domain acts as a leaky cap on the barbed ends of actin filaments, with the cap competitively preventing barbed end cappers from binding and terminating filament growth (Figure 2B). One model proposes that formins 'walk' processively up the growing filament, allowing actin monomers to add to the barbed end of the growing filament (Zigmond et al., 2003). Importantly, this leads to the formation of straight, unbranched actin filaments, such as yeast actin cables, contractile rings, and mammalian stress fibers. The nature of these structures, and the ability to be attached to membranes is important for sustaining tension and aiding in contraction along with the myosin family of motor proteins (Evangelista et al., 2003; Wallar and Alberts, 2003). In addition to the original limb/organ morphogenesis, Formins have been shown to play important roles in cell polarity, cytokinesis, and sterocilia and acrosome formation (Zigmond, 2004).

Figure 2 Key Actin Nucleators and Cross-Linkers

A. The Arp2/3 complex is a highly conserved seven subunit protein complex that binds to the side of pre-existing actin filaments and nucleates new actin filaments at approximately 70˚ angle off the mother filament. It is the only nucleator currently accounted for in the array-treadmilling model of lamellipodial protrusion, and the only one known to create branched filaments. (Evangelista et al., 2003) B. The formin family of proteins, involved in limb morphogenesis, was recently shown to be capable of nucleating straight filaments. Formins bind to the barbed end of actin filaments and allow monomer addition, while protecting the barbed end from capping. (Evangelista et al., 2003) C. The Spire family, like Arp2/3, nucleates filaments by binding to the pointed end. However, to date Spire has only been shown to form straight, unbranched filaments. (Baum and Kunda, 2005) D. Filamin is a large actin binding protein that has been shown to cross-link actin filaments, but has no known nucleating activity. Cross-linking creates X, Y, and T shaped junctions when viewed from above. Found in the lamellipodia, there are conflicting results as to whether it is localized in the extreme edge (Flanagan et al., 2001; Stossel et al., 2001).

Key Actin Nucleators & Crosslinkers

A.	Arp2/3		•7 protein complex •binds pointed end •nucleates branched filaments at 70˚ from mother filament
B.	Formins		•dimer •binds barbed end •nucleates straight filaments
C.	Spire	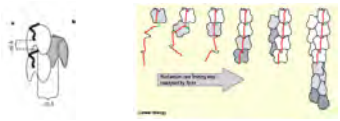	•single molecule •binds pointed end •nucleates straight filaments
D.	Filamin	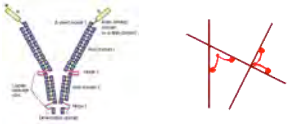	•dimer •crosslinks actin filaments •creates T, X, Y junctions

Spire Family – Pointed End Nucleators of Straight Filaments

In early 2005 the Spire family of Drosophila genes critical for embryo development was determined to define yet another novel class of actin nucleators (Quinlan et al., 2005). Spire genes have no sequence homology to either the Arp2/3 complex components or the formin family. They possess four Wasp Homology 2 domains (WH2). Such domains are reminiscent of those found in the Arp2/3 activator N-Wasp, and *in vitro* they are capable of blocking actin polymerization. Similar to Arp2/3, Spire binds to the pointed end of an actin filaments and initiates actin filament nucleation de novo (Figure 2C), and has been shown to be capable of nucleating actin dimers, trimers, or tetramers (Kerkhoff, 2006). Similar to formins, Spire has only been shown to generate straight, as opposed to branched filaments (Quinlan et al., 2005). It is highly conserved across the metazoans, though no orthologs have been identified yet in unicellular organisms. Mammalian homologs, Spir-1 and Spir-2 showed expression throughout the developing murine nervous system, including dorsal root ganglia (Schumacher et al., 2004). However, expression has been shown to be restricted to the CNS in the adult, with dense staining observed in the cerebellum, hippocampus, and dentate gyrus.

Filamin – A Crosslinker that Creates X, T, and Y Junctions

Filamin A (FLN-A, formerly ABP-280) is one of older known actin binding proteins that functions as a filament cross-linker (Hartwig and Shevlin, 1986). It was accidentally discovered by a group trying to purify a macrophage myosin that discovered an actin binding protein that produced an enormous precipitation of actin (Hartwig and Stossel,

1975; Stossel and Hartwig, 1975). It is a large protein of ~280 kDa that dimerizes at the C-terminus and binds actin at the N terminus. Filamin cross-links form X, Y, and/or T shaped junctions, and has been shown to abut the pointed end of actin molecules against existing filaments (Figure 2D) (Flanagan et al., 2001; Hartwig and Shevlin, 1986; Stossel et al., 2001; Stossel and Hartwig, 2003). Additionally, Filamins can bind the intracellular domains of proteins involved in connecting the extracellular matrix with the internal actin cytoskeleton, such as intergins, caveolin-1, TNF-α receptor. Human melanoma cells null for FLN-A are non-motile, and have lamella that are less orthogonally arranged than their motile counterparts with restored FLN-A expression (Flanagan et al., 2001). Clinically, expression of dysfunctional FLN-A in humans leads to ventricular heterotopia, with defective neuronal migration along radial glial cells, suggesting a specific role for filamin in neuronal migration and motility (Fox et al., 1998; Lambert de Rouvroit and Goffinet, 2001).

FLN-A is distributed throughout the cortical actin network. When filamin binds to actin filaments, they become locked together and are no longer able to slide past one another, lending strength to the network (Tseng et al., 2004). Some groups report localization at the leading edge (Flanagan et al., 2001), however, work performed in fibroblasts by our laboratory failed to localize filiamin at the leading edge (Svitkina and Borisy, 1999). FLN-A rarely colocalizes with Arp2/3 at the ultrastructural level when examined by dual immuno-electron staining, suggesting that the two proteins function independently (Flanagan et al., 2001). While both proteins likely function cooperatively

within protruding lamellipodia, no model currently accounts for both proteins in lamellipodial protrusion.

In Vitro Physical Properties of Crosslinks vs. Branches

As indicated above, filament branching and cross-linking initially appear to provide similar functional roles to the dendritic network, raising the question of whether they are interchangeable for array-treadmilling to occur. A series of elegant *in vitro* studies performed by the Wirtz laboratory on the gelation and deformability of actin networks in the presence of Arp 2/3, and cross-linkers filamin, fascin, and α-actinin sought to address this issue (Tseng et al., 2004). To protrude the leading edge, the actin network of a cell needs be sufficiently stiff and capable of recovering from elastic deformation, as well as being attached by some means to a substratum (Tseng and Wirtz, 2004). Wirtz et al. focused on two factors: the time to gelation of the actin network, and the final steady state values of elasticity imparted to the network. They found that Arp2/3 causes gelation of actin network over a much faster time scale than filamin, and that the resultant network was much more homogenous (Tseng and Wirtz, 2004). This is thought to result from the consistent angle of branching and the free sliding of the filaments, that allows filling of holes within the network (Tseng et al., 2004; Tseng and Wirtz, 2004). Conversely, cross-linking of actin filaments occurs at irregular angles, creating different junction shapes that actually slow the homogenization of the network (Tseng et al., 2004). While *in vitro* studies cannot duplicate the *in vivo* environment, the results suggests a system that experiences fast gelation of the network by Arp2/3 at the

leading edge followed by further network stabilization in the form of filamin crosslinks near the leading edge (Tseng et al., 2004; Tseng and Wirtz, 2004).

Many Nucleators Functioning within One Actin Network

The above review of actin new nucleators and a crosslinker shows an ever-increasing ensemble of proteins available to modify the shape of the actin networks within cells. Spire and Formin family proteins form straight actin filaments, and it is unlikely that they will replace the Arp 2/3 complex in creating a branched network. Their existence in the lamellipodia provides the cell with a diversity of options for generating protrusion within the dendritic network. Additionally, the formins may function to aid in contraction of the lamella rather than protrusion. Filamins co-exist within this model. In a three-dimensional scheme, cross-linking of actin filaments in this orthogonal array provides extra resilience to the cytoskeleton. It can provide an additional strength to the cortical actin meshwork, stabilizing the network and providing stability for the cell to maintain its shape over longer time scales

1.6 Myosins and the Motility Machinery

Myosins are a large family of force producing motor proteins that interact with actin in both muscle and non-muscle containing tissues. There are approximately 15 phylogenetic classes, and upwards of 40 myosin genes identified in mammals (Sellers, 2000). Yeast contain one myosin I, one myosin II, and two myosin V genes, which is thought to define a minimal set necessary for eukaryotic survival (Alberts, 2002; Sellers,

2000). Myosins consist of three main domains: a highly conserved head domain with actin and ATP binding domains, a neck domain for binding of regulatory light chains, and a tail region that can be broken into coiled-coil and tail, all of which determine interactions and thus functions of a particular myosin (Alberts, 2004). Myosins hydrolyze ATP to ADP in the 'power stroke' while remaining bound to actin, causing the net movement of the myosin in relation to the actin filament. In this case, the interaction of the tail domain determines the type of relative movement (Alberts, 2004). In dimerizing myosins such as myosin II, the tails interact with one another, forming bipolar filaments whose power stroke leads to contraction, either of muscle or actin networks. In the non-dimerizing myosins, such as myosin I, specific domains in the tail help localize the myosin to membranes or organelle membranes, leading to vesicle/organelle transport or plasma membrane localization (Alberts, 2002).

Myosin II is a conventional myosin, critical in muscle contraction, which has also been well studied in fibroblasts and is thought to play a role in the cell motility and retrograde flow observed in keratocytes (Svitkina et al., 1997; Verkhovsky and Borisy, 1993; Verkhovsky et al., 1995). Fish keratocytes have a stable shape and persistent, predictable motility that made them an ideal system to study the role of myosin II in cell motility. Myosin II and actin were observed to have inverse concentration profiles in these cells, with actin staining more brightly at the leading edge, and myosin more concentrated in front of the nucleus at the rear of the lamellum in parallel bundled actin filaments. Clusters of myosin II bipolar filaments appeared in the lamellum, and enlarged as the leading edge continued to protrude (Svitkina et al., 1997). Contraction

Figure 3 Myosin II Dynamic Network-Contraction Hypothesis

This schematic from Svitkina et al. depicts the dynamic network-contraction hypothesis showing myosin II dependent formation of parallel bundles (1997). In (a), myosin II bipolar filaments are shown attached to actin filaments at the rear of the lamellipodia. In (b), Contraction of myosin II leads to sliding of the filaments, that become oriented parallel to the leading edge. In (c) and (d), this generates a forward-directed force that can pull the rear edge of the cell forward, and induces forward rotation of the nucleus.

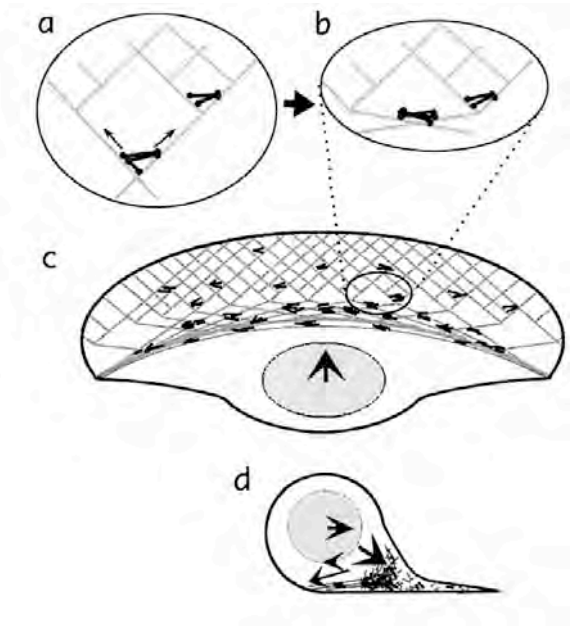

(Svitkina et al., 1997)

of these bipolar filaments at the rear, less dense region of the lamellum, proposed in the 'dynamic network contraction' model (Figure 3) would then cause actin filaments in the orthogonal array to be pulled into large bundles oriented parallel to the direction of protrusion (Svitkina et al., 1997). One important conclusion from these experiments is that myosin II can use uniformly oriented actin filaments in the dendritic array to generate force production in the direction of network orientation. In the absence of protrusion, as in tethered cells, the constant contraction of the myosin network against a fixed leading edge generates a retrograde flow (Svitkina et al., 1997).

1.7 Filopodia form by convergent elongation from a dendritic network.

Filopodia represent an alternate arrangement of actin filaments; parallel and bundled tightly together, as opposed to the dendritic branched network seen in the lamellipodium. This difference in organization raised the question of what relationship existed between filopodia and lamellipodia. Work published by our lab in 2003 proposed a convergent-elongation model whereby filopodia arise from gradual rearrangement of a dendritic actin network in fibroblasts (Svitkina et al., 2003) (Figure 4). This work established the dependence of filopodia initiation on a dendritic network.

CorEM was used to study early filopodial structures, referred to as lambda (λ) precursors, which had previously been shown by live cell imaging to mature into filopodia. The earliest λ precursors contained shorter branched filaments similar to those seen in the surrounding lamellipodium, while the later ones contained much longer filaments that could be traced back into the dendritic network (Svitkina et al.,

2003). This model proposes that the barbed ends of a few privileged filaments are protected from capping, possibly by VASP/Mena, and allowed to elongate in the dendritic network where they may collide with other similar filaments. A “tip complex” binds to the barbed ends, and keeps them bound together and in register with one another allowing for convergent elongation. Fascin is recruited after the initial λ precursor is formed, and the filaments subsequently become tightly bundled in the characteristic fashion seen in mature filopodia (Svitkina et al., 2003).

Fascin is the primary bundler of filopodia, and is necessary for filopodia formation in fibroblasts (Svitkina et al., 2003; Vignjevic et al., 2003). Targeted depletion of fascin using hairpin siRNA blocked formation of filopodia in melanoma cells, as did the inactive fascin mutant S39E (Vignjevic et al., 2006). Additionally, filopodia formation could not be rescued with over expression of other known actin bundlers such as alpha-actinin or espin (Vignjevic et al., 2006). This is consistent with previously published work that demonstrated that fascin was capable of creating filopodial “stars” in an *in vitro* system, while alpha-actinin could only form loose wavy bundles (Svitkina et al., 2003).

1.8 From the Cytoskeleton to the Growth Cone.

The above sections serve to introduce the actin cytoskeleton as it has been studied in motile fibroblasts and keratocytes. Similar studies have not been performed in primary neurons or neuronal cell lines. Primary neurons and neuronal cell lines present unique structural challenges to the question of cell motility. Neurons have a fixed cell body, containing a nucleus, that produces a neurite(s) led by a dynamic growth cone when

Figure 4 Convergent Elongation Model of Filopodial Formation

This model proposes that filopodia arise from privileged filaments in the lamellipodia that are protected from capping by a tip complex. (1) Some filaments in the network become associated with a molecule(s) from the “tip complex”, among them VASP, that protects them from capping. (2-3) Filaments with tip complexes align with one another in the network. These long filaments stand out from the network and appear as the lambda precursor of filopodia. (4) The actin bundling protein fascin is recruited to the lambda precursor where it rivets the actin filaments together. (5) Actin monomers are added to the barbed ends of the filaments in the filopodia as fascin continues adding to the filopodia keeping the filaments tightly bundled parallel to one another.

Convergent Elongation Model of Filopodia Formation

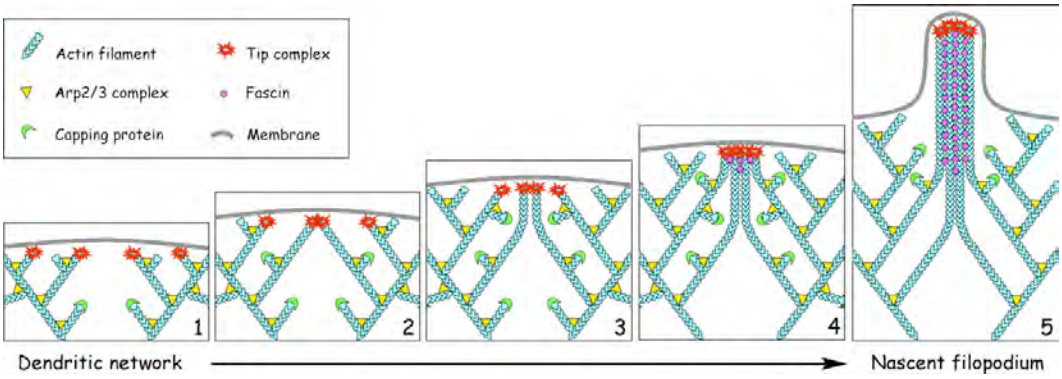

(Svitkina et al., 2003)

appropriately stimulated. This growth cone tows and guides the axon over enormous distances, to provide the wiring of the nervous system. In adulthood, continued remodeling of the cytoskeleton in dendrites has implications on how we learn and perceive the world around us (Luo, 2002). From this perspective, the growth cone presents unique cell biology questions that cannot be studied in other cell based biological systems. However, these questions have often been eclipsed by those concerning signaling and clinical disease. As such, some very basic questions of the motility machinery remain unanswered in the field, a few of which this thesis addresses.

Origin of the growth cone: discovery of the form and an inquiry into function.

The growth cone was first observed and consequently named by Santiago Ramon y Cajal in 1890 (Ramón y Cajal, 1890). Cajal visualized a club shaped protrusion emerging from an embryonic neuron in the spinal cord of silver-stained chick embryos (Figure 5). This simple observation and the following postulate that neurons existed as discrete entities that could form terminal connections with one another, would end an era that defined the nervous system as contiguous reticular network (Clarke and Jacyna, 1987). After nineteen years of work on the growth cone, Cajal summarized his findings:

> *"From the functional point of view the growth cone may be regarded as a sort of club or battering ram, endowed with exquisite chemical sensitivity, with rapid amoeboid movements, and with certain impulsive force, thanks to which it is able*

to proceed forward and overcome obstacles met in its way, forcing cellular interstices until it arrives at its destination" (Cajal, 1909)

What is known about the form and function of the neuronal growth cone today?

The dynamic shape of the growth cone has stimulated its own field of research. Grossly qualitative early studies determined that neurons are enriched with actin, which can consist of up to 5% of the total protein (Clark et al., 1983). The growth cone itself is particularly enriched with actin-based structures. Forscher's work on Aplysia led to the division of the growth cone into three structural domains: the microtubule rich central domain, the peripheral actin-rich domain, and the transitional domain situated in between the two, where there is overlap of microtubules and actin structures (Lin et al., 1996; Suter and Forscher, 2000). The actin-rich peripheral domain is composed primarily of a loose meshwork with long bundled radial spikes, (Lewis and Bridgman, 1992; Yamada et al., 1970; Yamada et al., 1971). It has been observed that microtubules occasionally penetrate into the peripheral zone, where they have been shown to interact with the filopodia (Schaefer et al., 2002).

The function of the growth cone, from the laying down of millions of miles of neuronal wiring, the eventual transformation into synaptic cleft, and the dendritic pruning that mediates synaptic plasticity of the nervous system, is dependent upon its dynamic motility machinery. An early question was whether axons elongated by cytoskeletal pushing or by being pulled out by applied tension from the growth cone. This was resolved by studies which demonstrated the ability of the growth cone to generate the

Figure 5 Cajal's Growth Cone

Representative drawings of chick neurons published by Santiago Ramon y Cajal. Neuroblasts of the chick embryo at the 60th hour of incubation. *A,* developing cone stained by the reduced silver nitrate method; *B,* cone impregnated by the Golgi method; *a,* primordial dendritic expansion. (Cajal, 1967)

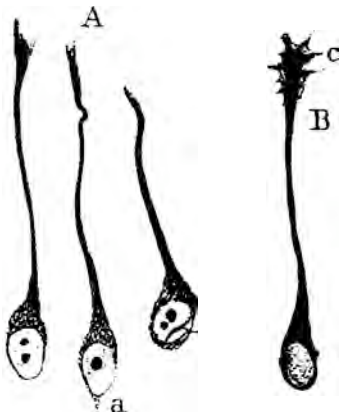

(Cajal, 1967)

tension needed to “tow” the axon (Bray, 1979; Bray, 1984; Heidemann et al., 1990; Lamoureux et al., 1989). Tension generation requires coupling of the actin cytoskeleton to a fixed substrate to provide a surface against which it can apply force. Substrate adhesion is mediated by cell adhesion molecules (CAM’s) and the proteins that tether the cytoskeleton to them (Suter and Forscher, 2000). Additionally, the actin cytoskeleton in the growth cone undergoes retrograde flow powered by myosin II motors that are integrated into the actin network (Bridgman et al., 2001; Forscher and Smith, 1988; Lin et al., 1996; Lin and Forscher, 1995). In keratocytes, contraction of this actin-myosin II network is proposed to drive the forward translocation of the cell body when there is strong substrate attachment (Svitkina et al., 1997). It has been suggested that a similar model may apply to the growth cone (Brown and Bridgman, 2003a).

Why is an investigation into the form of the motility machinery of the neuronal growth cone necessary?

On a basic level, this is an inquiry into the nature of form itself. Form is important from both a structural and functional perspective, as form is intimately connected with function. The ensemble of molecules constituting the motility machinery of the actin cytoskeleton has been rather extensively investigated in non-neuronal systems while their role in the form of the growth cone has been practically ignored until recently. All of which led us to ask broadly: how is the actin cytoskeleton of neuronal growth cones organized, and how does this organization influence growth cone motility?

CHAPTER 2

KINETIC-STRUCTURAL ANALYSIS OF NEURONAL GROWTH CONE VEIL MOTILITY

2.1 Introduction

The elongation and path finding of neurons depend upon the motility and sensory properties residing within a terminal specialization of cytoplasm known as the growth cone (Harrison, 1910; Landis, 1983). The motility behavior and cytomechanical properties of growth cones have been extensively investigated (Argiro et al., 1984; Heidemann et al., 1990; Steketee and Tosney, 2002; Suter and Forscher, 2000) and the molecular pathways by which they respond to environmental signals have been substantially unraveled (Gallo and Letourneau, 2004; Henley and Poo, 2004; Kalil and Dent, 2005; Luo, 2002). The relationship of lamellar extensions to shaft adhesions has been investigated (Steketee and Tosney, 2002). However, the supramolecular structure underlying dynamic growth cone motility has not been clearly delineated--especially in relationship to its temporal behavior. Understanding the structure and dynamics of the cytoskeletal apparatus within the growth cone is important for learning how the signaling pathways connect to the motility machinery, which in turn determines how growth cones are directed to developmental targets.

Growth cone advance has been described in terms of the behavior of two principal modes of actin filament organization,--lamellipodia and filopodia, which are frequently referred to as veils and microspikes, respectively, in the neuronal literature (Bray and Hollenbeck, 1988; Dent and Gertler, 2003). In general, net advance of the growth cone occurs by cycles of protrusion and retraction (Bray and Chapman, 1985) much as was originally described for fibroblasts (Abercrombie et al., 1970; Abercrombie et al., 1971). Investigations of the large growth cone of Aplysia neurons led to the

formulation that the growth cone could be divided into three structural domains: the microtubule rich central domain, the peripheral actin-rich domain, and the transitional domain situated in between the two, where there is overlap of microtubules and actin structures (Bridgman and Dailey, 1989; Forscher and Smith, 1988; Smith, 1988). The actin-rich peripheral domain contains the long actin filaments bundled into radial microspikes (filopodia) interspersed with a meshwork of veil or lamellipodial actin filaments (Lewis and Bridgman, 1992; Tosney and Wessells, 1983; Yamada et al., 1970; Yamada et al., 1971).

One question, which is as yet unanswered, is whether or not growth cone and fibroblast lamellipodia advance by similar or distinctive mechanisms. In non-neuronal cells, lamellipodial protrusion has been accounted for by an Arp2/3 dependent, dendritic nucleation/array treadmilling mechanism (Pollard and Borisy, 2003; Carlier, 2002). However, recent publications have called into question whether neuronal advance proceeds by an Arp2/3-dependent mechanism and have raised the possibility that additional Arp2/3 independent mechanisms may also exist. Genetic experiments generating null alleles for the Scar-Wasp-Arp pathway in the mushroom body neurons of Drosophila provided evidence that the Arp2/3 complex was not essential for axon growth in vivo (Ng and Luo, 2004). A similar conclusion was drawn for hippocampal neurons in culture in which Arp2/3 function had been diminished by expression of a dominant negative construct (Strasser et al., 2004). In both studies, although axon outgrowth occurred, pathfinding was aberrant.

The conclusion that the Arp2/3 complex is not essential for axon outgrowth is consistent with an older literature demonstrating that, under sufficiently adhesive conditions, actin polymerization itself is not essential for neurite outgrowth (Marsh and Letourneau, 1984). Further, path-finding in situ was disoriented in growth cones that had been subjected to cytochalasin treatment (Bentley and Toroian-Raymond, 1986; Chien et al., 1993). Although the focus of these studies was depletion of filopodia, the cytochalasin treatment employed would have inhibited barbed-end actin polymerization generally.

The role of the Arp 2/3 complex in protrusive motility has also been subject to re-evaluation in non-neuronal cells. Several reports demonstrated that Arp depletion blocked lamellipodia and invadipodia formation (Harborth et al., 2001; Rogers et al., 2003; Yamaguchi et al., 2005), thus confirming the importance of Arp 2/3 in protrusion. However, other studies interfering with Arp function (Di Nardo et al., 2005; Gupton et al., 2005; Ng and Luo, 2004; Strasser et al., 2004) have reported continued motility, thus suggesting the existence of Arp2/3-independent mechanisms of protrusion. Finally, recent literature has identified actin nucleators other than Arp2/3,--namely, formins (Evangelista et al., 2003; Kovar, 2006; Zigmond, 2004) and spire proteins (Baum and Kunda, 2005; Quinlan et al., 2005; Schumacher et al., 2004), both of which nucleate linear actin filaments as opposed to branched ones. Such non-Arp nucleators taken together with the Arp depletion and perturbation experiments suggest that redundant pathways may exist for the protrusion of lamellipodia and veils. The alternative

nucleation pathways also suggest the possibility of cell system dependent or conditional involvement of motility mechanisms.

Given the uncertainties surrounding the mechanisms that contribute to protrusive motility, we concluded that the presumed equivalence of neuronal growth cone veils and fibroblast lamellipodia required a closer evaluation. We felt that a kinetic-structural analysis of the growth cone veil similar to that which we carried out for keratocytes and fibroblasts (Svitkina and Borisy, 1999) was warranted. Examination of the growth cone literature indicated that no such study had yet been conducted. Most work that had addressed this topic occurred before current models of actin based protrusive motility were available and before methodology was available to carry out correlative analysis at high resolution. The general conclusion that emerged was that an actin network existed in veils, often referred to as a “cortical meshwork” (Clark et al., 1983; Landis, 1983; Lewis and Bridgman, 1992; Yamada et al., 1970; Yamada et al., 1971). These earlier studies, carried out at low resolution and lacking biomarkers such as Arp2/3 for the lamellipodium, were insufficient to answer questions regarding whether growth cone veils protruded by a similar or different mechanism from that of fibroblast or keratocyte lamellipodia.

Thus, a gap exists in our understanding of growth cone activity. We lack information on the supramolecular organization of the motility machinery in relationship to the dynamic behavior of protrusion and retraction. We have attempted to fill this gap by carrying out correlative light and electron microscopic analysis on chick dorsal root ganglion cells grown in explant culture. Time-lapse imaging of a living growth cone on a

second-by-second time scale provided dynamics data on veil activity while platinum replica electron microscopy of the same veils allowed us to determine the supramolecular organization of the veils in a known state of behavior. The results obtained provide new information on the neuronal motility machinery and allow a conceptual framework to be formulated for understanding the structural basis of growth cone advance.

2.2 Results

Veils Alternate Phases of Protrusion and Retraction

Although many qualitative studies have characterized growth cone advance in terms of overall velocity and directionality, relatively few have provided detailed quantitative parameters. Bray and Chapman (1985) carried out a quantitative analysis of microspike movement but, as far as we are aware, the dynamics of veil movement have not been similarly deconstructed. In preparation for correlative electron microscopic analyses, we first determined basic parameters for growth cone behavior in our whole DRG explants. Confirming results in the literature (Argiro et al., 1984; Goldberg and Burmeister, 1986; Landis, 1983), growth cones of DRG axons advanced rapidly (1.09 ± 0.34 μm/minute) with high persistence (0.9 over a period of 1 hr) for long periods of time (measured over 3-8 hrs) (Fig. 1A). However, this relatively regular advance, evident from low magnification, time-lapse images taken at intervals of minutes, belied the chaotic behavior evident at a time scale of seconds.

High magnification, high temporal resolution (2-3 s) image sequences showed significant shape changes in individual growth cones from frame to frame suggesting

that the veils and filopodia which comprise the growth cone were changing on a rapid time scale. Kymographs were constructed for individual veils within growth cones to analyze their detailed behavior (Figure 6B). As reported previously in qualitative terms (Goldberg and Burmeister, 1986; Tosney and Wessells, 1983), veils frequently showed periods of protrusion and retraction. Velocities of veil protrusion and retraction were obtained from the kymographs. Transitions between protrusion and retraction were defined by direction reversals observed in the kymograph. Durations of veil protrusion and retraction were calculated by dividing the total time protruding or retracting by the total number of transitions between protrusion and retraction.

The kymographs and quantitative data (Figure 6C) indicated several aspects of veil behavior. First, veils alternated phases of protrusion and retraction with a small fraction of time spent in a paused or irregular state. The average duration of a protrusive phase at the front of the growth cone was about a minute, and transitions to retraction were abrupt. This indicates that for correlative electron microscopic analysis to capture characteristic features of a phase or a transition, it would need to be carried out with a temporal resolution of seconds.

Second, veil dynamics showed differences or similarities depending on position in the growth cone. Protrusion was somewhat faster (35%, $p=0.016$, two-tailed) in the front as compared to the rear of the growth cone while retraction velocities did not vary significantly from the front to rear. However, at any given position along the growth cone perimeter, protrusion velocity was significantly greater (2.2x to 2.5x) than retraction velocity ($p<0.01$). In the front half of the growth cone, protrusion and retraction occurred

Figure 6 Growth cone advance and veil dynamics

(A) Growth Cone Advance. Blue line traces path traveled by growth cone during 3 hour time lapse observation. (*) indicates start; scale bar 40 μm. (B) Veil Dynamics. Kymographs (right) of veils in growth cone front (top, left) and rear (bottom, left) show alternation of protrusion and retraction. Scale bar, 10 μm; black line denotes path along which kymograph was obtained. (C) Orientation of protrusion and retraction phases. “Other” denotes veil dynamics, collapse, ruffling, stalling, - not readily categorized as protrusion or retraction. N=151 veils; 20 individual growth cones; 352 minutes observation; 329 transitions recorded.

A

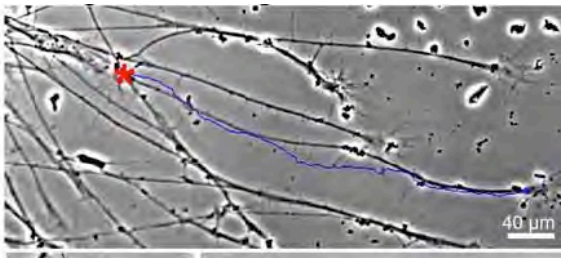

B

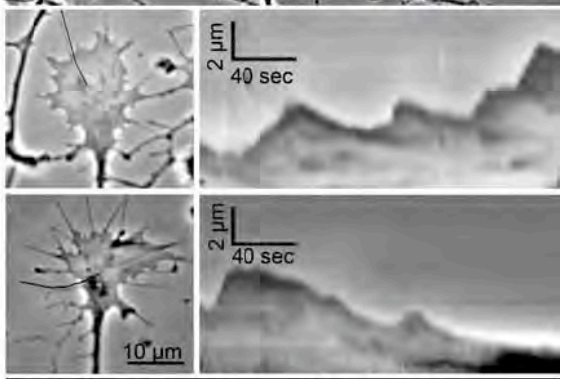

C

	FRONT			REAR		
	Protrusion	Retraction	Other	Protrusion	Retraction	Other
Velocity (µm/min)	6.5 ± 4.1	2.6 ± 2.7	N/A	4.8 ± 4.1	2.2 ± 2.7	N/A
Duration (min)	1.1 ± 0.9	0.8 ± 0.5	0.7 ± 0.6	0.6 ± 0.3	2.3 ± 2.0	0.4 ± 0.2
% Time	43.8	43.1	13.1	17.7	78.6	3.8

for the same percentage of time and were similar in duration, whereas in the rear half of the growth cone, retraction occurred 4 times more frequently and lasted 4 times as long ($p<0.004$). Thus, the major differentiation between the front and rear of the growth cone was in the greater duration and frequency of retraction in the rear.

Third, veils protruded more rapidly (~ 6 X) than the growth cone translocated; a property that requires explanation. Part of the explanation comes from the fact that individual veils protrude at various angles to the growth cone axis. For a veil protruding at an angle, ϕ, with respect to the direction of net advance, the contribution to the net velocity is the veil velocity times cos ϕ. Integrating over all orientations reduces average axial velocity by a half. The balance of the explanation comes from recognizing that retraction offsets much of protrusion. The overall rate of growth cone advance, v_{gc}, may be estimated from the parameters for individual veils as = 1/2 [$v_p\ d_p\ f_p$ - $v_r\ d_r\ f_r$] where v, d and f are velocities, durations and fraction time in phase for protrusion (p) and retraction (r), respectively, in the front of the growth cone. Inserting the parameters from Figure 6C gives v_{gc} = 1.11 mm/minute which corresponds surprisingly well to the measured rate of 1.09 mm/minute for overall growth cone advance. We conclude that growth cone advance may be accounted for on the basis of individual veil dynamics.

Veils can be Categorized based on Association with Filopodia

Since growth cone behavior could be largely deconstructed into veil and filopodial behavior, we examined possible distinctions between veils as they related to filopodia. Veils were categorized as to whether they were protruding or retracting and whether

they occurred between two adjacent filopodia, were associated with a single filopodium or were not associated with filopodia (Figure 7). Remarkably, 74% of protruding veils occurred between two filopodia less than 2.5 μm apart and an additional 10% occurred along a single filopodium (Figure 7B). Often, veils would arise from the junction of two filopodia roots or in the “crotch” of two filopodia diverging from a common trunk. Veil behavior seemed to occur in separable, independent units, frequently separated by a filopodium. The independent behavior of veils was manifested as protrusion on one side of a filopodium and retraction or pause on the other side. Thus, filopodia seemed to serve as ‘”boundaries” for veil formation. However, veils could often arise (16%) without obvious associations with filopodia, indicating that filopodia were not necessary for veil formation.

Veils were also categorized by shape because of the possibility that morphology would be indicative of mechanism. Lamellipodia of fibroblast type cells typically display a convex shape because of protrusive forces pushing outward over a range of directions. Protruding veils not associated with filopodia also displayed a convex shape. However, veils associated with filopodia commonly displayed a concave shape. All retracting veils and approximately half of protruding veils were concave. A concave shape during retraction can be understood in terms of surface tension applied to the veil against filopodia that resist compression. However, the explanation for a concave shape during protrusion seemed counter-intuitive; therefore, concave and convex protruding veils were subjected to separate analyses.

Figure 7 Veil Protrusion and Retraction are Primarily Filopodia Associated.

(A) Timelapse merges illustrate veil categories. In this and all succeeding figures, protruding and retracting regions are indicated by red and cyan, respectively, by merging the later time point (red channel) with the earlier time point (blue and green channels). Filopodia Associated Protrusion – protrusion between two established filopodia; veil edges can be convex (a) or concave (b); Filopodia Independent Protrusion – veil protrusion not connected to established filopodia (c); Filopodia Associated Retraction – retraction between two filopodia, retaining direct connection throughout retraction (d); Filopodia Independent Retraction (5, arrowhead) is seen less than 3% of the time; Single Filopodium Associated Protrusion – protrusion along a single filopodium (e, asterisk) and veil protrusion arising on a filopodium shaft (f). (B) Tabulation of frequency and width of veils in each category.

A.

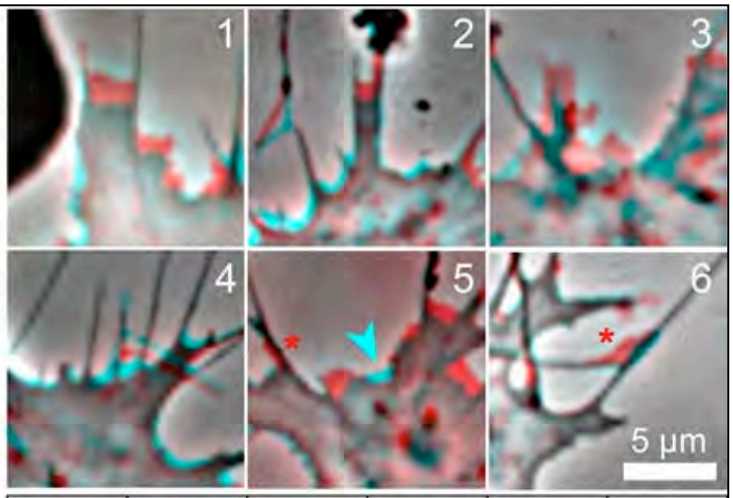

B.

Direction of Veil Movement	# of Filopodia Supporting Veil	% of Veils	Edge Curvature	% of Veils	Veil Width (µm)
Protrusion	Filopodia Associated	74.0	Concave	40.7	1.54 ± 0.70
			Convex	59.3	1.32 ± 0.55
	Single Filopodium	9.6	N/A		1.03 ± 0.65
	Filopodia Independent	16.4	Convex	100	4.66 ± 1.67
Retraction	Filopodia Associated	97.1	Concave	100	1.81 ± 0.92
	Filopodia Independent	2.9			

Figure 8 Correlative Light and Electron Microscopy of Filopodia Associated Veil Protrusion and Retraction

(A) Phase contrast panels show a low magnification image of the growth cone with a white box denoting the region of interest, followed by four consecutive images from the last 9 seconds of the time lapse sequence before the cell was extracted, a live-live phase contrast merge of the first and last images, the same region after extraction "lysed", and a phase contrast merge of the lysed and the last live image. In all merges, red regions indicate protrusion, cyan regions indicate retraction. The veil in the left panel was protruding at 4.2 μm/min, the veil in the right panel was retracting at 1.7 μm/min. (B) Electron micrographs of region of interest from the time lapses in A. (C) Higher magnification of the boxed regions in B.

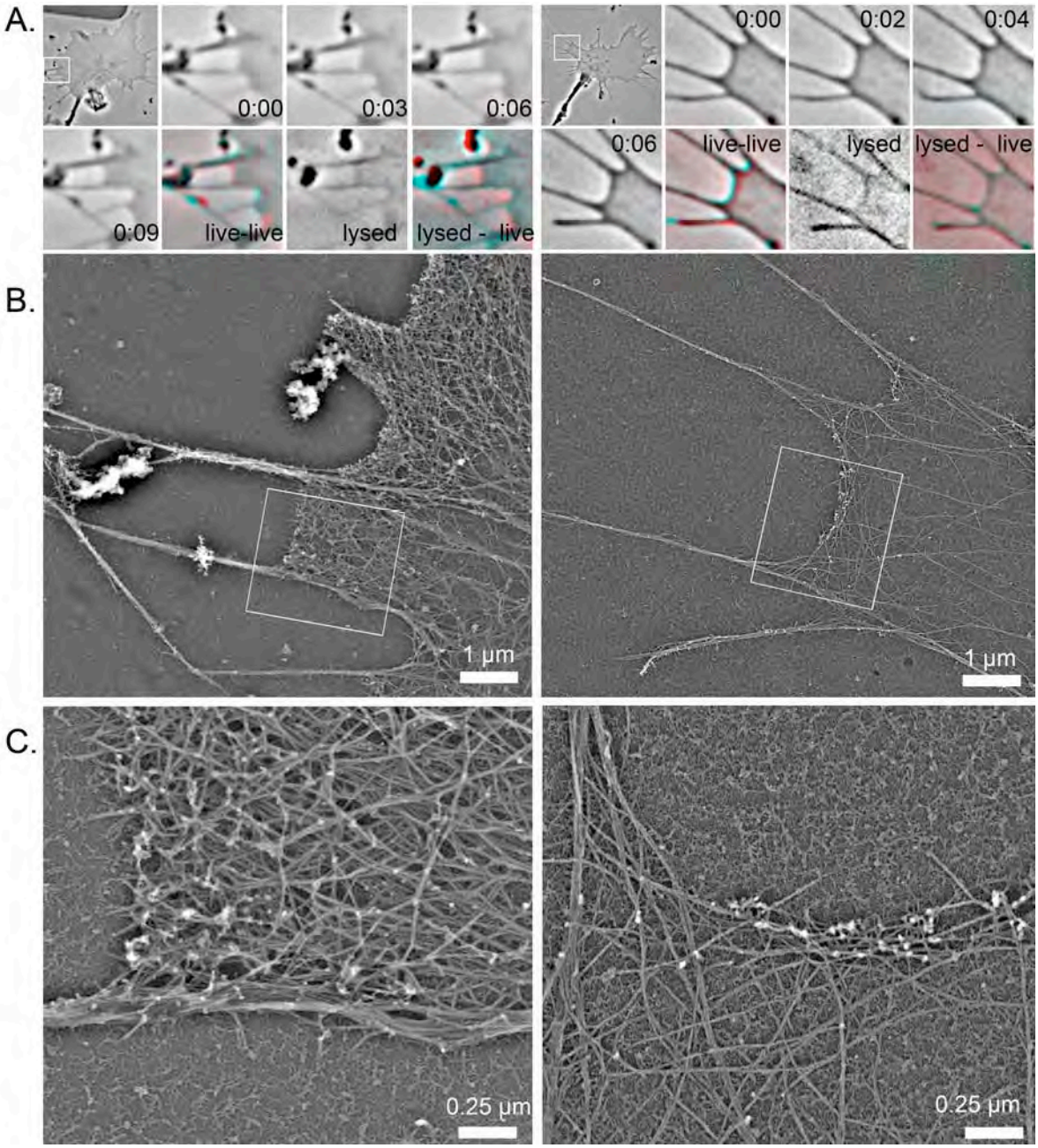
A.
0:00
0:03
0:06
0:09
live-live
lysed
lysed - live
0:00
0:02
0:04
0:06
live-live
lysed
lysed - live
B.
1 µm
1 µm
C.
0.25 µm
0.25 µm

Correlative Light and Electron Microscopy Reveals Structure-Function Relationships in Veils

Correlative microscopy combines kinetic analysis of a living cell by light microscopy with structural analysis of the same cell by electron microscopy to determine the supramolecular organization of the cell in a known state of behavior (Svitkina and Borisy, 1998). For the growth cone, this means carrying out analyses on veils known to be protruding, retracting or in transition. As the most common form of both protruding and retracting veils was that associated with two filopodia, we first focused on this category (Figure 8). The left panels of Figure 8 show a protruding veil that had been protruding for ~21 seconds at the time of extraction and fixation. The “live - live” panel is a color merge of the last two images of the living cell in which red indicates veil protrusion; cyan indicates retraction. The “lysed-live” panel is a merge between the cell just after extraction and the last live image. A region of the growth cone (white box) is shown in the low magnification EM and the veil under analysis is shown in the higher magnification EM. The protruding veil contains a dense, filamentous network that is bounded by the filopodia and comprised of both branched filaments and interspersed longer filaments. Overall, the appearance resembles that characteristic of fibroblast lamellipodia. At low magnification both associated filopodia can be clearly distinguished from the network. At high magnification, the network is in very close contact with the filopodia, and filaments appear to both enter into and/or come off of the filopodium.

The right panels of Figure 8 show the kinetics and structure of three adjacent retracting veils that had been receding for almost 60 s at the time of extraction. They are

strikingly different than protruding veils in ultrastructure, although the differences are not appreciable by phase contrast microscopy. One difference is the density of filaments in the retracting veil. Unlike the protruding veil, the filaments in retracting veils are scarce,--sufficiently so that the background of the substrate is visible. A second difference is the organization of filaments. Filaments in retracting veils do not show a dendritic network; rather, they typically show filaments bundled and running parallel to the retracting edge.

The difference in filament density between protruding and retracting veils was sufficiently dramatic that we sought confirmation independent of processing for electron microscopy. We used fluorescently tagged phalloidin staining to quantify actin filament density (Svitkina et al., 1997) prior to preparation of the samples for electron microscopy. As shown in Figure 9, linescan analysis of phalloidin staining indicated that protruding veils had a 2 X greater amount of actin and a 3 X greater extent (depth) of the actin rich region than retracting veils. Additionally, we measured the total length of actin filaments contained in 0.25 μm^2 boxes drawn at the center of the edge of protruding and retracting veils. Protruding veils contained an average of 57.7 ± 6.6 μm actin/μm^2, while retracting veils contained 19.8 ± 4.0 μm actin/μm^2 (n=10 veils for each state, $p<0.00001$) which corresponds well with the phalloidin staining shown in Figure 9. Thus, the disparity in filament density between protruding and retracting veils was not a consequence of sample preparation for EM.

A second line of evidence for the difference between protruding and retracting veils comes from analysis of phase transitions. Phase transitions are abrupt, occurring within one or two frames (3-6 s). For an average phase duration of approximately 60 s,

this means that randomly picking the time of extraction and fixation for EM will generate approximately 5-10% of the veils caught in a transition between retraction and protrusion. Such an event is illustrated in the left panel of Figure 10. The cyan arrow in the live-live merged image shows a veil in a retraction phase, while the red arrow in the subsequent lysed-live image identifies a newly protruding veil that has formed in the same location during the time needed for lysis. The electron micrographs show that the nascent veil is dense and dendritic in contrast to the sparse, unbranched network behind it. The structure of this transition suggests that the dendritic protruding veil appears to have formed by branching off the roots of the associated filopodia and/or the residual filaments of the previously retracting veil. Finally, a third line of evidence comes from adjacent veils displaying opposite behavior. Adjacent veils that share a filopodium frequently exhibit independent behavior as illustrated in the right panels of Figure 10. The lysed-live merge shows two adjacent veils (red and cyan arrows), separated by a single filopodium, that exhibit opposite behavior where the lower veil protrudes and the upper veil retracts. The high magnification EM shows the sparseness of filamentous actin in the retracting veil adjacent to the robust dendritic network in the protruding veil. The correlation of filament density with veil behavior strongly suggests that the appearance of the network is not an artifact of processing for electron microscopy. Rather, the results indicate a significant difference in filament organization between protruding and retracting veils that has not been previously recognized.

Figure 9 Actin Distribution in Protruding and Retracting Veils

(A) Veil dynamics merge (left) and filamentous actin distribution (right) in a growth cone. The merge combines the last live phase contrast image before extraction and the one obtained 6 seconds earlier. Enlarged insets (p, r) show regions of veil protrusion (red) and retraction (cyan). (B) Linescans of Texas Red phalloidin fluorescence for protrusion and retraction derived from the regions of the growth cone shown in A (dotted lines). Fluorescence normalized to 100 at peak of protrusion distribution. Protruding veils have more and deeper filamentous actin than retracting veils. N=4 growth cones; 9 retracting veils; 22 protruding veils.

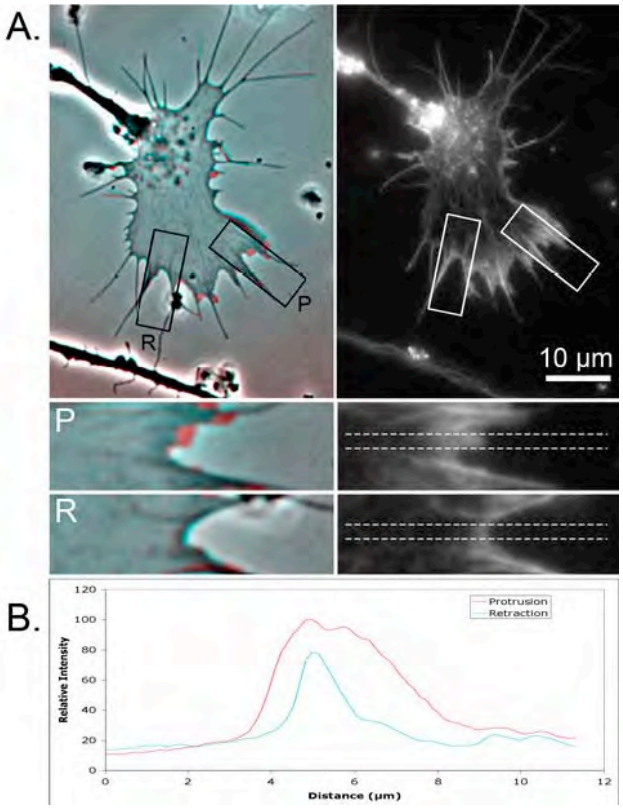
A.
P
R
10 µm
P
R
B.
Protrusion
Retraction
Relative Intensity
Distance (µm)
0
20
40
60
80
100
120
0
2
4
6
8
10
12

Figure 10 Phase Transitions and Local Autonomy of Veils.

Panel Construction same as in Figure 4.

(A) Left: Nascent protrusion (3.6 μm/min) characterized by dense branched network is demarcated from surrounding sparse network. Right: Protruding (7.6 μm/min) and retracting veil (2.8 μm/min) adjacent to same filopodium show distinct filament organization, - dense branched vs sparse, respectively. (B) Electron micrographs of the regions of interest from the time lapses in A. (C) Higher magnification of the boxed region from the EM in B. The new protrusion (left) is sharply demarcated from the local network (dashed line). Adjacent filopodia associated veils (right) have independent behavior.

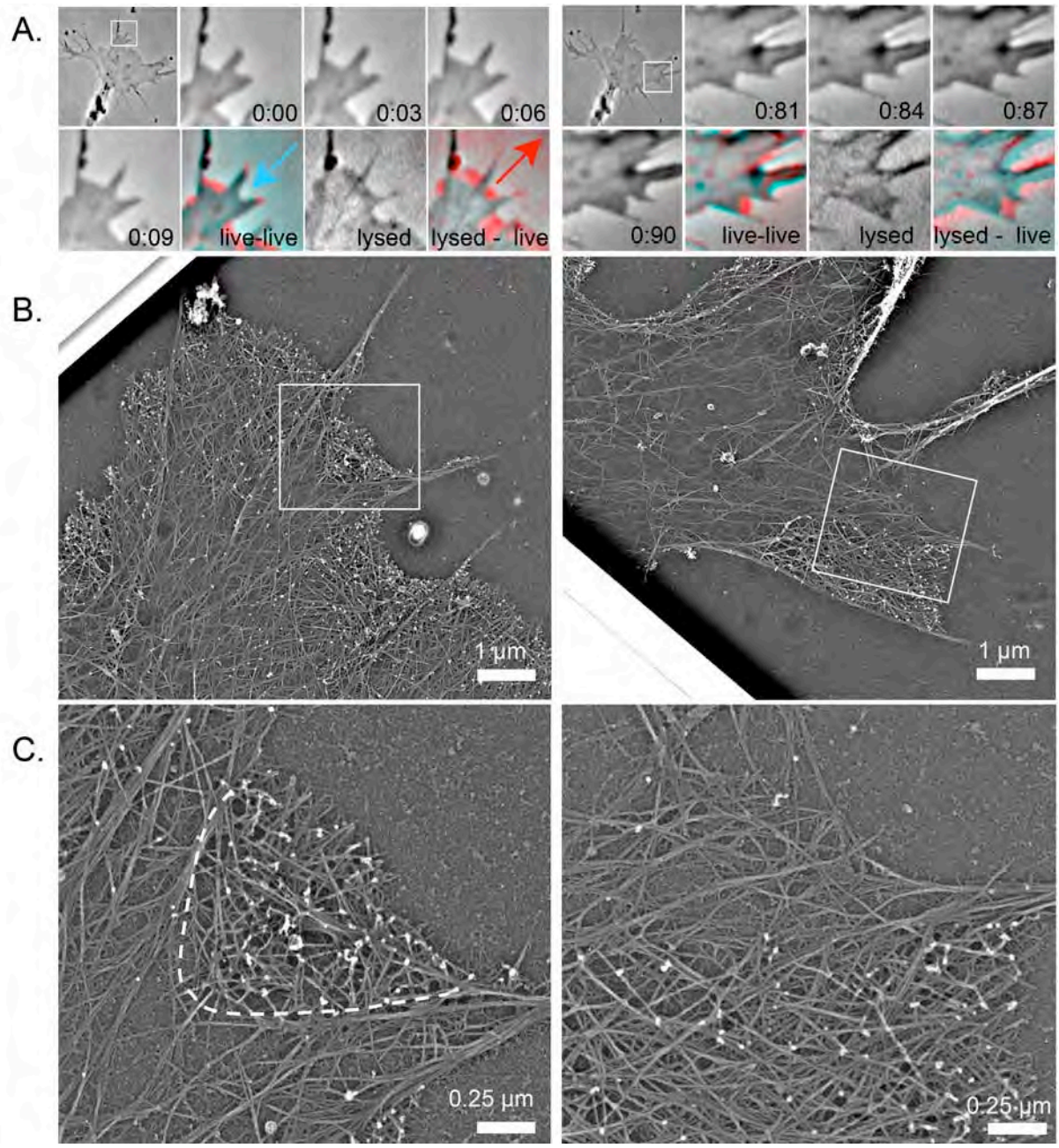
A.
0:00
0:03
0:06
0:09
live-live
lysed
lysed - live
0:81
0:84
0:87
0:90
live-live
lysed
lysed - live
B.
1 µm
1 µm
C.
0.25 µm
0.25 µm

Veils that protruded along single filopodia also showed a dense, dendritic network. In the nascent (4 s old) veil shown in Figure 11A, the surrounding region was retracting prior to the veil's appearance, while the filopodium was already present. Besides its dense network, the nascent veil contained long filaments that apparently connected to the filopodial shaft, while branches appear directed away from the shaft.

Filopodia associated veils can protrude in isolation from other veils and the body of the growth cone (Figure 11B). In this example, the filaments in the associated filopodium merged near their base, isolating the veil from the rest of the growth cone. Filaments in the veil formed both branched and tightly bundled filaments. They are also seen growing out of and into the associated filopodia, suggesting the ability of filaments to form by branching off of filopodia shafts. The average angle at which filaments branched off of filopodia was measured at 70.9 ± 3.6˚ (n=51 branches, 8 growth cones). Figure 11C shows a typical filopodia independent protrusion whose network organization closely resembles the lamellipodia seen in fibroblasts and keratocytes (Svitkina and Borisy, 1999). The veil had been protruding for approximately 1 minute at the time of extraction, and contains a mixture of dense, branched network and embedded loosely bundled long filaments. Figure 11D shows a group of nascent veils arising as multiple finger-like protrusions independent of any association with filopodia. These jutting protrusions are the usual precursor to the smooth edged filopodia independent veil.

Taken together, the correlative microscopy experiments establish several new features of the growth cone motility machinery. The organization of actin filaments in

Figure 11 Alternate Forms of Veil Protrusion.

The upper panel of each subsection contains a low magnification image of the growth cone, with the region of interest boxed, a single phase contrast overlay, and a low magnification EM of the region of interest.

(A) Nascent Veil protrusion (6.8 μm/min) along a single filopodium. Veil contains a dense network of filaments connected to filopodial shaft. (B) Veil formation (8.3 μm/min) isolated from lamellipodium. Dense network interconnects two filopodia shafts. (C) Established Filopodia “independent” protrusion (8.1 μm/min). Veil organization is mixture of dense network and loosely bundled long filaments. Boxed regions (a-c) show branched filaments in the network, pseudo-colored cyan for visualization. (D) Nascent Filopodia “independent” protrusion (1.1 μm/min). Veil displays multiple finger-like protrusions containing dense network and some long filaments.

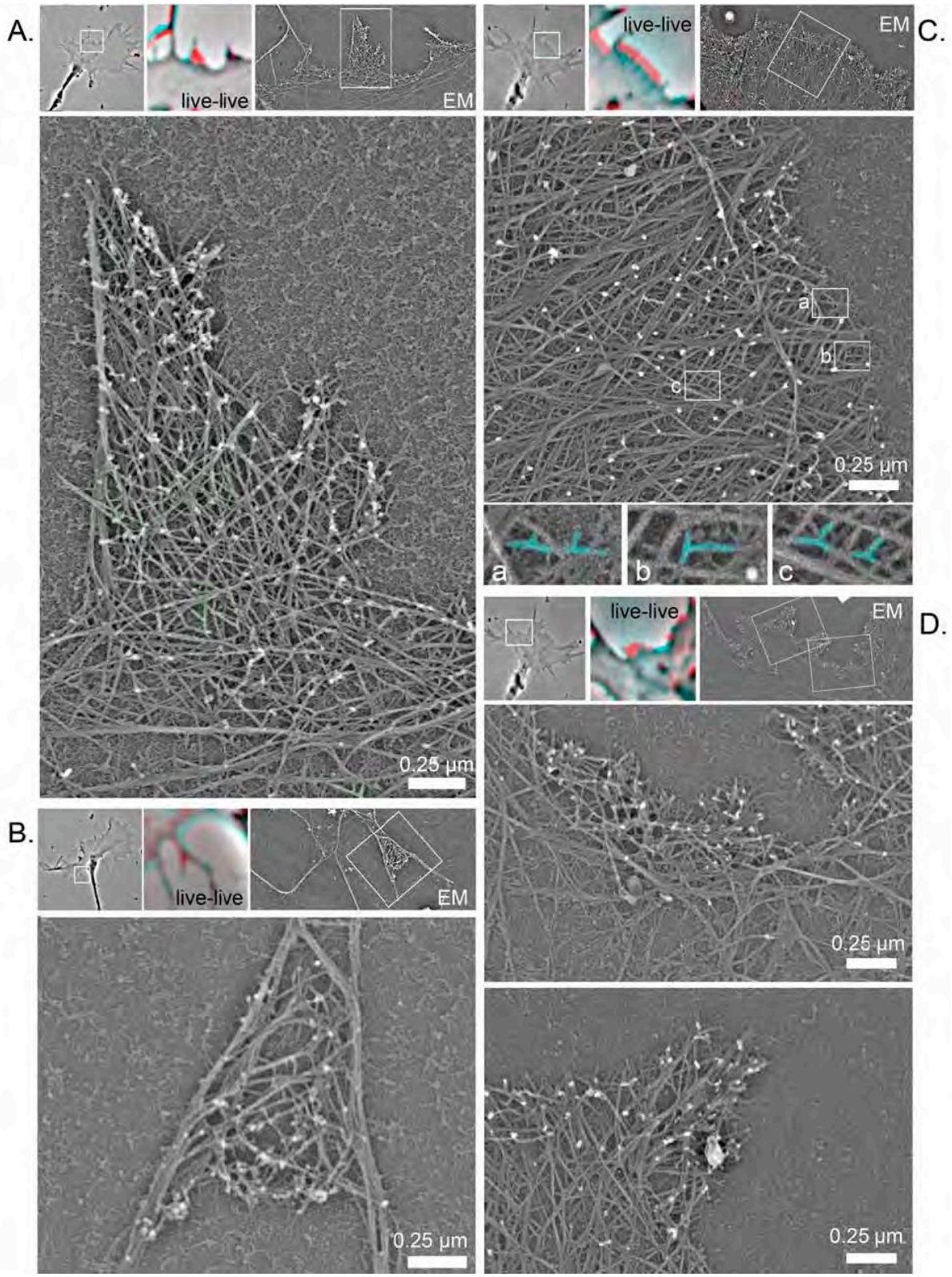
A.
live-live
EM
0.25 µm
B.
live-live
EM
0.25 µm
C.
live-live
EM
a
b
c
0.25 µm
a
b
c
D.
live-live
EM
0.25 µm
0.25 µm

protruding veils is similar to that in lamellipodia of fibroblasts; retracting veils lack a dendritic network but contain sparse long filaments; and dendritic networks can form off filopodia.

Arp2/3 Complex is Localized to Actin Networks In Veils and Along Filopodia

Since the supramolecular organization of filamentous actin in protruding veils appeared similar to that seen in the lamellipodia of motile fibroblasts and keratocytes, we tested whether veils contained the Arp2/3 complex, a biomarker characteristic of dendritic networks. Fluorescence immunostaining for Arp3 demonstrated, at the light microscopic level, that Arp3 was enriched at the leading edge of the growth cone and co-localized with phalloidin stained actin filaments (Figure 12A). We also stained for the p34 subunit, using an alternative fixation technique, and saw similar staining patterns in both DRG and PC-12 growth cones (Figure 13 A-C). Control staining and immunoblotting demonstrated specificity of both antibodies (Figure 14 A-C). Expression of myc-tagged Arp3 in NG108 cells as evaluated by immunostaining (Figure 14D) and expression of GFP-tagged Arp3 in PC-12 growth cones as evaluated by TIRF (total internal reflection fluorescence) microscopy showed localization of the expressed protein at the leading edge of protruding growth cone veils (Figure 15). Thus, on the basis of immunostaining and expression data, the Arp2/3 complex seemed to be present in the growth cone.

To localize the Arp2/3 complex at higher resolution and to evaluate Arp localization in relation to its protrusion history, immuno-gold electron microscopic

staining was carried out using correlative microscopy Figure 12 B, C, D). The EM of the protruding veil in the lysed-live merge (Figure 12 C, left) was overlayed with a 0.5 μm grid, and the number of 10 nm gold particles in each box was counted (for veil regions that did not fill a box, the count was normalized to the area of a 0.5 mm box). The "heat map" reflecting the number of gold particles (Figure 12C, right) indicates that the Arp2/3 complex was highest in concentration at the leading edge of the protruding veils and was localized to the dense dendritic network (as opposed to regions with bundles of long filaments). Protruding veils contained and average of 145 ± 20 gold particles per μm^2 at the leading edge, and 60 ± 9 gold particles per μm^2 1 μm back from the leading edge, while retracting veils contained only 17 ± 7 gold particles per μm^2 at the retracting edge, and 11 ± 6 gold particles per μm^2 1 μm back from the retracting edge (n=8 protruding and 8 retracting veils). In less dense regions of protruding veils, gold particles were localized to individual Y junctions (Figure 16). Sparse non-protruding regions were not enriched in gold particles. Control growth cones stained only with secondary antibody labeled with gold particles contained very few gold particles (Figure 14E). Inset shows Arp3 staining (Figure 12D) with gold particles pseudo-colored yellow for easier visualization.

Veils sometimes protruded with a concave shaped leading edge. Because such a shape is characteristic of retracting veils, we wondered whether concave protrusions proceeded by a different mechanism from that of convex protrusions and so tested whether Arp2/3 was present in such veils. We found that Arp2/3 in concave veil edges varied with direction of veil movement. Arp2/3 was found in veils protruding with a

Figure 12 Distribution of Arp2/3 in Veils.

(A) Growth cone immunostained against Arp3 subunit and phalloidin. Inset shows an enrichment of Arp3 (green) at the leading edge that co-localizes with phalloidin stained actin (red). (B) Low magnification growth cone (veil protrusion at 5.3 μm/min) followed by time lapse and merges of boxed region. (C) Left. EM of region in lysed-live in (B) immunostained against Arp3 subunit. Right. Same EM overlayed with a 0.5 μm grid colored to reflect the number of gold particles in each box; heat map indicates number of gold particles per 0.25 μm2 box. Similar to (A), Arp3 staining co-localizes with actin and is highest at the leading edge of protruding veils. (D) High magnification of the boxed region from (C). Gold particles have been pseudo-colored yellow.

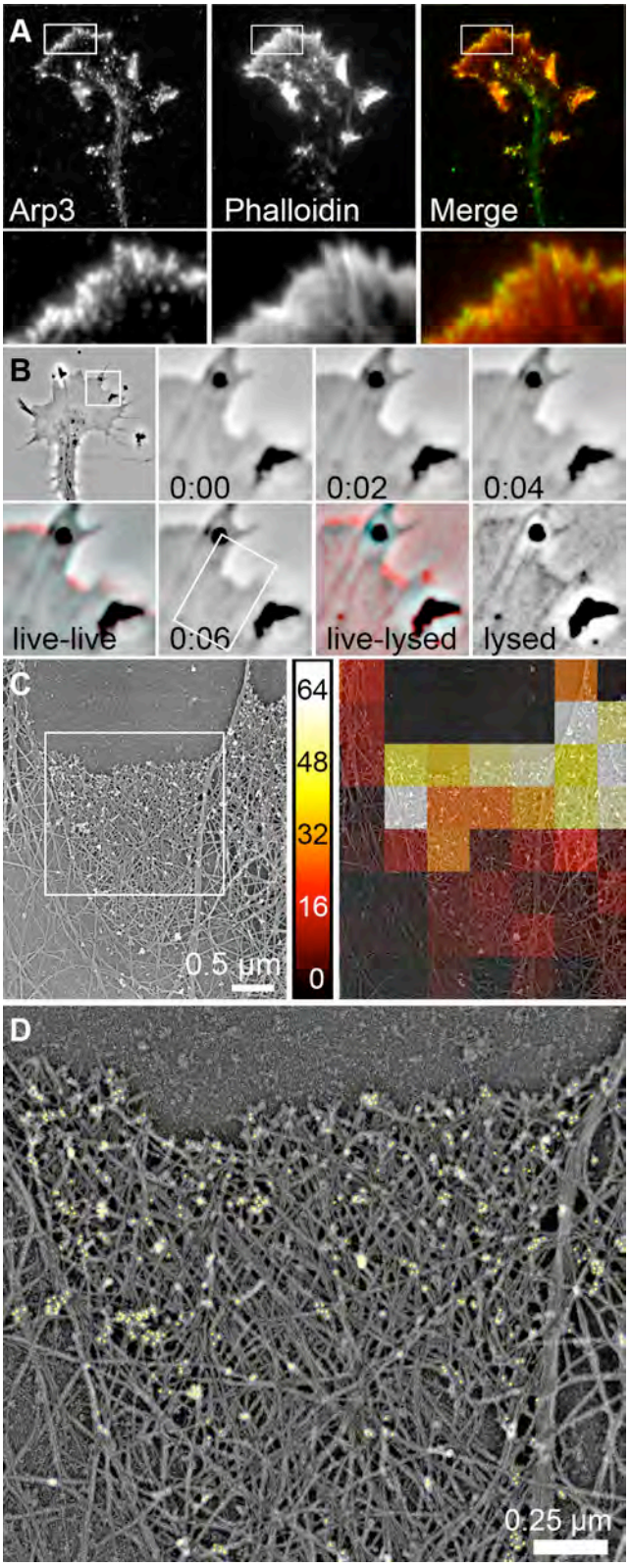
A
Arp3
Phalloidin
Merge
B
0:00
0:02
0:04
live-live
0:06
live-lysed
lysed
C
64
48
32
16
0
0.5 µm
D
0.25 µm

Figure 13 Immunostaining of Additional Arp2/3 Subunits in Growth Cones.

Scale bar = 10 μm. (A) DRG growth cones immunostained against the p34 subunit and phalloidin. The staining pattern is the same as that observed for Arp3. (B,C) PC-12 growth cones immunostained against Arp3 (B) or p34 (C) and phalloidin. The staining pattern is the same as that observed in chick DRG growth cones.

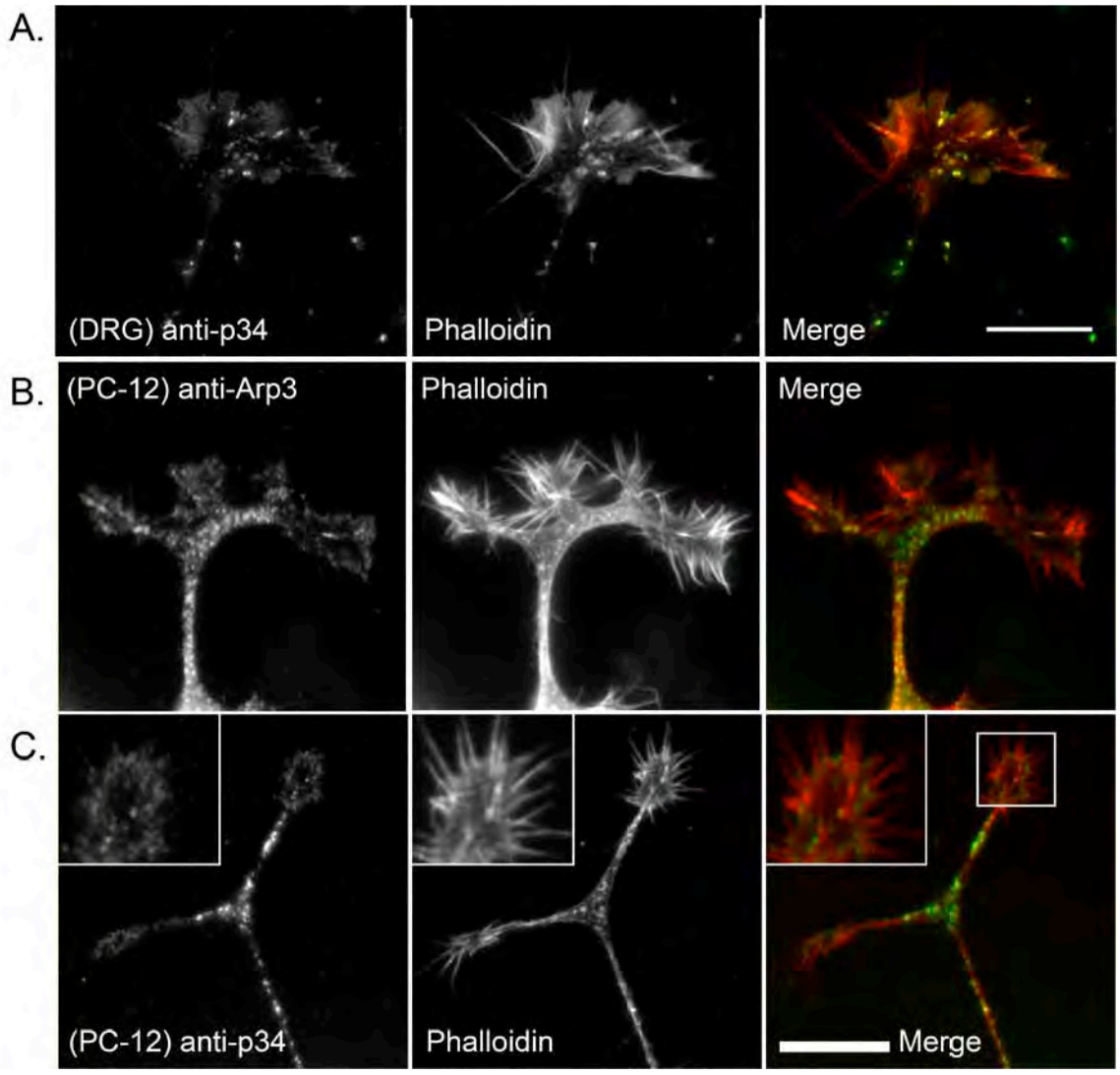
A.
(DRG) anti-p34
Phalloidin
Merge
B.
(PC-12) anti-Arp3
Phalloidin
Merge
C.
(PC-12) anti-p34
Phalloidin
Merge

Figure 14 Immunostaining Controls.

(A) Immunoblot of PC-12 lysate, probed with anti-p34 and tubulin (left), anti-Arp3 and tubulin (right) primary antibodies. (B) Scale bar = 10 μm. PC-12 cell extracted, fixed, and immunostained with rabbit non-immune serum in place of 1˚ antibody and FITC 2˚ antibody (left), and rhodamine phalloidin (right) shows little fluorescence in the non-immune channel, with none observed in the growth cones. (C) Linescan analysis of both channels in B shows fluorescence in non-immune channel is negligible. (D) Scale bar = 5μm. (left) NG-108 cells, the lower cell (*) is expressing myc-tagged Arp3, the white box marks a region containing the lamellipodia of both cells shown at higher magnification in the three panels to the right. The left center panel is immunostained against Arp3, and shows smooth staining at the leading edge of both cells. The right center panel is immunostained against myc, showing staining at the leading edge of the transfected cell, but not the untransfected cell. The merge in the right panel shows colocalization of Arp3 and myc immunostaining at the leading edge in the transfected cell. (E) Control Immungold EM, processed along with experimental samples, incubated with gold labeled 2˚ only. Grid marks 0.2 μm^2 boxes, number of gold particles contained in each box is shown.

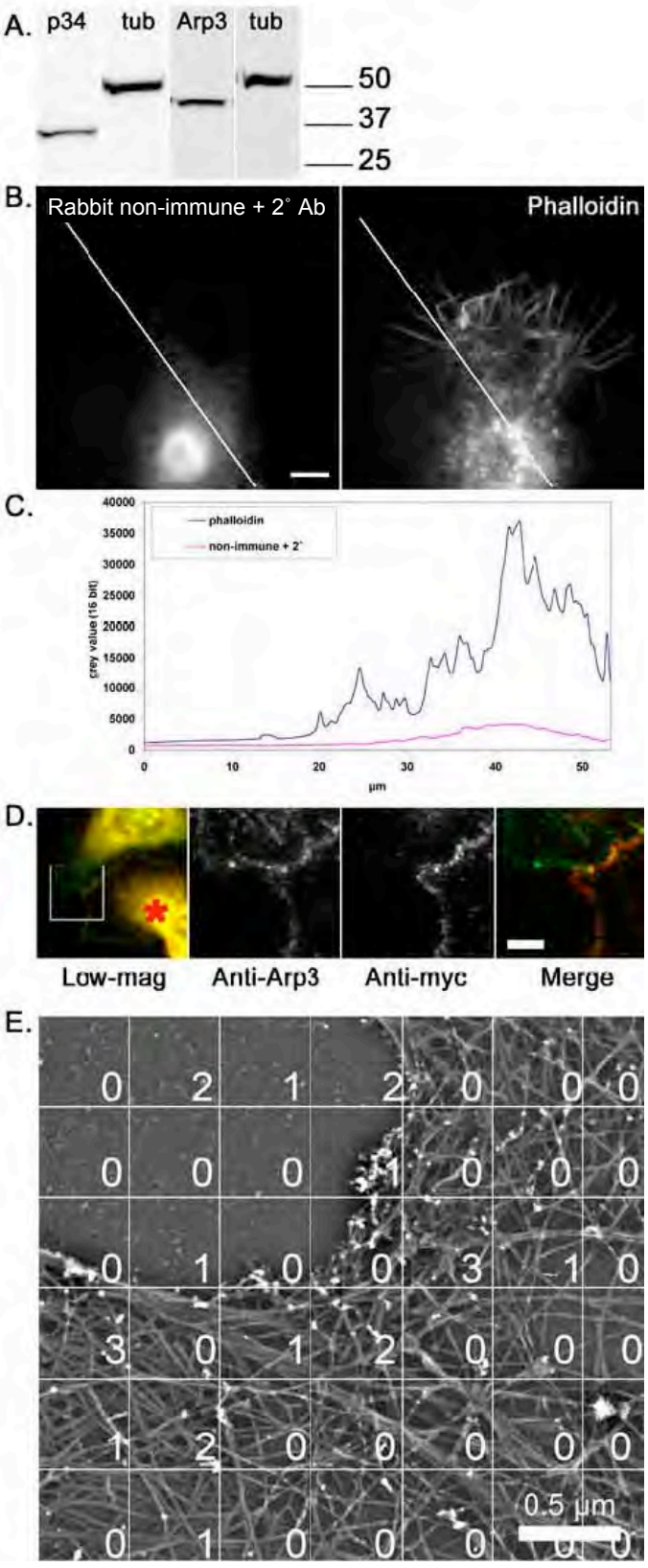
A.
p34
tub
Arp3
tub
50
37
25
B.
Rabbit non-immune + 2° Ab
Phalloidin
C.
phalloidin
non-immune + 2°
grey value (16 bit)
μm
D.
Low-mag
Anti-Arp3
Anti-myc
Merge
E.
0.5 μm

Figure 15 Localization of GFP-Arp3 expressed in PC-12 cells using TIRF microscopy.

(A) scale bar = 5 μm. (left) Whole PC-12 cell expressing GFP-Arp3 imaged using widefield fluorescence microscopy, the central region of the cell body is grossly overexposed in order to visualize the three peripheral growth cones, giving the impression of enrichment in the central region. (right) The same cell imaged using TIRF microscopy a few seconds later, yielding an even optical field that reveals no enrichment in the central region. (B) For all images, red arrows indicate protrusion, cyan arrows indicate retraction, scale bar = 2 μm. (1) Arp3 is seen in veils that protrude from the crotch of two pre-existing filopodia, away from the growth cone. (2) Arp3 is seen in veil protrusion along a single filopodium. (3) GFP-Arp3 is enriched in veils at the leading edge of the growth cone. (4) Arp3 enrichment decreases in retracting veils.

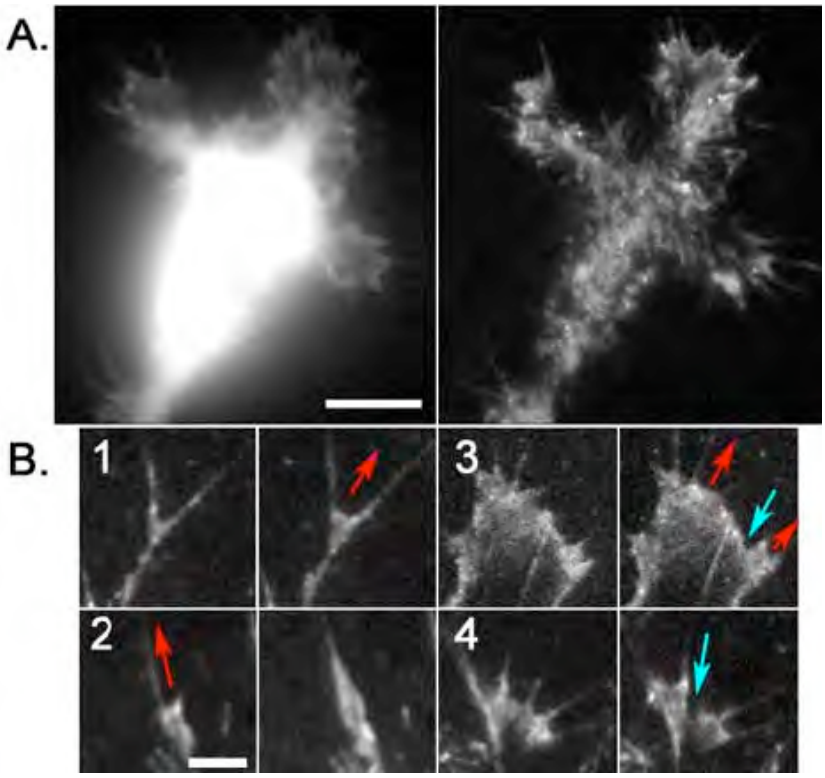
A.
B.
1
2
3
4

Figure 16 Localization of Arp3-Immunogold Particles to 'Y' Junctions of Protruding DRG Veils.

Scale bar = 0.1 μm. 11 similar examples were observed in 5 growth cones examined.

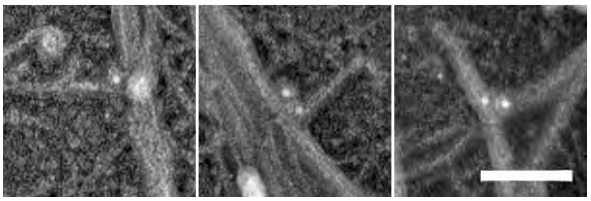

concave leading edge (Figure 17A) but was not enriched in retracting veils (Figure 17B). In this figure, the veil had been retracting for ~40s, displaying the usual concave edge. Typical of retracting veils, there was little underlying network. The network that did remain was not enriched with Arp2/3.

Arp2/3 was also found in veils that spontaneously formed along the shafts of filopodia. Figure 17C shows a small veil (*) that formed at the distal end of a filopodium, and then traveled down the filopodium shaft. The live-live merge and the low magnification electron micrographs show the veil as it approached the second filopodium and then began to protrude between the two filopodia. The network contains loosely bundled long filaments mixed with a dense branched network that stained for Arp3. Figure 17D shows a small veil that formed at a kink along the shaft of a filopodium over ~6 seconds. By light microscopy it appeared as a dark expanding spot along the shaft of the filopodium. Electron microscopy showed that the nascent veil contained a dendritic network enriched with Arp2/3 that was associated directly with filaments of the filopodium shaft. Thus, nascent veils that form along the length of filopodia are dendritic and associated with Arp2/3 just as veils that form between filopodia.

2.3 Discussion

The main goal of this study was to elucidate the organization of the actin cytoskeleton underlying veil movements. Our results provide a significant advance in three respects: First, we show that protruding veils are comprised of a densely branched network of actin filaments that is lamellipodial in appearance and includes the Arp2/3 complex. On

Figure 17 Correlation of Arp3 location with Veil Dynamics.

The upper panel of each subsection contains a low magnification image of the growth cone, with the region of interest boxed, a single phase contrast overlay, and a low magnification EM immunostained against Arp3 of the region of interest.

(A) Protruding filopodia (5.2 μm/min) associated veil with a concave leading edge. (B) Retracting filopodia (1.7 μm/min) associated veil with sparse actin network. (C) De novo veil initiation from filopodial shaft (*), which travels (11.3 μm/min) toward the growth cone. (D) Representative example of a veil arising de novo from a phase dense spot along the shaft of a filopodium.

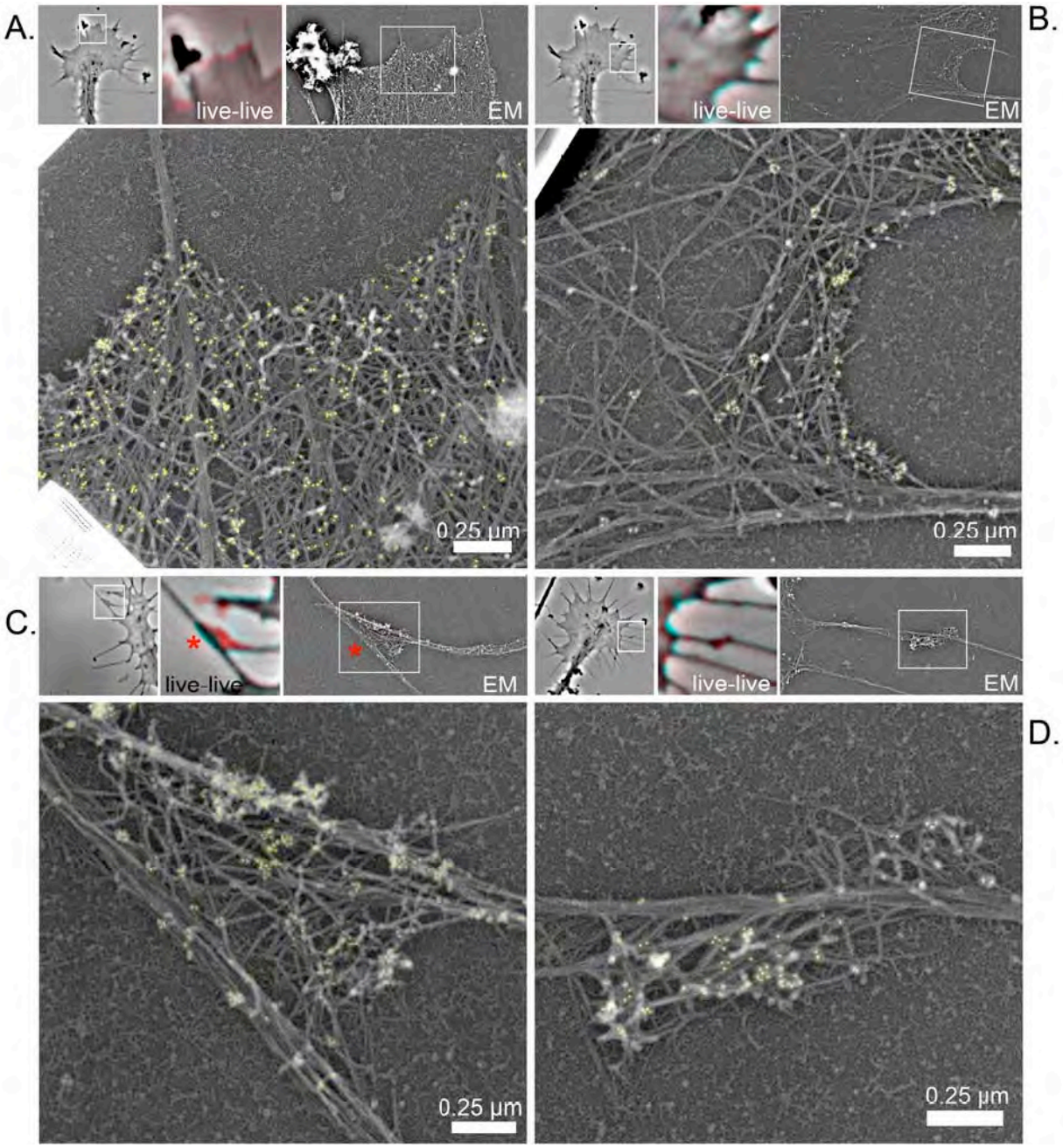
A.
live-live
EM
0.25 µm
B.
live-live
EM
0.25 µm
C.
live-live
EM
0.25 µm
D.
live-live
EM
0.25 µm

the basis of this structural and biomarker evidence, we infer that the dendritic nucleation/array-treadmilling mechanism of protrusive motility (Pollard and Borisy, 2003) is conserved in the veil protrusion of growth cone advance as in the motility of fibroblasts and keratocytes. Second, we delineate the supramolecular organization of the retraction phase, a phase originally reported by Abercrombie (Abercrombie et al., 1970; Abercrombie et al., 1971) in the crawling movement of fibroblasts but which has not heretofore been specifically analyzed at a high resolution structural level. Veil retraction, in contrast to protrusion, was characterized by sparse, long filaments with some bundled parallel to the cell edge. And, third, we show that filopodia have the capacity to nucleate dendritic networks along their length, a property consistent with veil formation seen at the light microscopic level but not previously understood in supramolecular terms. The basic findings of this study are summarized in Figure 18. We discuss each of these findings in turn and then comment on how they can be viewed as elements of motility which, when taken together, provide a conceptual framework for understanding the structural basis of growth cone advance.

Veil Protrusion

Correlative light and electron microscopy permits a kinetic-structural analysis of a cellular process. Temporal resolution of the kinetics is determined by the interval of time-lapse imaging and the time required for lysis and fixation (~ 3 sec). Spatial resolution is limited by the grain of the platinum (~3 nm) in the replica approach. Analysis of veils undergoing a transition from retraction to protrusion indicated that

formation of a branched, lamellipodia-like network was rapid, occurring within seconds after the phase transition. At veil protrusion velocities of 6 μm/min, electron microscopy established that about 1 μm of nascent dendritic network could be formed within approximately 10 seconds. This is consistent with rates of actin polymerization and lamellipodial formation in fibroblasts.

The conclusion that veil protrusion is dendritic in nature is not simply a confirmatory finding for neurons of a mechanism accepted in fibroblasts. Strasser et al found that Arp was paradoxically enriched in the central domains of the growth cone and neurites rather than in the veils, and that the ultrastructure appeared to contain few Y junctions, raising the question of what type of cytoskeletal organization was present in protruding veils (2004). Additionally, as outlined in the Introduction, recent studies involving mutation (Ng and Luo, 2004) or expression of a dominant negative construct (Strasser et al., 2004) have called into question whether neuronal advance proceeds by an Arp2/3-dependent mechanism. In both studies, although axon outgrowth occurred, pathfinding was aberrant. Our kinetic-structural results establish that the dendritic pathway does function in DRG growth cones that protrude veils under normal culture conditions. Further, the dendritic pathway biomarker, Arp2/3 was localized to the leading edge of protruding veils by both immunostaining and by expression of tagged Arp2/3 (both myc and GFP). It is not clear why this staining pattern was not seen in the study of Strasser et al (2004), but one possibility is that their widefield imaging missed the edge localization because of the greatly differing optical thickness of the neuronal shaft versus the lamellipodium (see (Grzywa et al., 2006a) and comparison of TIRF and

Figure 18 Modes of veil dynamics in the neuronal growth cone.

1. Veil protrusion associated with filopodia at the front and rear of the growth cone. Branched filaments can arise from the veil network and merge into the filopodia or can occur off existing filaments in the filopodia.

2. Veil protrusion along a single filopodium, either crawling along the side of the filopodium (2a) or arising de novo off the shaft of the filopodium (2b).

3. Veil protrusion independent of filopodia. The veil network appears to be similar to lamellipodial network seen in non-neuronal cells.

4. Retraction at the front and rear of the growth cone. The veil network becomes very sparse and some filaments are seen aligned and bundled, parallel to the membrane.

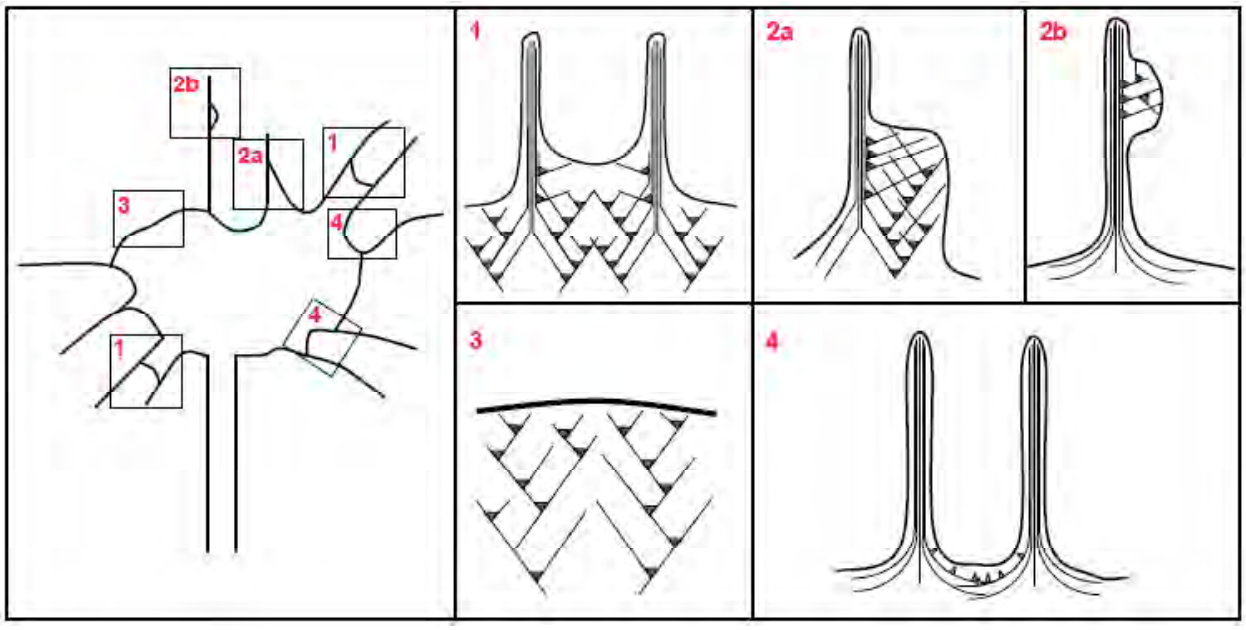
2b
2a
1
3
4
4
1
1
2a
2b
3
4

widefield imaging of growth cones in Supplemental Figure 3A). Alternatively, it is possible that the observed aberrant pathfinding reported in Arp2/3 deficient neurons (Ng and Luo, 2004; Strasser et al., 2004) indicates that Arp2/3-mediated dendritic nucleation may be critical for the exploratory functions of growth cones, required for pathfinding, while expendable for neurite extension.

Further, the role of the Arp 2/3 complex in protrusive motility has also been subject to re-evaluation in non-neuronal cells with results both supporting (Harborth et al., 2001; Rogers et al., 2003; Yamaguchi et al., 2005) and in opposition (Di Nardo et al., 2005; Gupton et al., 2005; Ng and Luo, 2004; Strasser et al., 2004) to an essential role for Arp2/3. Such mixed results in the literature suggest the possibility of cell system specific or conditional involvement of motility mechanisms. Moreover, redundant pathways likely exist for the protrusion of lamellipodia and veils. Unraveling the relative contribution of the pathways will require quantitative analyses in which each pathway is individually perturbed.

Veil Retraction

Although fibroblast motility was originally described in terms of alternating phases of protrusion and retraction (Abercrombie et al., 1970; Abercrombie et al., 1971), the protrusion phase has received most attention while the retraction phase has been relatively understudied. To our knowledge, no detailed kinetic-structural studies at the supramolecular level have been carried out on retraction in any cell system. One reason for this may be that in non-neuronal cells the lamellipodium overlaps spatially with the

lamellum (Gupton et al., 2005), thus obscuring clear views of the lamellipodium in retraction.

In the growth cone, in contrast to fibroblasts, the motility machinery is separated from the remainder of the organelles and nucleus in the cell body. Growth cones microsurgically severed from the cell body have the capacity to continue to move (Bray et al., 1978). Thus, the motility machinery of the growth cone, to a first approximation, is autonomous. The spatial separation and local autonomy of the growth cone may provide unique advantages for studying the motility machinery in general and retraction in particular.

Previous studies have characterized the growth cone in terms of peripheral, actin rich, and central, microtubule rich, domains with a transitional domain defining the boundary between them (Bridgman and Dailey, 1989; Forscher and Smith, 1988; Smith, 1988). Veils are considered to be in the actin-rich, peripheral domain. However, previous studies have not attempted to seek distinctions in structure between protruding and retracting veils.

Our results showed that retracting veils, in contrast to protruding veils, contain a sparse array of long actin filaments and that some of these filaments tend to run parallel to the retracting cell perimeter and are organized into bundles. Typically, the retracting edge was concave and the actin bundles paralleled this edge. Analysis of the transition from the protrusion phase to the retraction phase indicated that the dense, dendritic network of the protrusion phase was lost rapidly (within tens of seconds) after the retraction phase began. The kinetics of this loss are consistent with an array

treadmilling mechanism (Pollard and Borisy, 2003) in which polymerization at the barbed end of actin filaments near the membrane is turned off; continued depolymerization at the pointed end would then result in disappearance of the dense, branched network and represent the initial phase of veil retraction. The remaining, long filaments presumably provide mechanical connection between the retracting edge and the deeper cytoplasm. Edges that continue to retract continue to show the sparse array of long filaments. Although this mode of organization may be unique to retracting veils of neuronal growth cones, it also seems possible that this is a general pattern of organization that is present in fibroblasts and other motile cells but which is simply more clearly visualized in neurons.

The mechanism responsible for formation of the parallel bundled filaments underlying the membrane in veil retraction has not been investigated but may be related to the edge actin bundles originally described by Albrecht-Buehler (Zand and Albrecht-Buehler, 1989) or it may be related to the phenomenon of retrograde flow and to forces generated by myosin II. Once actin polymerization is blocked at the leading edge, the actin filament network rapidly flows backwards with retrograde flow; inhibition of myosin II in neurons blocks retrograde flow in the transitional domain, and leads to a 50% decrease in retrograde flow in the peripheral domain (Medeiros et al., 2006). Myosin II has been immunolocalized to the central and transitional regions of the growth cone, and has also been localized at the edge of retracting veils (Rochlin et al., 1995). Further, myosin II has been correlated with formation of parallel bundles at the rear of the dendritic network in keratocytes (Svitkina et al., 1997). Taken together, these results

point to an important role for myosin II in continued veil retraction. Our electron microscopy results show that the actin network, a few microns behind the protruding edge, is already quite sparse. The combination of a sparse network, rapid retrograde flow, and myosin-driven bundling could provide an explanation for the observed supramolecular organization found in retracting veils of growth cones.

Veil Formation on Filopodia

Our results suggest that filopodia demarcate boundaries between veils and have the capacity to initiate the formation of nascent veils. Our light microscopic observations revealed that most veils were associated with at least one filopodium, which were consistent with the literature (Goldberg and Burmeister, 1986), whereas the ability of adjacent veils to behave independently while sharing a single filopodium was a novel result. Frequently, veils were observed protruding on one side of a filopodium while retracting on the other side. In such cases, electron microscopy revealed a dramatically different mode of actin organization on either side of the filopodium,--dense, branched network on the protruding side and sparse network on the retracting side. Filaments from one veil did not appear to extend over the shaft to interact with filaments of the adjacent veil. Thus, the supramolecular organization seen in these veils supports the idea of locally independent units of veil behavior.

Beyond demarcating boundaries between veils, filopodia appear to also play an active role in veil formation. Routinely, we observed in phase contrast time-lapse sequences that veils would be initiated along filopodial shafts or in the “crotch” of forked

filopodia, far from the growth cone or nearby veils. In all cases evaluated by correlative electron microscopy, the veil was revealed to contain a dense, branched actin network, enriched in Arp2/3 and associated with the filaments in the filopodium. Filaments in the veil were frequently seen branching off filaments in the filopodial shaft at an angle suggestive of Arp2/3 nucleation. This result was initially surprising since Arp2/3 was not previously thought to be present in filopodia, though at least one of its activators had been localized there (Nozumi et al., 2003). Our results carry implications for veil formation and current models for lamellipodial formation as well.

Nucleation of actin filaments off of filopodial filaments presumably represents nucleation on the side of actin filaments. Although actin filaments have been demonstrated to support side branching in vitro (Higgs and Pollard, 1999; Higgs and Pollard, 2001; Mullins et al., 1998), the typical situation in vivo restricts branching to sites near the barbed ends of actin filaments in close proximity to the cell membrane because that is where activators of Arp2/3 are located (Pantaloni et al., 2000; Pantaloni et al., 2001; Wiesner et al., 2003). The appearance of actin filaments branching from the sides of filopodia has not previously been reported in vivo. Filaments in filopodia are thought to be long with their barbed ends near the filopodial tip. Veil formation along the length of filopodia, therefore, may be a realization of the capacity of actin filaments to support side branching. From these results we can expand upon the convergent elongation model for filopodia formation (Vignjevic et al., 2003) that accounts for the emergence of bundled filaments from the dendritic network. Our data add to this model the possible re-emergence of a branched network from filopodia – allowing the filopodia

to continue to interact with both the network from which it formed and the new one which it initiates.

An additional caveat is that veil formation off the side of filopodia could potentially influence the shape of the leading edge of the veil. Veil initiation along a filopodium shaft would begin protruding distal to the leading edge of the connected veil, creating the observed concave protruding edge. It has been reported that adhesions along the filopodial shaft regulate veil advance along filopodia, and this could be a possible mechanism by which this occurs (Steketee and Tosney, 2002). Taken together, veil protrusion and veil formation on filopodia allow the creation of great diversity of form from a very basic organization of the actin cytoskeleton (Fig. 9).

In summary, our results suggest that the plasticity of growth cone motility arises at the level of individual veils associated with filopodia within the growth cone. Individual veils exhibit directional instability, alternating between rapid phases of protrusion and retraction. This property allows for focal response to the encountered environment. Since the growth cone is composed of an ensemble of protruding and retracting veils, net growth cone advance may be considered the vector sum of all veils' motility behavior in response to their local environments. Filopodia play a key role in delimiting veils and serving to nucleate the formation of new veils. In the case of the path finding growth cone, this system is particularly economical. It allows exploration of the environment by numerous long filopodia, selective protrusion along the filopodia that find a good path, and rapid disassembly of veils that protruded along a non-productive path.

CHAPTER 3

ADDITIONAL DOCUMENTATION OF THE PROTRUSION-WITHDRAWAL CYCLE

3.1 Introduction:

The correlative light and electron microscopy studies presented in the previous chapter were the result of imaging numerous growth cones and resulted in a collection of more than 700 EMs. More figures were assembled as we evaluated the data than could be included in the published work. We include here additional examples of the protrusion and withdrawal cycle observed in our correlative studies. This documentation is intended as a record of the quality of the full data set, comprising 21 growth cones containing 185 veils individually characterized using CorEM.

3.2 Filopodia Associated Veil Protrusion

In the previous chapter we showed that 74% of protruding veils occurred between two filopodia less than 2.5 μm apart (Figure 7B).

Figure 19 shows a veil that just began to protrude from the crotch of two filopodia after the last live image. In this example, the region surrounding the filopodia roots was actively retracting throughout the time lapse. The veil itself contains a dense dendritic network, and filaments from the network appear to both branch off of, and merge into, the filopodial shafts.

Figure 20 shows a series of three adjacent, simultaneously protruding filopodia delimited veils that were protruding at the start of the time lapse and continued to protrude for the next 60 seconds until extraction. In the low magnification EM arrows mark a long filopodia that clearly demarcates the adjacent veils. In the high magnification EM the network is dense and dendritic, and few filaments cross over the filopodial shaft.

Figure 21 and Figure 22 show two filopodia associated veils that protruded along filopodia whose tips fused together, either as the veil protruded along it's length (Figure 22), or before the veil protruded (Figure 23). In both cases the observed actin network is dendritic, and shows clear interaction between the filopodia and the veil.

Figure 23 shows a small filopodia associated veil at the rear of the growth cone that was protruding in the direction opposite of growth cone advance, while the veils on either side retracted.

Figure 19 Filopodia Associated Veil Protrusion 1

A. The last live image of the growth cone before extraction. White box denotes the region of interest. **B.** Time-lapse image sequence of region of interest. **C.** Overlays showing the amount of veil protrusion (appears red) over the last 6 seconds before extraction (upper merge) and from the last live frame until extraction (lower merge). **D.** Low magnification platinum replica electron micrograph (EM) of the region of interest. **E.** High magnification of very young filopodia associated veil marked in D that began to protrude after the last live frame, at the junction of two filopodia roots. The older portion of the veil, at the junction of the filopodia, has been cleared out and only horizontal filaments remain. Filaments at the leading edge are highly branched.

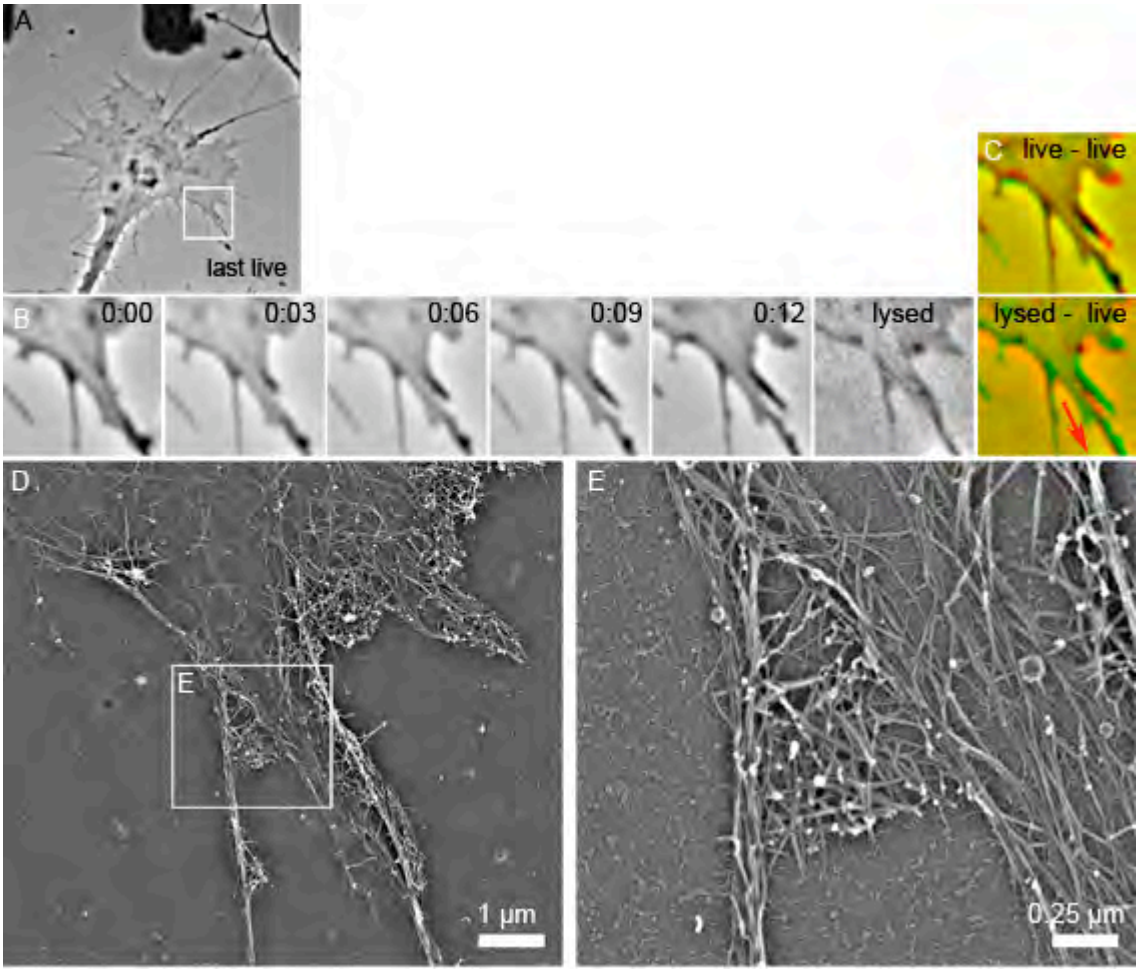
A
last live
C live - live
B
0:00
0:03
0:06
0:09
0:12
lysed
lysed - live
D
E
1 µm
E
0.25 µm

Figure 20 Filopodia Associated Veil Protrusion 2.

A. The last live image of the growth cone before extraction. White box denotes the region of interest. **B.** Time-lapse image sequence of region of interest. Upper time-lapse shows the initiation of the upper left veil shown that is cut-off in the lower time-lapse (box is acquired from region slightly up and to the left of the box to show the veil). **C.** Overlays showing the amount of veil protrusion (appears red) over the last 6 seconds before extraction (upper overlay) and from the last live frame until extraction (lower overlay). **D.** Low magnification platinum replica electron micrograph (EM) of the region of interest. Arrows mark the tightly bundled shaft of the older filopodium that extends more than 7 μm back through the veil. The veils on either side of the filopodium do not appear to cross over from one side to the other. **E.** High magnification of protruding convex edge of filopodia associated veil marked in D.

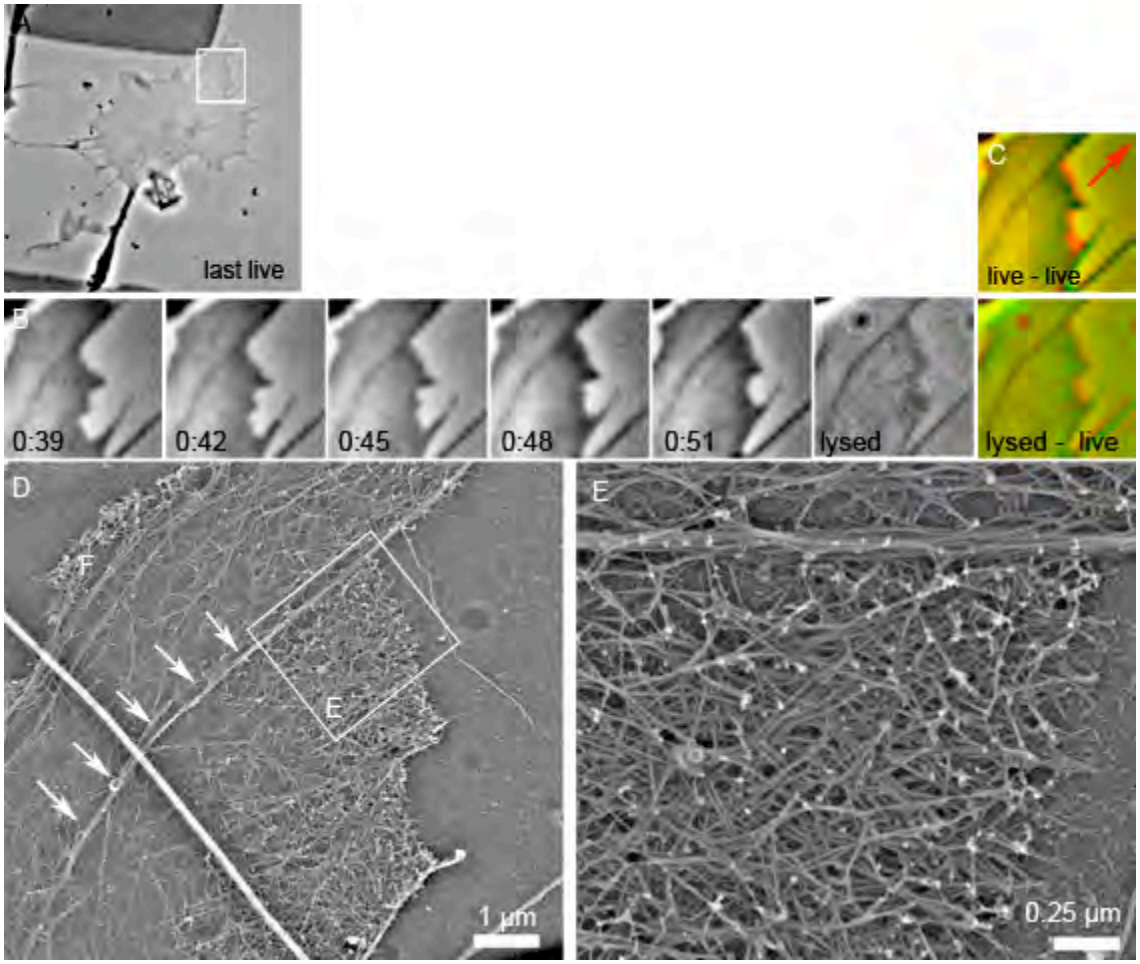
A
last live
C
live - live
B
0:39
0:42
0:45
0:48
0:51
lysed
lysed - live
D
F
E
1 µm
E
0.25 µm

Figure 21 Filopodia Associated Veil Protrusion 3.

A. The last live image of the growth cone before extraction. White box denotes the region of interest. B. Time-lapse image sequence of region of interest. C. Overlays showing the amount of veil protrusion (appears red) over the last 6 seconds before extraction (upper overlay) and from the last live frame until extraction (lower overlay). D. Low magnification platinum replica electron micrograph (EM) of the region of interest. E. High magnification of convex filopodia associated veil marked in D. In this case, the tip of the right filopodium merges with the shaft of the left one before the veils begins to protrude up between them

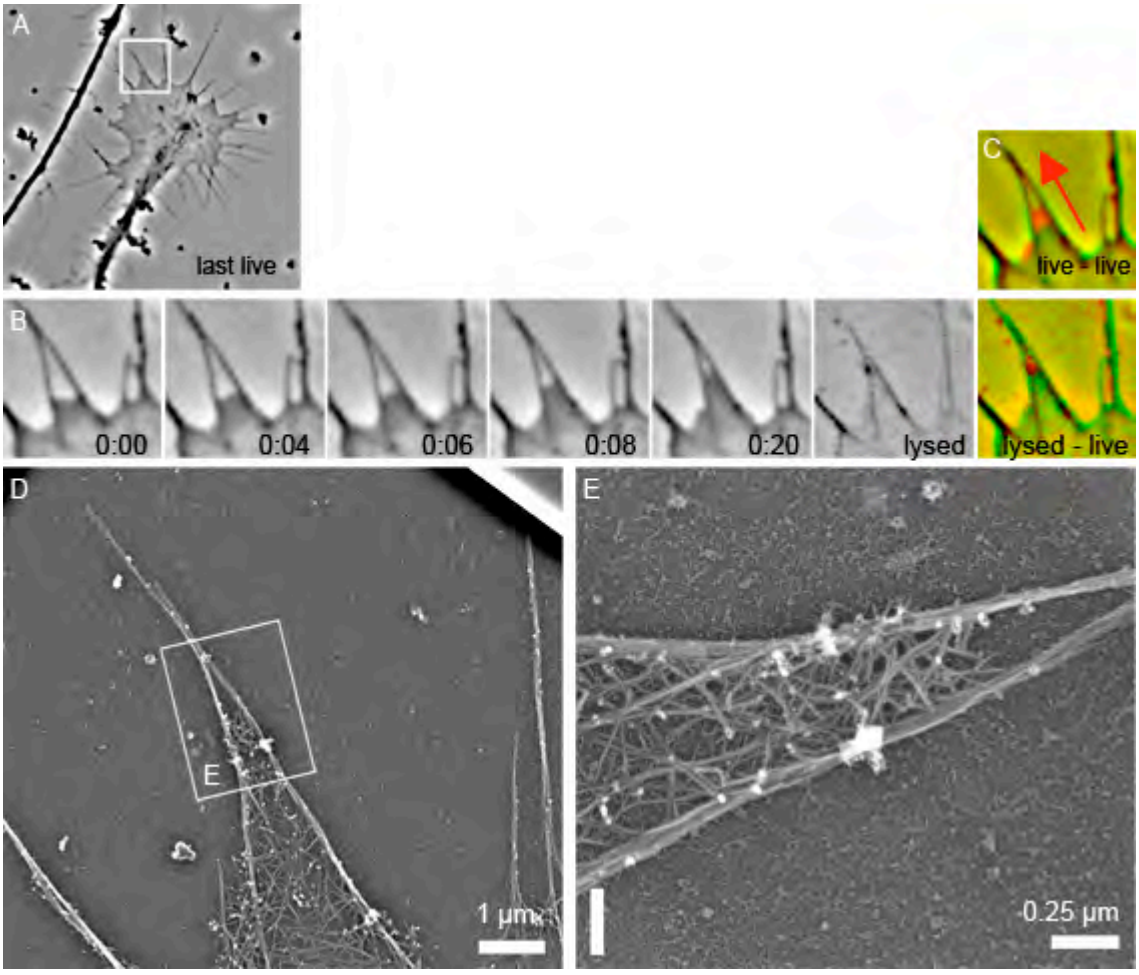
A
last live
C
live - live
B
0:00
0:04
0:06
0:08
0:20
lysed
lysed - live
D
E
1 µm
E
0.25 µm

Figure 22 Filopodia Associated Veil Protrusion 4.

A. The last live image of the growth cone before extraction. White box denotes the region of interest. **B.** Time-lapse image sequence of region of interest. Red arrows mark protruding veil of interest. White arrowhead points at angle of lower filopodium whose angle of protrusion is shifted upwards as the veil protrudes along it. **C.** Overlay showing the amount of veil protrusion (appears red) over the last 6 seconds before extraction. **D.** Low magnification platinum replica electron micrograph (EM) of the region of interest. **E.** High magnification of convex filopodia associated veil marked in D. The tips of the filopodia meet and fuse together. In this case the fusion occurs as the veil protruding up between the filopodia reaches the fusion point. The thin network makes it easier to discern the numerous filaments that criss-cross from one side of the veil to the other, appearing to add into the filopodium on the opposite side.

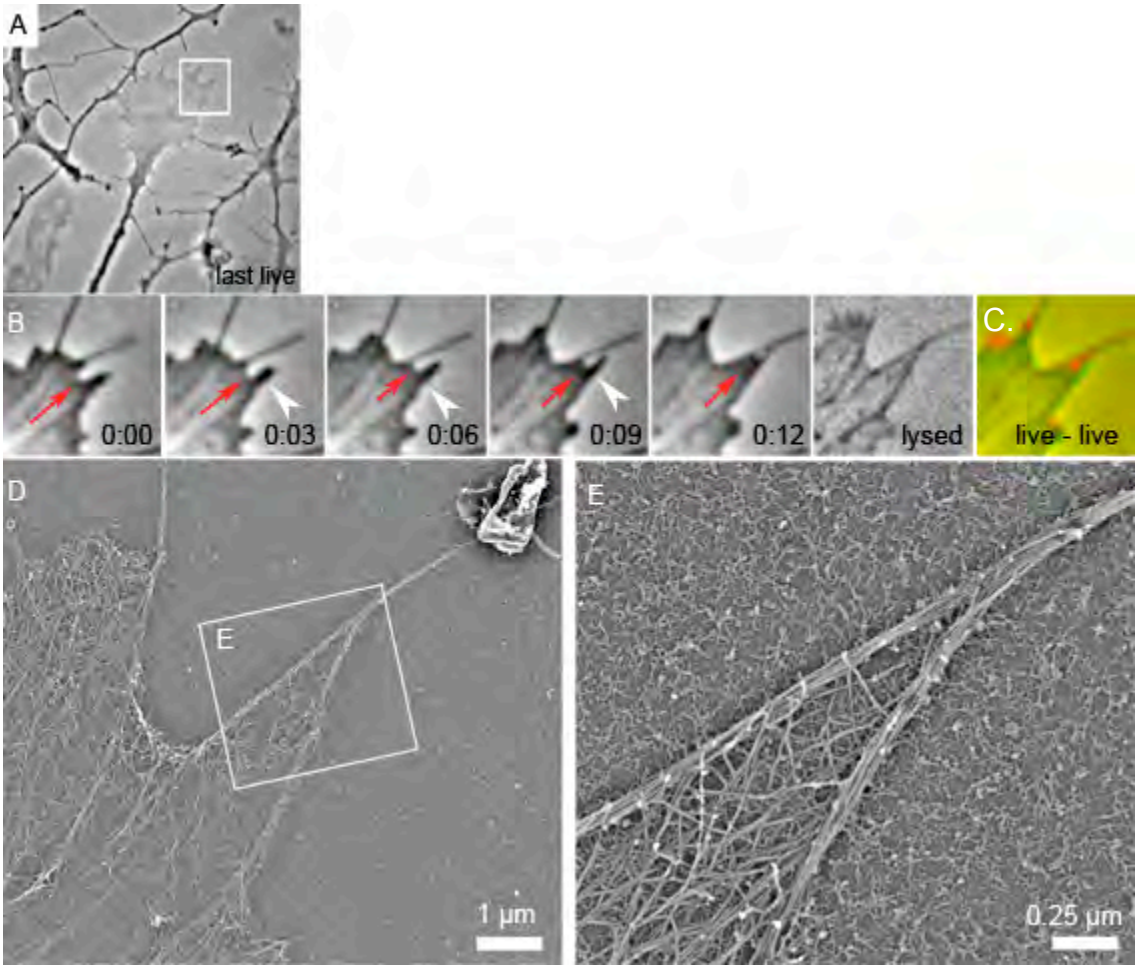
A
last live
B
0:00
0:03
0:06
0:09
0:12
lysed
C.
live - live
D
E
1 µm
E
0.25 µm

Figure 23 Filopodia-associated veil protrusion distal to the growth cone.

A. The last live image of the growth cone before extraction. White box denotes the region of interest. **B.** Time-lapse image sequence of region of interest. Black arrow denotes body of growth cone retracting away from filopodia. Red arrow marks small veil **C.** Low magnification platinum replica electron micrograph (EM) of the region of interest. **D.** High magnification of small veil that protruded up two filopodia, and continued to protrude after retraction of the growth cone edge fused the filopodia together behind it.

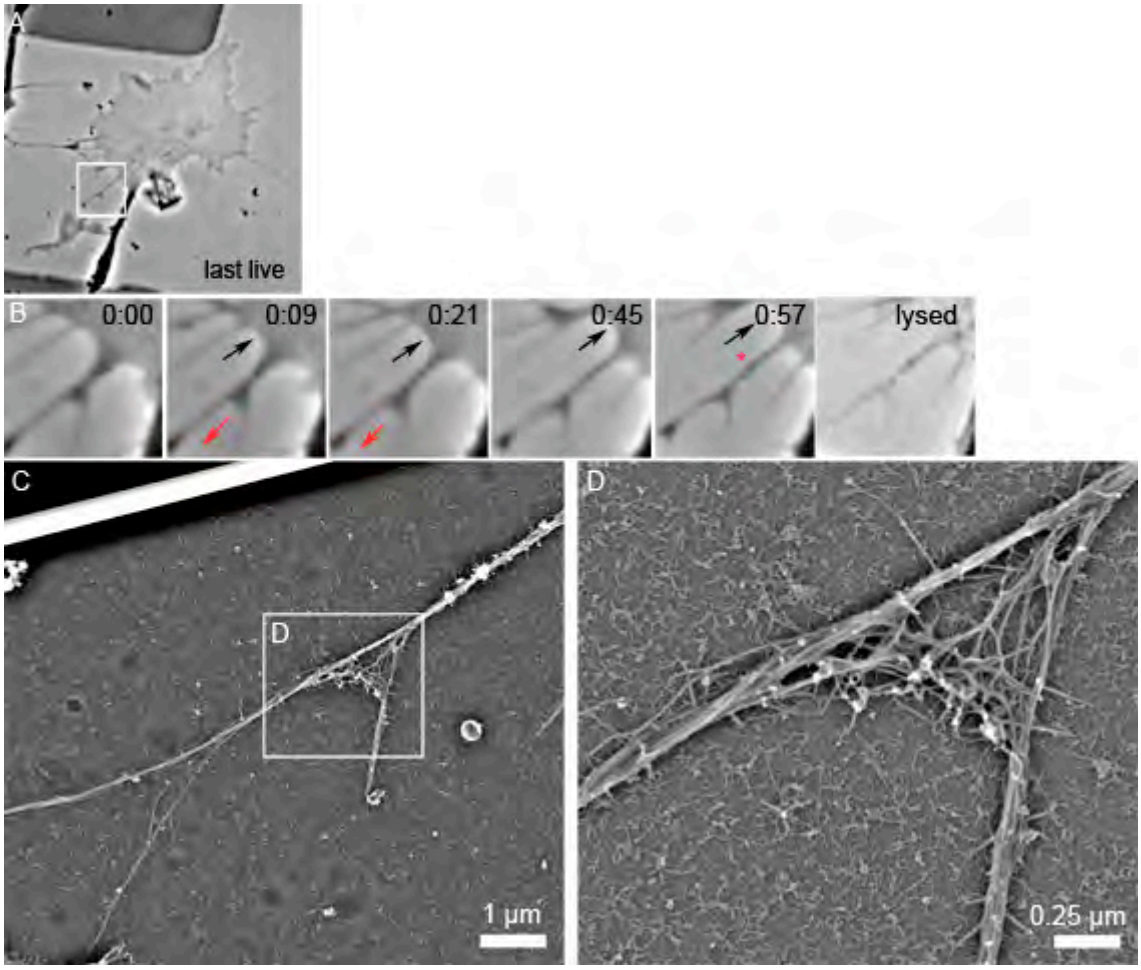
A
last live
B
0:00
0:09
0:21
0:45
0:57
lysed
C
D
1 µm
D
0.25 µm

3.3 Veil Retraction

In Chapter 2 we showed that retracting veils, in contrast to protruding veils, contain a sparse array of long actin filaments and that some of these filaments tend to run parallel to the retracting cell perimeter and are organized into bundles.

Figure 24 shows a small veil, at the front of the growth cone, which began to retract 6 seconds before extraction, while a new veil began to protrude off of the filopodium to its left. In this short time span, bundled filaments have already begun to appear at the membrane edge, and the network behind the membrane has thinned considerably and is filled with long filaments.

Figure 24 Veil Retraction at the front of the growth cone

A. The last live image of the growth cone before extraction. White box denotes the region of interest. **B.** Time-lapse image sequence of region of interest. Red arrows mark protruding filopodium. Green arrows marks retracting veil. **C.** Overlays showing the amount of veil retraction (appears green) over the last 6 seconds before extraction (upper overlay, arrow marks veil retraction) and from the last live frame until extraction (lower overlay). **D.** Low magnification platinum replica electron micrograph (EM) of the region of interest. **E.** High magnification of retracting region boxed in D. The roots of the filopodium that protruded have replaced the leading edge, and only a few short, branched filaments remain.

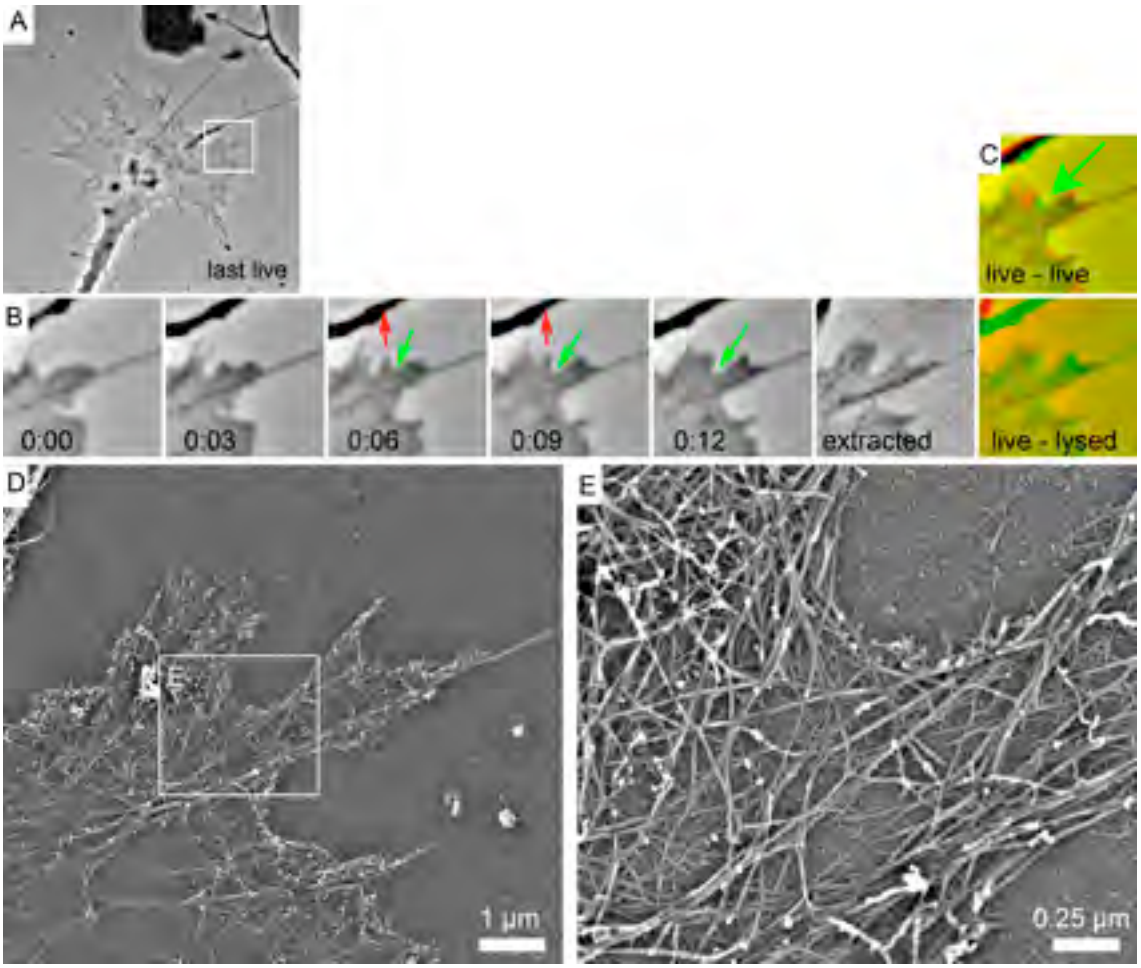
A
last live
C
live - live
B
0:00
0:03
0:06
0:09
0:12
extracted
live - lysed
D
E
1 µm
E
0.25 µm

3.4 Veil Protrusion Along a Single Filopodium

Veil protrusion along a single filopodium is a rare event that occurred on about the same order of magnitude as non-filopodia associated veils. The ultrastructure of these veils was dendritic, however the lack of a second filopodium resulted in a directional organization of the filaments within the network that appeared different from either the filopodia associated or non-filopodia associated veils.

Figure 25 shows a veil that protrudes for ~10 seconds up the side of a filopodium at 10-12 μm/min. The veil is long and narrow, but still contains a dense dendritic network. Some branches have been pseudocolored pink for easier visualization. At the top of the veil, some filaments along the outer edge become loosely bundled together. At the base of the veil (Figure 25F), the network is very sparse, showing the rapidity with which the dendritic network can be cleared following veil protrusion.

Figure 25 Veil Protrusion along a Single Filopodium

A. The last live image of the growth cone before extraction. White and yellow boxes denotes the region of interest. **B.** Time-lapse image sequence of region of interest. (*) marks the beginning of veil protrusion, red arrow marks process of veil along filopodium. **C.** Overlays showing the amount of veil protrusion (appears red) over the last 6 seconds before extraction (upper overlay, arrow marks veil protrusion) and from the last live frame until extraction (lower overlay – * marks new veil formation, arrow denotes direction of veil protrusion). **D.** Low magnification platinum replica electron micrograph (EM) of the region of interest. **E.** High magnification of veil protruding along single filopodium marked in D. White arrows mark the free edge of the veil, and above that point, the free edge becomes bundled. **F.** High magnification of base of veil that has since thinned out, showing many branches that come off the main filopodium. **G.** High magnification of boxed region in E with branched filaments pseudocolored. There is a high density of branches off filaments next to the main filopodium, and many filaments appear to merge or terminate into the filopodium.

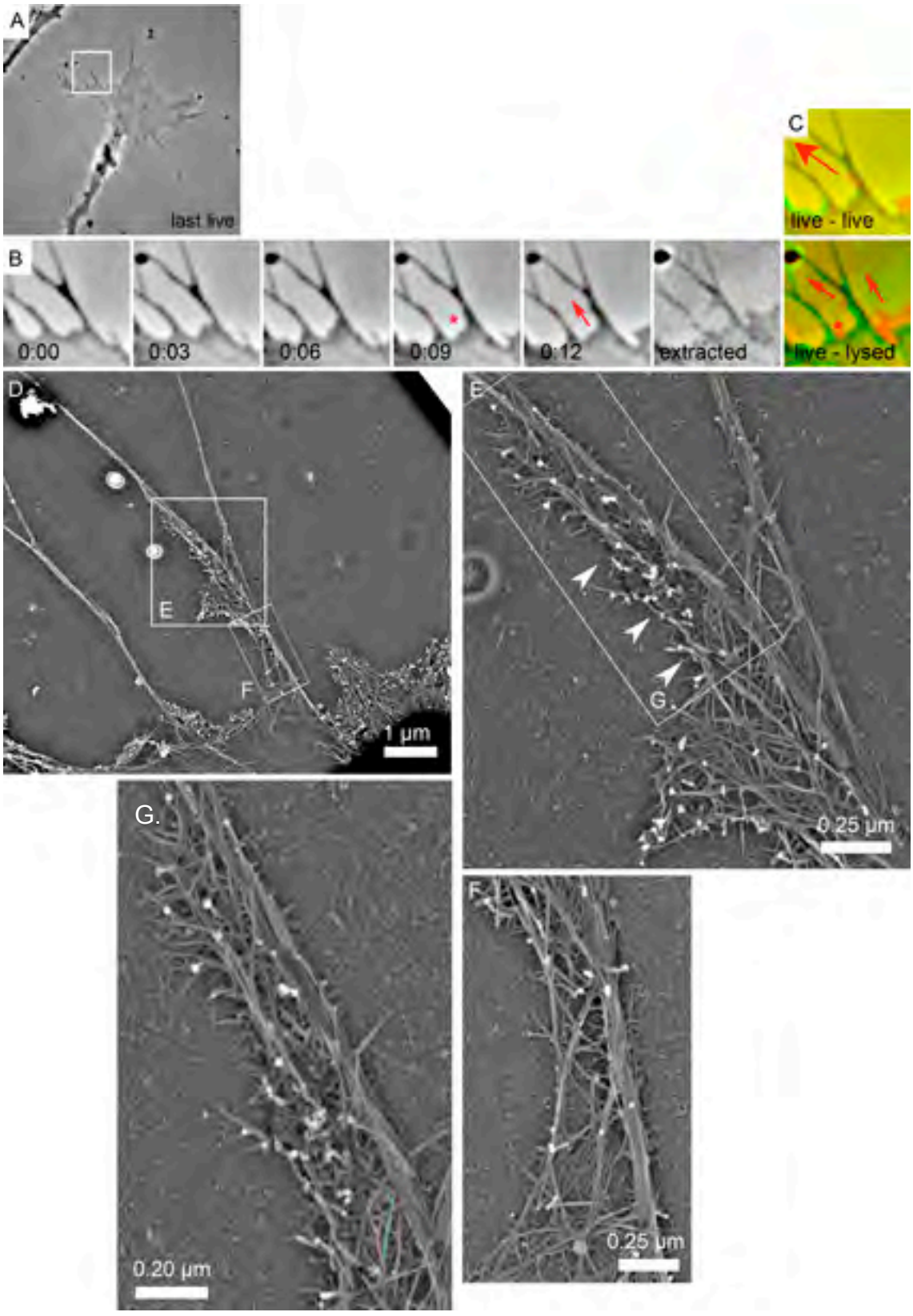
A
last live
C
live - live
B
0:00
0:03
0:06
0:09
0:12
extracted
live - lysed
D
E
F
1 µm
E
G.
0.25 µm
G.
0.20 µm
F
0.25 µm

s

3.5 Filopodia Independent Veil Protrusion.

Typical filopodia independent veil protrusion contains a network whose organization closely resembles the lamellipodia seen in fibroblasts and keratocytes (Svitkina and Borisy, 1999). Figure 26 shows a filopodia independent veil that protruded for the entire minute it was observed until extraction at 4.3 μm/min. The network contains a mixture of long and branched filaments woven together into a dense network. Insets showed pseudocolored y junctions present at the leading edge.

Figure 27 shows a non-filopodia delimited veil that had been protruding for approximately 18 seconds at the time of extraction. The veil protruded rapidly during the time shown in the image sequence, filling in a v-shaped gap at the front edge of the growth cone. In this example, the leading edge is not smooth and instead juts sharply outward. The boundary between newer and older region (white arrows, inset F) of the network is not demarcated as sharply as those seen in filopodia-associated protrusion, but is still visible.

Figure 26 Filopodia Independent Veil Protrusion 1

A. The last live image of the growth cone before extraction. White box denotes the region of interest. **B.** Time-lapse image sequence of region of interest. **C.** Overlays showing the amount of veil protrusion (appears red) over the last 6 seconds before extraction (upper overlay) and from the last live frame until extraction (lower overlay). **D.** Low magnification platinum replica electron micrograph (EM) of the region of interest. **E.** High magnification of longstanding non-filopodia associated veil marked in D with flat leading edge. **F.** Another high magnification of longstanding non-filopodia associated veil marked in D with convex leading edge. Individual Y branches are boxed and pseudocolored in blue for better visualization in a and b to the left

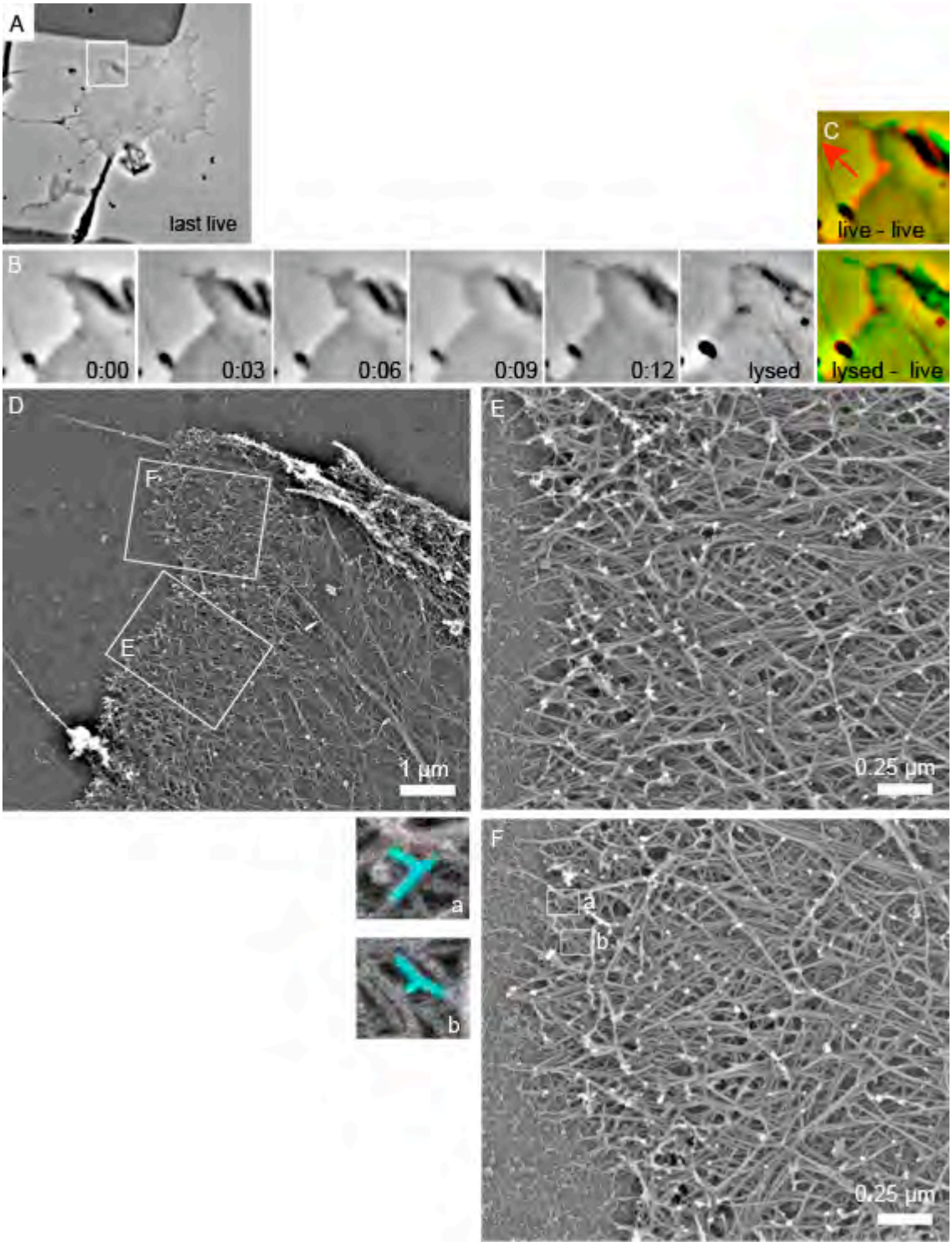
A
last live
C
live - live
B
0:00
0:03
0:06
0:09
0:12
lysed
lysed - live
D
F
E
1 µm
E
0.25 µm
a
b
F
a
b
0.25 µm

Figure 27 Filopodia Independent Veil Protrusion 2

A. The last live image of the growth cone before extraction. White box denotes the region of interest. **B.** Time-lapse image sequence of region of interest. **C.** Overlays showing the amount of veil protrusion (appears red) over the last 6 seconds before extraction (upper overlay) and from the last live frame until extraction (lower overlay). **D.** Low magnification platinum replica electron micrograph (EM) of the region of interest. **E.** High magnification of ~18 second old filopodia independent veil marked in D. The leading edge is not smooth, and the network appears somewhat disorganized. **F.** High magnification of boundary between the new veil growth and sparse older region from which it arose.

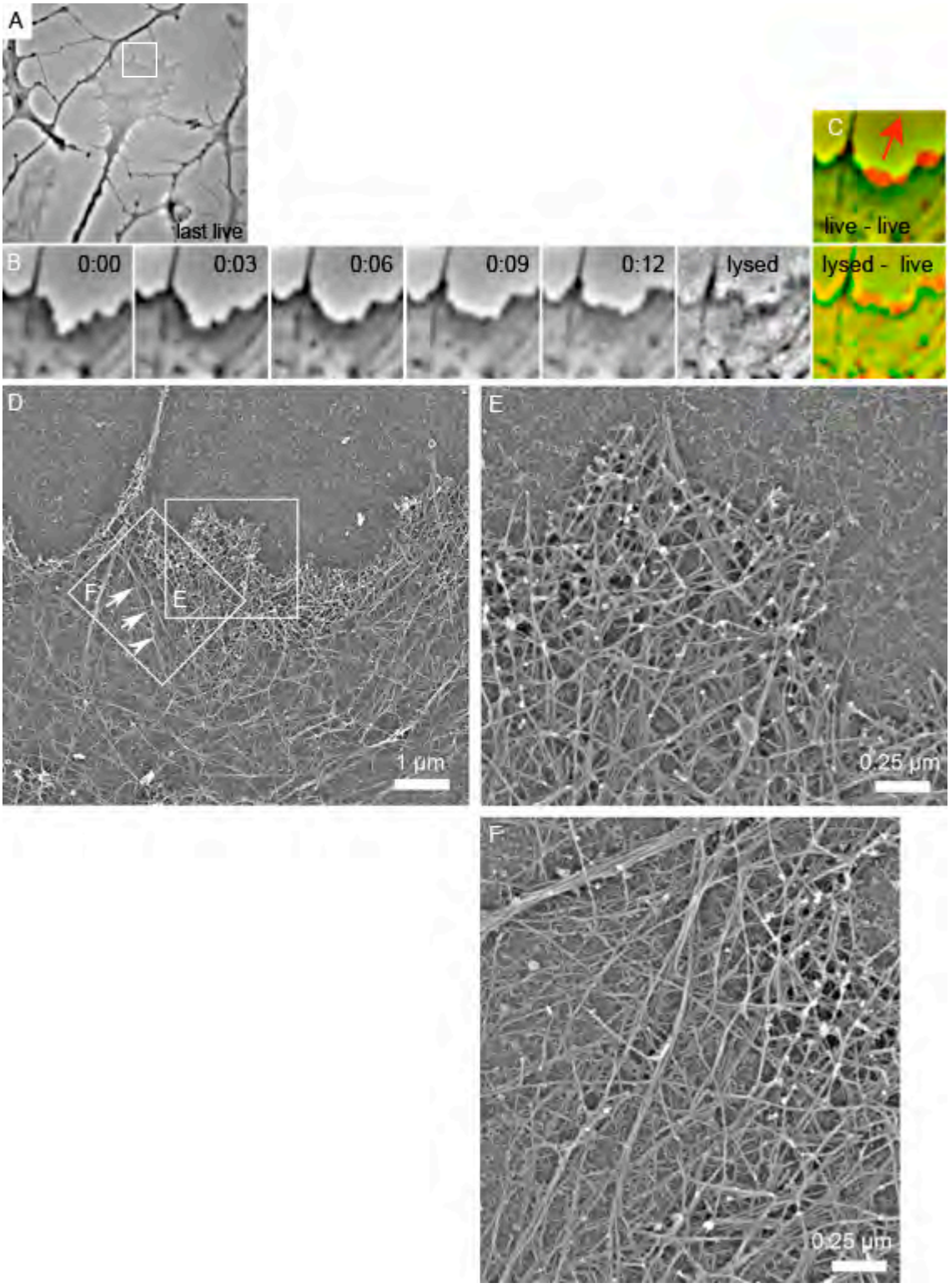
A
last live
C
live - live
B
0:00
0:03
0:06
0:09
0:12
lysed
lysed - live
D
F
E
1 µm
E
0.25 µm
F
0.25 µm

3.6 Arp2/3 Localization.

Figure 28 shows additional examples of p16, p34, and Arp3 immunostaining in chick DRG growth cones. Localization of all three antibodies is seen at the leading edge of growth cone.

Figure 29 shows a very young filopodia delimited veil that began to protrude after the last live image (~ 4 seconds) between two filopodia roots. The network is less than 0.5μm deep, and is very densely branched. Immunogold labeling is seen throughout the leading edge of the veil.

In Figure 30 the lower veil retracted for approximately 48 seconds before extraction. Mainly parallel bundled filaments are seen at membrane edge. Immunogold labeling is only seen along the bundled edge where remnant of the dendritic network remains. Almost no gold label was seen in the remainder of the veil.

Figure 31 shows two filopodia whose tips crossed over one another ~50 seconds prior to extraction, while they both continued to elongate. ~24 seconds later a phase dense spot appeared at the intersection between the two shafts that continued to enlarge and grow denser until extraction. In the EM, there is a small dendritic ‘bush” (marked by *) sprouting from the upper filopodium, at the point corresponding to the phase dense spot. Arp3 immunogold staining labels the filaments in the “bush” and is also seen on the filopodium shaft above and below the point where the filaments were loosened (pseudocolored yellow in F). Inset G shows an enlargement of an actin filament from the “bush” that has two branches with a gold particle labeling the crotch of each branch.

Figure 28 Immunostaining of Veils for Arp 2/3 Complex Subunits

Immuno-fluorescent staining against three Arp2/3 complex subunits in chicken dorsal root ganglion neurons ~ 24 hours after plating. Phalloidin stains actin filaments and the merge shows the colocalization.

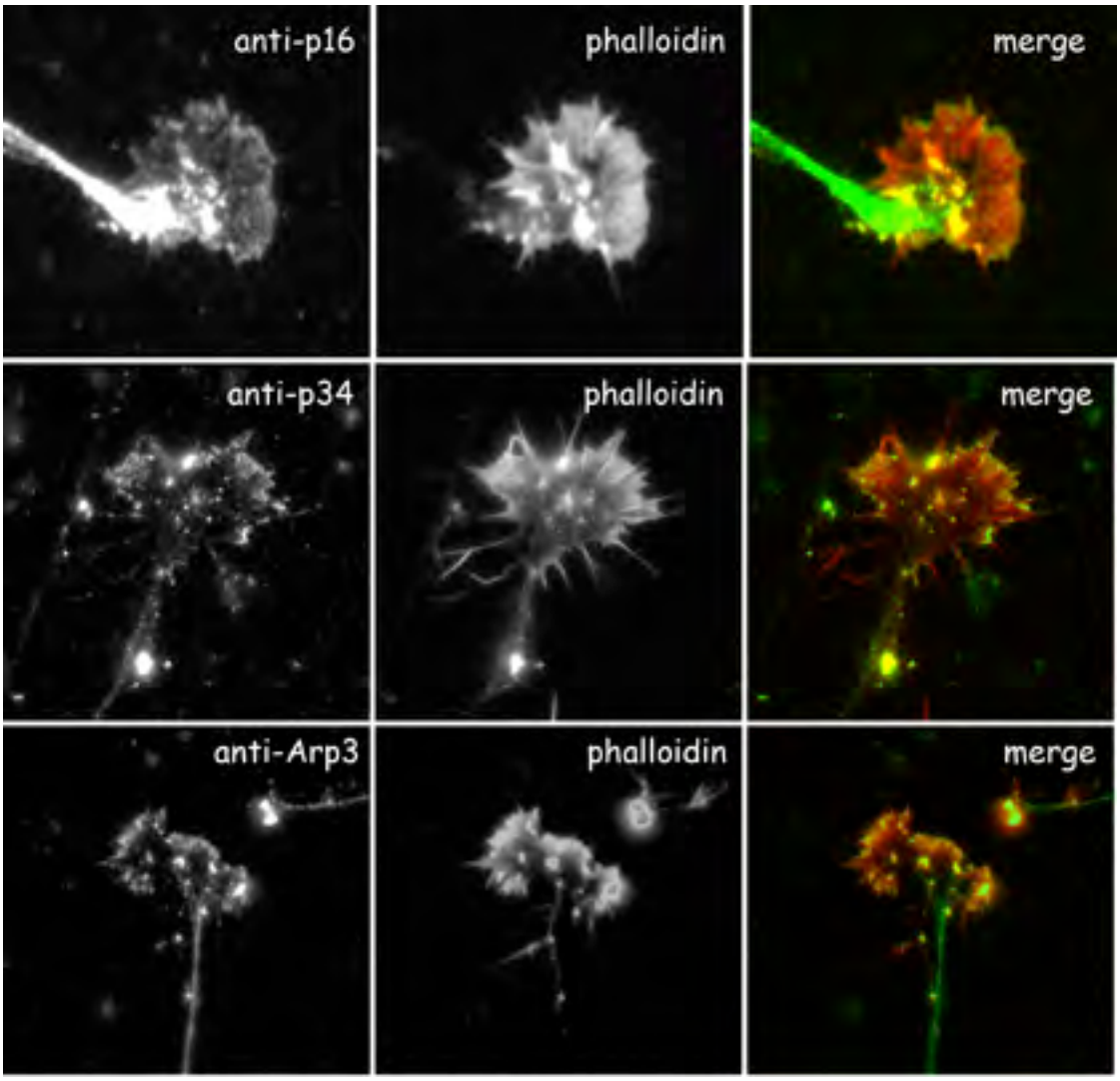
anti-p16
phalloidin
merge
anti-p34
phalloidin
merge
anti-Arp3
phalloidin
merge

Figure 29 Veil Protrusion with Arp3 Immunogold Staining

A. The last live image of the growth cone before extraction. White box denotes the region of interest. **B.** Time-lapse image sequence of region of interest. **C.** Overlays showing the amount of veil protrusion (appears red) over the last 6 seconds before extraction (upper overlay) and from the last live frame until extraction (lower overlay). **D.** Low magnification platinum replica electron micrograph (EM) of the region of interest. **E.** High magnification of a young veil that is initiated off filopodia roots n the last seconds before extraction (boxed in D), and immuno-electron stained against Arp3 (gold particles are pseudocolored yellow)

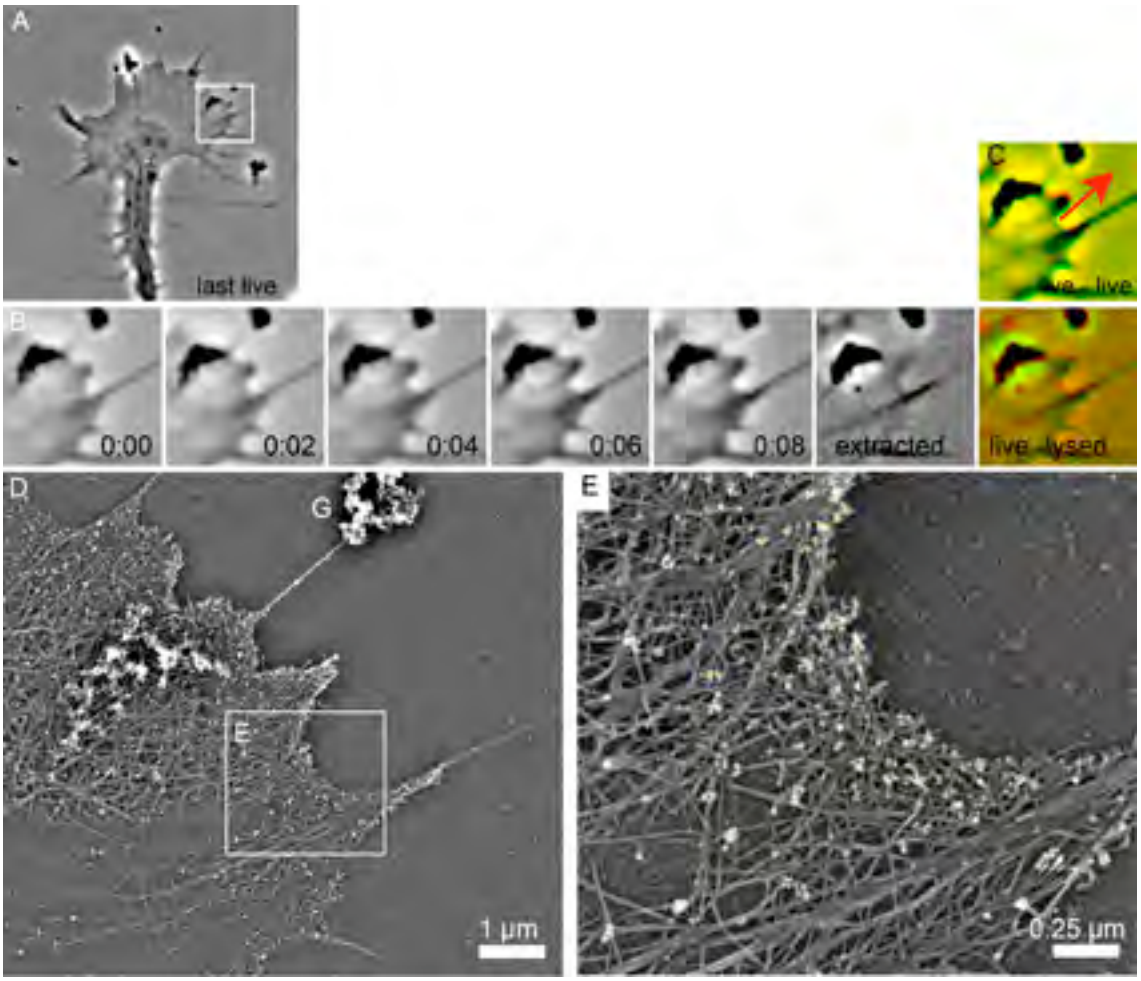
A
last live
C
B
0:00
0:02
0:04
0:06
0:08
extracted
live -lysed
D
G
E
1 µm
E
0.25 µm

Figure 30 Veil Retraction with Arp3 Immunogold Staining

A. The last live image of the growth cone before extraction. White box denotes the region of interest. **B.** Time-lapse image sequence of region of interest. **C.** Overlays showing the amount of veil retraction (appears green) over the last 6 seconds before extraction (upper overlay) and from the last live frame until extraction (lower overlay). **D.** Low magnification platinum replica electron micrograph (EM) of the region of interest. **E.** High magnification of the upper retracting veil that had been retracting for about 19 seconds (boxed in D), and immuno-electron stained against Arp3 (gold particles are pseudocolored yellow) Some branched filaments remain at the leading edge and stain with gold. This region is about 0.1-0.25 μm deep. Beyond that, long horizontal filaments remain, and there are large gaps in the network. **F.** High magnification of the lower retracting veil that had been retracting for about 48 seconds. The leading edge is almost entirely bundled, and very few tiny branches remain. .

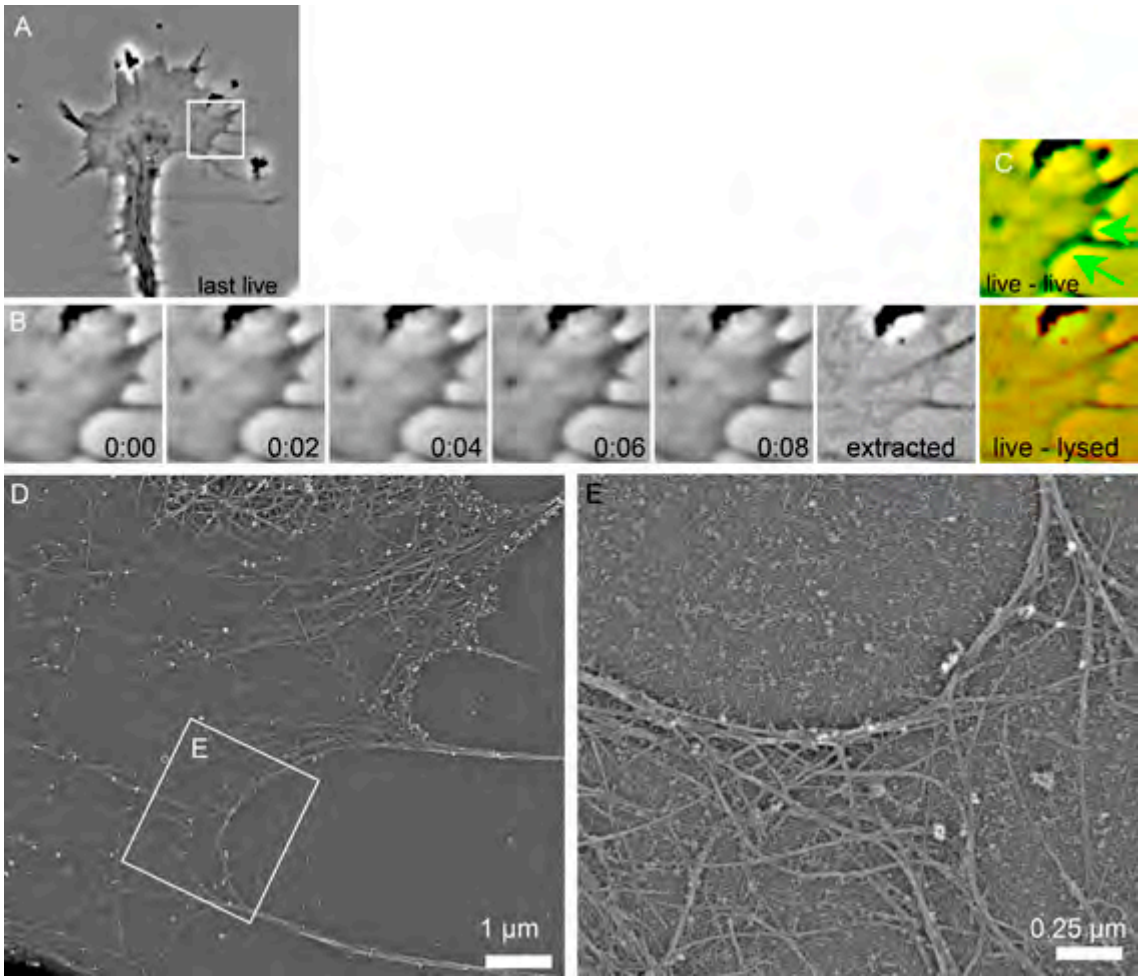
A
last live
C
live - live
B
0:00
0:02
0:04
0:06
0:08
extracted
live - lysed
D
E
1 µm
E
0.25 µm

Figure 31 De Novo Veil Formation Between Filopodia Shafts

A. The last live image of the growth cone before extraction. White box denotes the region of interest. **B.** Time-lapse image sequence of region of interest. (*) marks phase dense spot. **C.** Overlays showing the amount of veil protrusion (appears red) over the last 6 seconds before extraction (upper overlay) and from the last live frame until extraction (lower overlay). **D.** Low magnification platinum replica electron micrograph (EM) of the region of interest. **E.** High magnification of mid-size veil that was initiated de novo at the junction of two filopodia. In the time lapse, the phased dense spot gradually expands and darkens. White arrows mark the outpouching of filaments from the filopodium that become branched in the veil. **F.** High magnification of the veil itself, with Arp3 immunogold labeling (pseudocolored yellow). **G.** High magnification of actin filament with gold particles localized to Y junctions boxed in F.

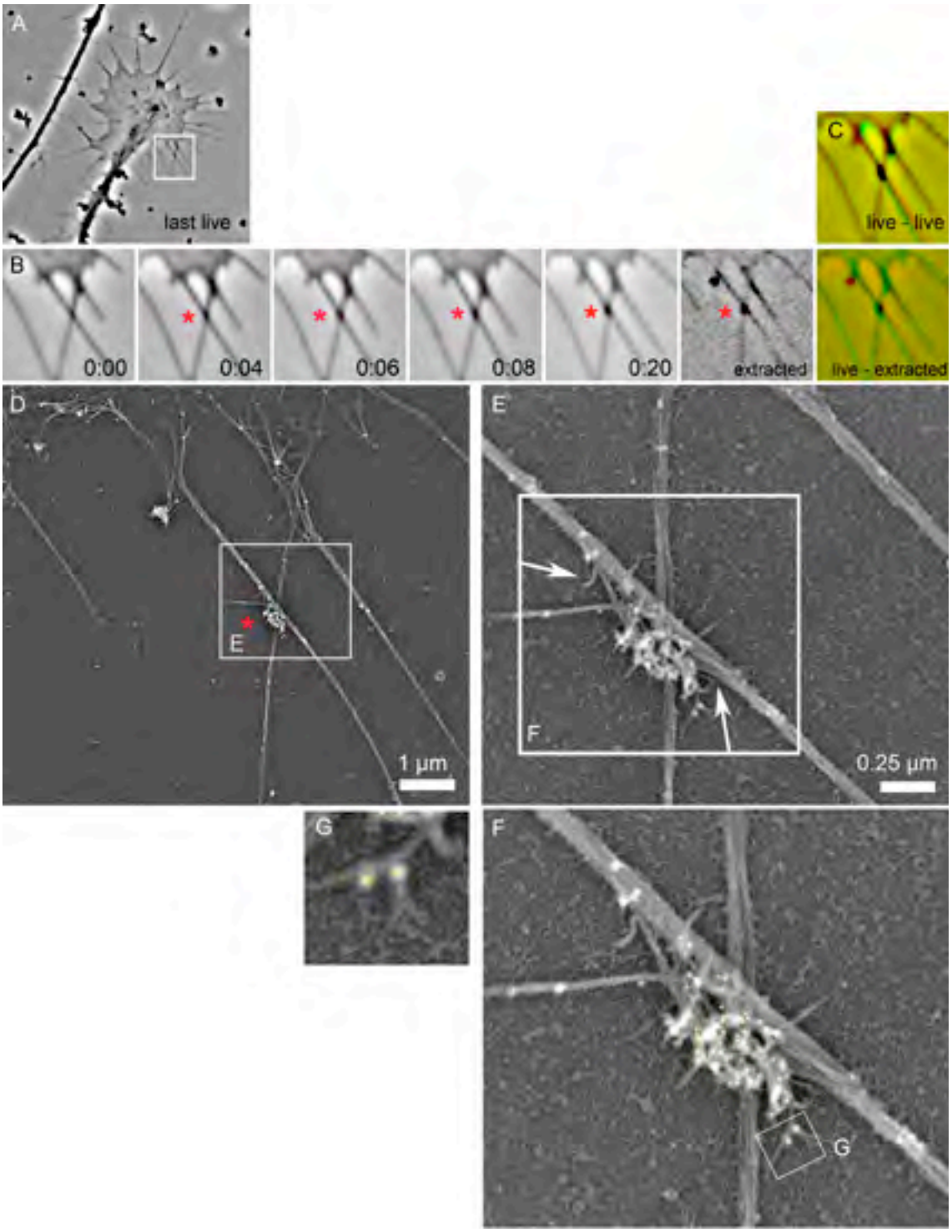
A
last live
C
live - live
B
0:00
0:04
0:06
0:08
0:20
extracted
live - extracted
D
E
1 µm
E
F
0.25 µm
G
F
G

CHAPTER 4

ANCILLARY FINDINGS FROM THE COREM STUDIES

4.1 Introduction

The primary focus of our structural-kinetic analyses in chick DRG neurons presented in Chapters 2 and 3 was the correlation of actin ultrastructure with veil protrusion and retraction. However, while evaluating the correlative microscopy, other novel structural and behavioral findings were observed. In some cases, preliminary studies were performed to further evaluate these findings. Although these findings fell outside the scope of the published work, they nonetheless provide a foundation to guide future studies.

4.2 Filopodia fusion.

Filopodia fusion events were frequently observed in the phase contrast image sequences, occurring between filopodia of the same growth cone as well as with adjacent growth cones. Filopodia were observed to fuse together from all locations along the shaft: upward from the base, through contact along the length of the shaft, at the tips, and downward from the tips towards the growth cone. Some of these fusion events were captured in the correlative microscopy experiments. At the EM level, the fused regions of filopodia shafts often appeared as a single filopodium.

The image sequence in Figure 32B shows two filopodia (red arrows) that were separated by a short length veil at the start of the image sequence. As the veil advanced between the filopodia, the filopodia were brought closer together, and by the third frame of the time-lapse, they shared a common base. In the subsequent frames,

Figure 32 "Zippering" from the base of two of filopodia.

A. The last live image of the growth cone before extraction. White box denotes the region of interest. **B.** Time-lapse image sequence of region of interest. Red arrows identify the filopodia of interest. They begin separately, and then slowly migrate towards one another to share a common base, and finally become fused from the base upwards. **C.** Low magnification platinum replica electron micrograph (EM) of the region of interest. **D.** High magnification of the fused filopodia. Longer white arrows show the fused based. The individual filopodia cannot be discerned. The tips, however, have not fused yet (short white arrow)

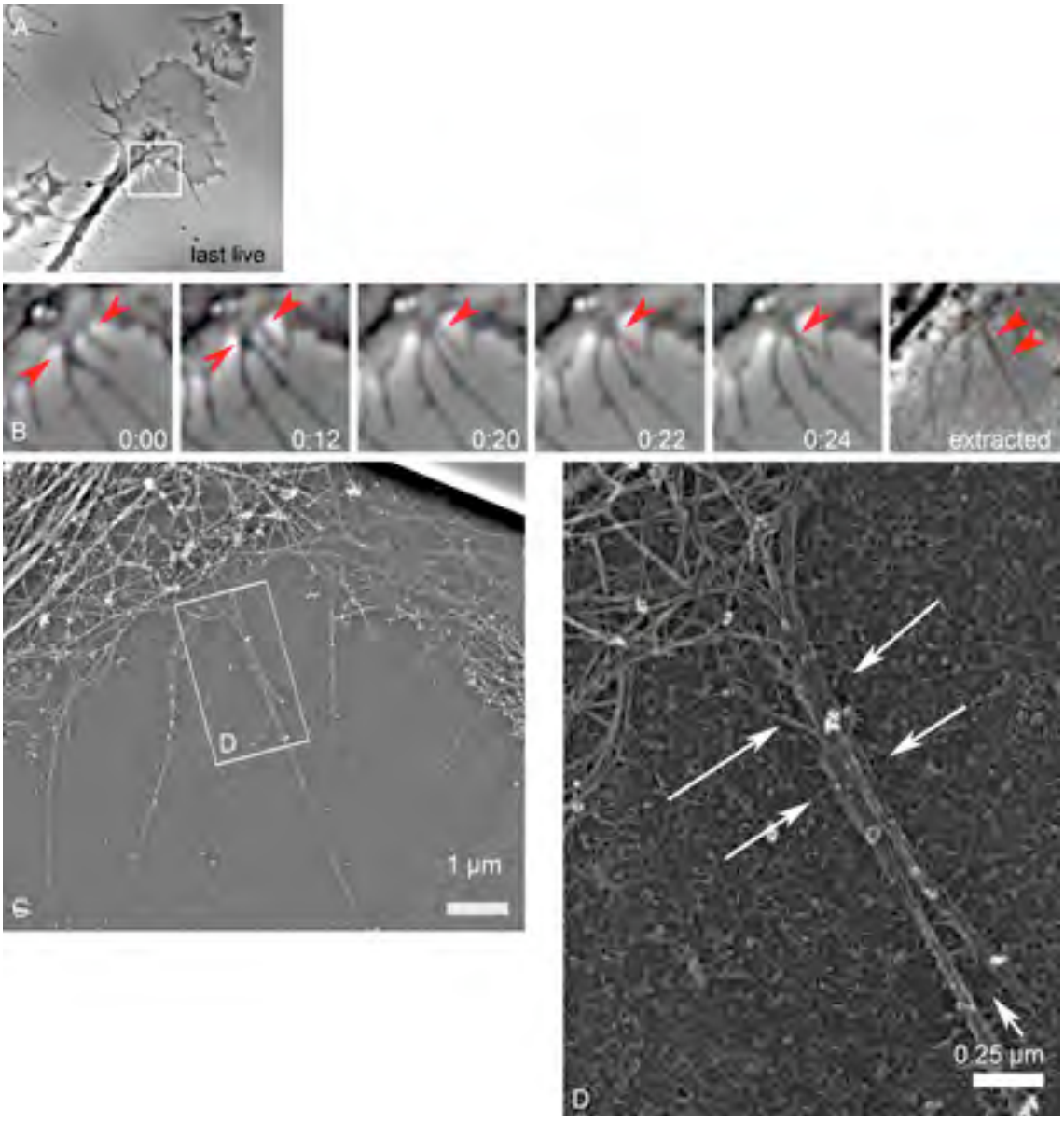
A
last live
B
0:00
0:12
0:20
0:22
0:24
extracted
C
D
1 µm
D
0.25 µm

the shafts of the filopodia “zipper” together towards the tips. In the EM (Figure 32C, D), the bases of the two filopodia appear completely merged into a single filopodium shaft (white arrows). Moving up from the base, the filopodia remain bound together for approximately 0.75 μm before the individual shafts can be visualized near the tip of the shorter filopodium on the right. A few short filaments are seen bridging the gap between the two filopodia where they become separated.

In Figure 33B a veil protrudes (red arrow) between two filopodia, as the veils to the right and left of the filopodia retract (black arrow). As the image sequence progresses, the veil advances forward between the filopodia while the shafts of the two filopodia become fused into a single shaft behind the veil. This results in the creation a Y-shaped junction seen at the base of the veil in the EM (Figure 33C, D). A single filopodium shaft is observed behind the veil, and it is studded with short actin filament clusters that may represent remnants of the veil. One cluster was large enough to form a phase dense spot (*) that was visible in the last frame of the image sequence before extraction.

In Figure 34, the tip of one filopodium (white arrow) is brought into contact with the shaft of a second filopodium as a veil (red arrow) protrudes between them. The two filopodia contact each other during the last 3 seconds of the image sequence as the veil approached the tip of the lower filopodium, and they appear fused together after extraction (Figure 34B, “extracted”). In the EM (Figure 34C, D), a single smooth shaft is observed where the filopodia merged, and the tip of the filopodia that contacted the shaft cannot be distinguished.

Figure 33 Filopodia fusion occurring behind veil protrusion.

A. The last live image of the growth cone before extraction. White box denotes the region of interest. B. Time-lapse image sequence of region of interest. Black arrow denotes body of growth cone retracting away from filopodia. Red arrow marks small veil C. Low magnification platinum replica electron micrograph (EM) of the region of interest. D. High magnification of proximal shaft of filopodium that was created by fusion of two separate filopodia after the veil protruded between as shown in the time-lapse. (*) marks star-like actin structures that appeared as phase dense spots along the filopodium shaft in the last live frame.

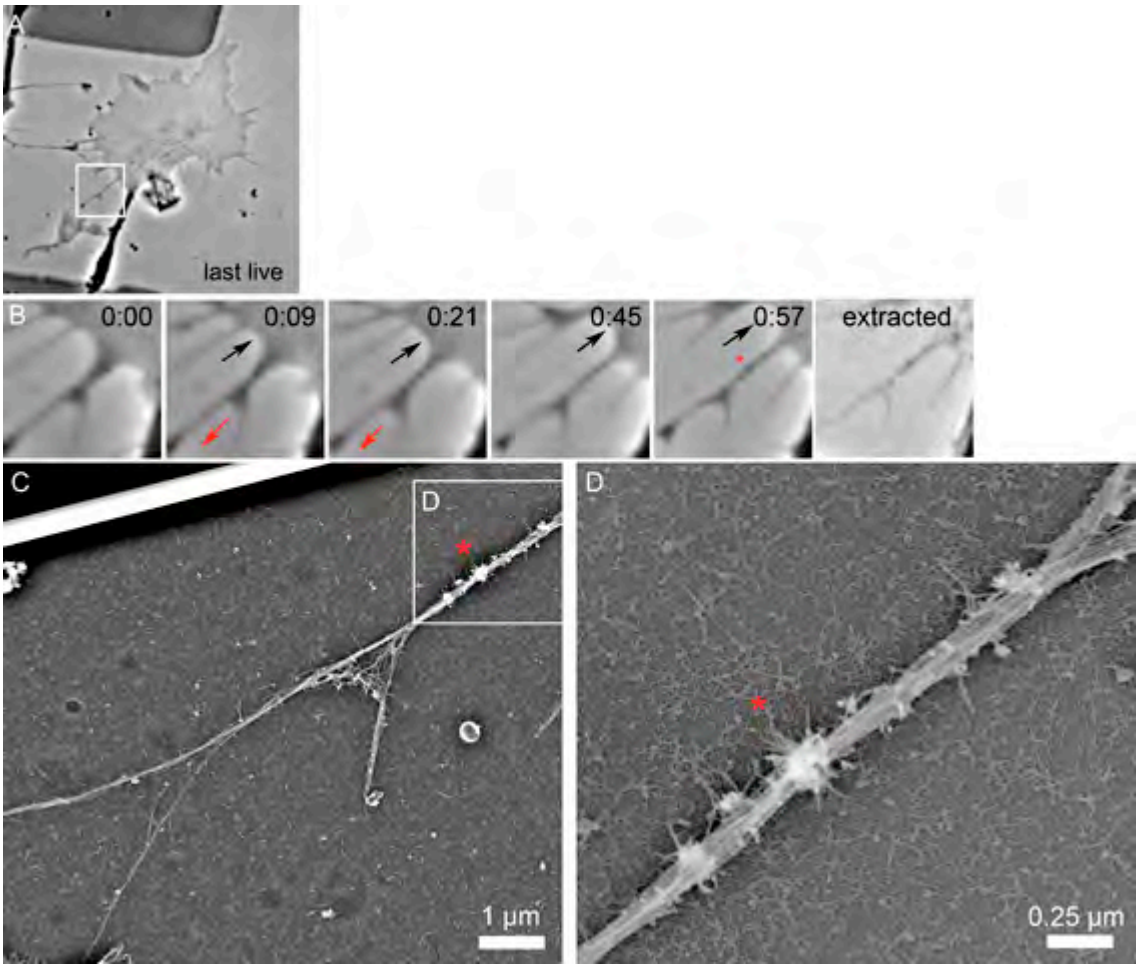
A
last live
B
0:00
0:09
0:21
0:45
0:57
extracted
C
D
1 µm
D
0.25 µm

Figure 34 Fusion of filopodia tips following veil protrusion.

A. The last live image of the growth cone before extraction. White box denotes the region of interest. **B.** Time-lapse image sequence of region of interest. Red arrows mark the protruding veil of interest. White arrowhead identifies the lower filopodium protruding towards the upper filopodium as the veil protrudes along it. **C.** Overlay showing the amount of veil protrusion (appears red) over the last 6 seconds before extraction. **D.** Low magnification platinum replica electron micrograph (EM) of the region of interest. **E.** High magnification of convex filopodia delimited veil marked in D. The filopodia tip meet during the last 3 seconds and fuse together by the time extraction has occurred. In this case, the fusion occurs as the veil protruding up between the filopodia reaches the lowest point of fusion. **F.** Tips of fused filopodia showing a single shaft that is smooth. The tip of the lower filopodium is not visible.

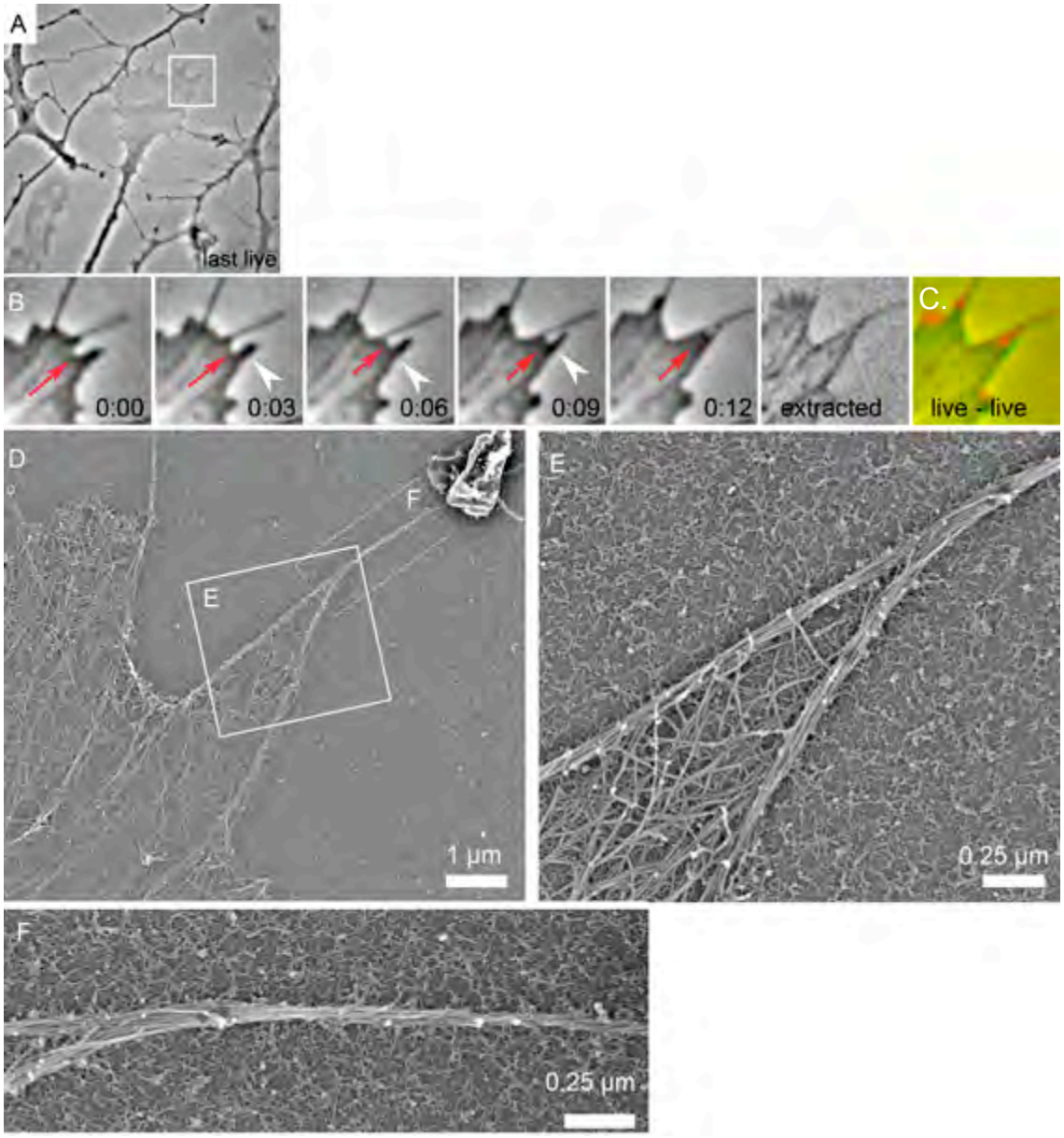
A
last live
B
0:00
0:03
0:06
0:09
0:12
extracted
C.
live - live
D
F
E
1 µm
E
0.25 µm
F
0.25 µm

Figure 35B shows two filopodia that came into contact with one another and fused together near their tips, prior to the start of veil protrusion along their shafts. Extraction occurred before the veil reached the point of fusion. In the EM (Figure 35C, D) the base of the fused region appears as a single filopodium, while the tip of the right filopodium can be clearly identified and appears to separate from the fused shaft. Arp3 immungold spots are seen dotting the base of the fused shafts.

In Figure 36B, two filopodia shafts cross one another during the last 6 seconds of the image sequence, and a phase dense spot appears in the last live frame before extraction. In the EM (Figure 36C, D) a few short actin filaments are visible just beneath the point of intersection (red arrow).

The ability of filopodia to contact one another and fuse together has not been previously evaluated. Fusion appears to promote the creation of novel filopodial structures – such as branches and Y junctions, which diverge from the straight filopodial organization traditionally reported in fibroblasts. Arp3 immunogold spots were frequently observed along the shafts of fused filopodia in our CorEM studies. These clusters may correspond to the Arp3 speckles that we observed moving along filopodia shafts during TIRF microscopy of PC-12 growth cones expressing GFP-Arp3. The short filaments seen between fused and newly fusing filopodia could suggest a potential mechanism by which de novo veil initiation may occur along filopodial shafts. Together, these fusion events suggest that neuronal filopodia are capable of complex filopodia-filopodia and veil-filopodia interactions.

Figure 35 Fusion of filopodia tips.

A. The last live image of the growth cone before extraction. White box denotes the region of interest. B. Time-lapse image sequence of region of interest. C. Overlays showing the amount of veil protrusion (appears red) over the last 6 seconds before extraction (upper overlay) and from the last live frame until extraction (lower overlay). D. Low magnification platinum replica electron micrograph (EM) of the region of interest. E. High magnification of convex filopodia delimited veil marked in D. In this case, the tip of the right filopodium merges with the shaft of the left filopodium before the veil began to protrude along the two shafts.

B.

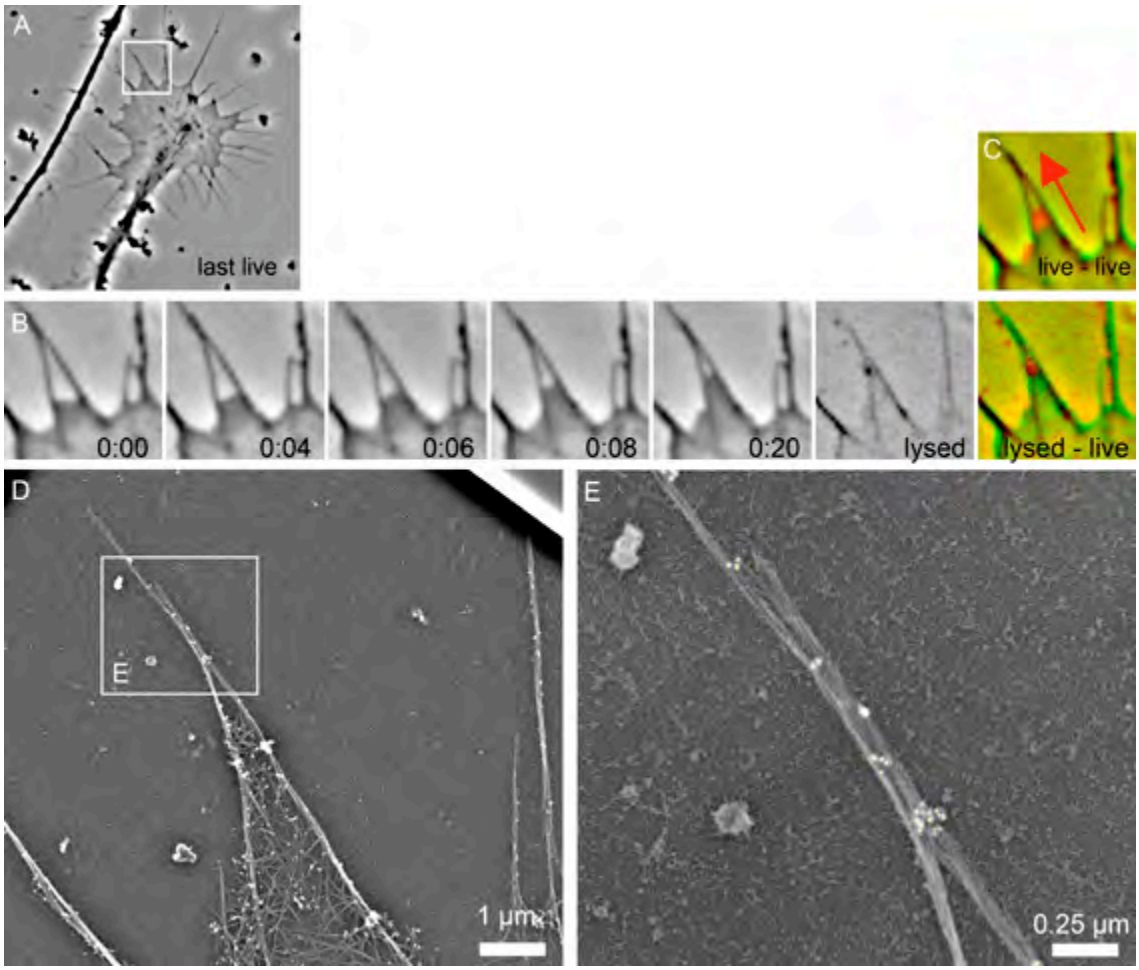
A
last live
C
live - live
B
0:00
0:04
0:06
0:08
0:20
lysed
lysed - live
D
E
1 µm
E
0.25 µm

Figure 36 Filopodia ultrastructure shortly after contact.

A. The last live image of the growth cone before extraction. White box denotes the region of interest. **B.** Time-lapse image sequence of region of interest. **C.** Low magnification platinum replica electron micrograph (EM) of the region of interest. **D.** High magnification of recent filopodia crossing. The region becomes slightly phase dense in the time-lapse, and in the EM, small filaments are seen selectively coming off the filopodia into the region beneath the intersection of the two shafts (red arrow).

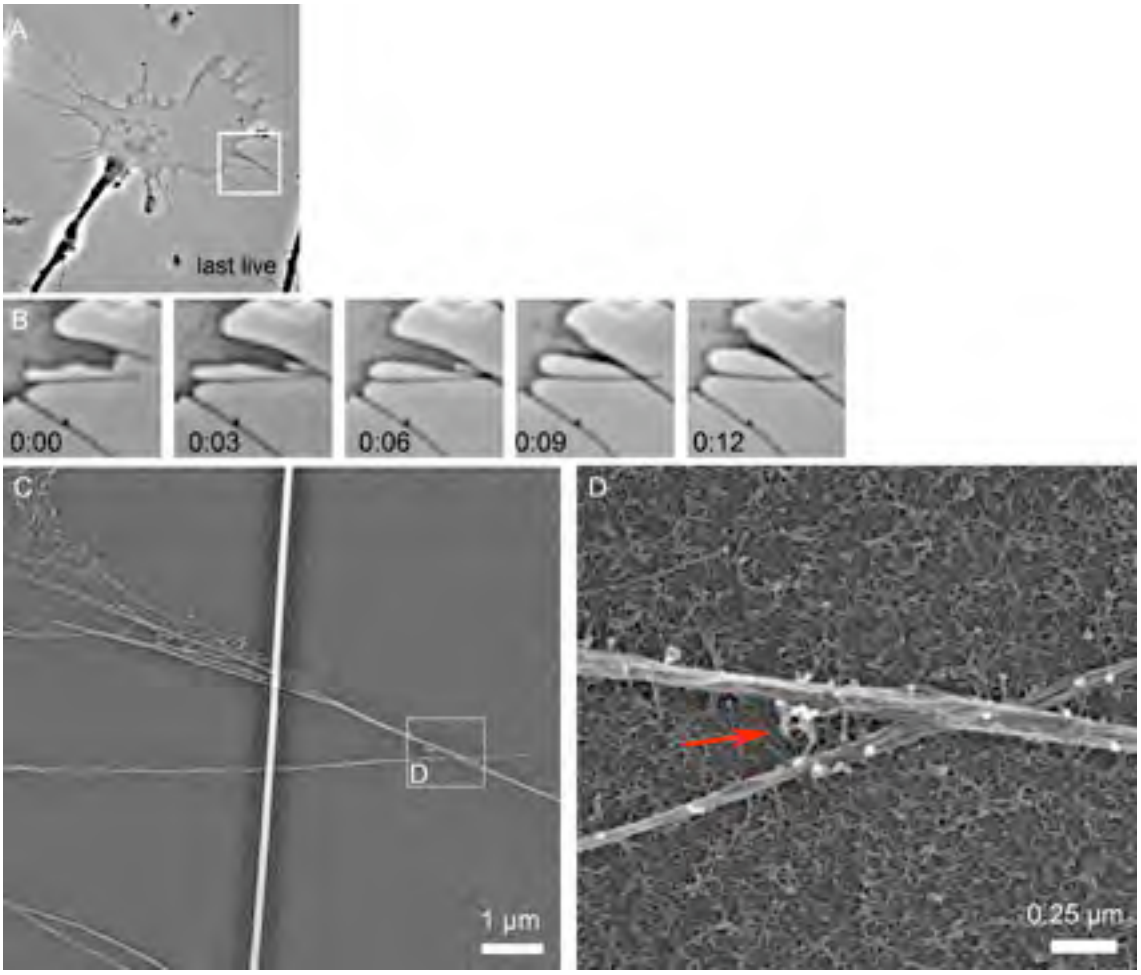
A
last live
B
0:00
0:03
0:06
0:09
0:12
C
D
1 µm
D
0.25 µm

4.3 Filopodia tip structures vary with protrusion or withdrawal state.

In Chapter 2 we showed that the actin cytoskeleton in neuronal veils had dramatically different ultrastructural organization depending on whether the veils were protruding or retracting. Here we evaluated whether filopodial ultrastructure also changed with protrusion and retraction by examining the ultrastructure of filopodia that were either actively protruding, retracting, or stalled as determined by merging the last live and extracted frames from the image sequence (Figure 37). In addition to protrusion and retraction, neuronal filopodia have also been described as having a "life cycle," whereby they arise at the leading edge of the growth cone, sweep backwards, and eventually become deposited into the actin-rich membrane-associated with the axonal shaft (Bray and Chapman, 1985). We also evaluated filopodia along the axonal shaft see if significant changes in ultrastructure had occurred after incorporation into the axonal shaft.

We first examined the tips of the filopodia to evaluate whether any ultrastructural differences were present in different states of motility. We noted that the majority of protruding filopodia (13/17) terminated in a globular appearing head, similar in appearance to the structure described by Lewis in chick DRGs and to the "tip complex" reported by Svitkina et al. in melanoma cells (Lewis and Bridgman, 1992; Svitkina et al., 2003) (Figure 37A, B (1)). None of the 8 retracting filopodia in this study contained a tip complex at the distal end (Figure 37(3)). Stalled filopodia, that neither protruded nor retracted during the last few seconds of imaging, predominantly lacked a tip complex

(1/12) (Figure 37(2)). Filopodia located along the axon also lacked a tip complex (0/15) (Figure 37(4)).

We also evaluated the number of “hairs” along the shaft of the filopodium (Figure 37B). Hairs were defined as any actin filament protruding from the filopodium shaft, oriented at an angle greater than 50˚ from the angle of the filopodium shaft. Filopodia were considered “hairy” if they contained greater the 10 hairs along their length. 35% of protruding filopodia, 55% of stalled, and 38% of retracting filopodia were hairy, while 80% of axonal filopodia were hairy. We qualitatively noted that filopodia along the axonal shaft appeared to have a greater number of hairs, containing longer filaments than those seen in the growth cone itself. Additionally, these filopodia stained heavily with Arp3 immunogold.

Svitkina et al showed that the tip complex appeared very early in filopodia formation, and physically linked the barbed ends of actin filaments in the filopodium together, preventing splaying of actin filaments in the filopodium (Svitkina et al., 2003). In this preliminary report, we observed that this globular tip structure was primarily found in protruding filopodia, to the general exclusion of retracting, stalled, and axonal filopodia. The relationship between tip structure loss and filopodia retraction is not known. We also observed that filopodia along the axonal shaft appeared more “hairy” than those within the growth cone, suggesting that changes to neuronal filopodial ultrastructure may occur as they become embedded in the axonal shaft.

Figure 37 Protruding Growth Cone Filopodia and Microspikes have Intact Tip Complex

A. (upper panel) Merges of the last live and extracted frames, red = protrusion, cyan = retraction. (lower panel) EM of protruding (1), retracting (3), stalled (2), and axonal filopodia (4). **B**. Table summarizing presence or absence of the tip complex and branching. Tip complex was considered present or absent by visual inspection of 20,000X images. Hairs were defined as any actin filament protruding from the filopodium shaft, oriented at an angle greater than 50˚ from the angle of the filopodium shaft. Filopodia were considered hairy if they contained greater the 10 branches along their length

A.

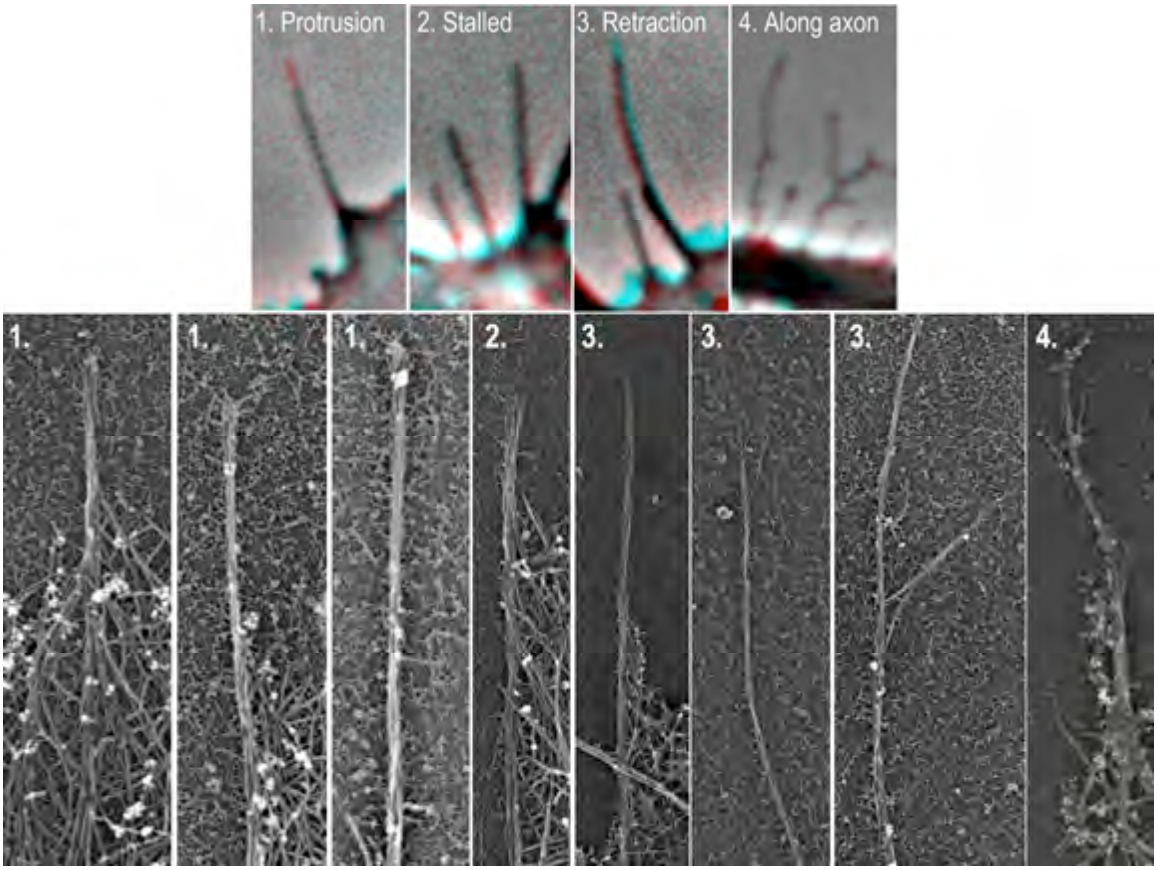

B.

	protruding filopodia				stalled filopodia				retracting filopodia				filopodia along shaft			
	tip structure	no tip structure	hairy	not hairy	tip structure	no tip structure	hairy	not hairy	tip structure	no tip structure	hairy	not hairy	tip structure	no tip structure	hairy	not hairy
sum	13	4	6	11	1	11	6	5	0	8	3	5	0	15	12	3
%	0.76		0.35		0.08		0.55		0.00		0.38		0.00		0.80	

.

4.4 Myosin IIA Immunostaining.

In Chapter 2 we presented a first report of veil retraction. In sharp contrast to veil protrusion, retraction was not associated with a dendritic network. Rather, the leading edge was replaced by bundled actin filaments that were oriented parallel to the membrane. These parallel actin bundles at the membrane edge of retracting veils resembled similar bundles generated by myosin II in keratocytes, at the rear of the lamellum (Svitkina et al., 1997; Verkhovsky et al., 1995). Of the three known myosin II isoforms, myosin IIA and B isoforms have been localized to (Rochlin et al., 1995), and have been shown to form bipolar filaments in, growth cones (Bridgman, 2002). In these studies, both isoforms stained most intensely in the central region of the growth cone, colocalizing with F-actin bundles, and out towards the transitional and peripheral domains along embedded roots of some filopodia. Other studies indicated that myosin IIA was implicated in growth cone retraction (Wylie and Chantler, 2001; Wylie and Chantler, 2003; Wylie et al., 1998). None of these studies addressed the role of myosin IIA in individual veil motility. The implication of myosin IIA in growth cone retraction and the similarity of the ultrastructure of edge bundles raised the possibility that myosin IIA might have a potential role in veil retraction. This prompted us to examine myosin IIA localization in chick DRGs.

Myosin IIA immuno-localizes to phalloidin poor regions of the growth cone.

In chick DRG growth cones, myosin IIA staining was brightest in regions of low actin density as evaluated by phalloidin staining (Figure 38 A-C). Punctate, linear myosin IIA

staining was seen throughout the central region of the growth cone. The myosin IIA staining was particularly intense along the membrane edge at the rear of the growth cone and at the front of the growth cone in regions of low phalloidin staining (white arrows). Additionally, staining was observed along the shafts of filopodia at the rear of the growth cone and along the axon. However myosin IIA staining was faint or absent in regions of bright phalloidin staining (red arrows). Neuronal fibroblasts growing with the DRGs (Figure 38D) lack myosin IIA staining in the lamellipodia, with the bulk of the staining restricted to the cell body. In our experience with DRGs regions of low phalloidin staining and a concave edge correlated with veil retraction (Figure 9), while regions with bright phalloidin staining correlated to a high actin density and veil protrusion. Control staining with secondary antibody or rabbit non-immune serum and secondary antibody was negative. These results were repeated on 3 separate occasions, and led us evaluate the feasibility of immuno-electron labeling with myosin IIA. Figure 39 shows a non-correlative growth cone labeled with myosin IIA. Insets mark two regions with a concave leading edge containing parallel bundled actin filaments, similar to those seen in retracting veils. Gold staining is seen along these bundled filaments. Figure 40 shows a non-correlative growth cone with a dendritic network similar to those seen in protruding veils. Very little myosin IIA labeling is seen in the network.

The staining pattern observed for myosin IIA at both the light and EM level suggest that it is enriched in actin poor regions that appear similar to retracting veils,

and may indicate a role for myosin II in individual veil retraction. CorEM studies with immuno-electron labeling for myosin IIA are needed to further evaluate these results.

Figure 38 Myosin IIA Immunostaining in the Growth Cone.

Immuno-fluorescent staining against myosin IIA in chicken dorsal root ganglion neurons (top two rows), and non-neuronal glial cell (lower row) ~ 24 hours after plating. For all cells, phalloidin (red) and myosin IIA (green) immunostaining are shown individually and merged. In all cells, myosin IIA staining was brightest in regions of low actin density (white arrows) by phalloidin staining. The staining was especially bright along the rear edge of the growth cone, and along filopodia at the rear end of the growth cone and along the shaft. Myosin IIA staining was almost entirely excluded from regions of bright phalloidin staining (red arrows).

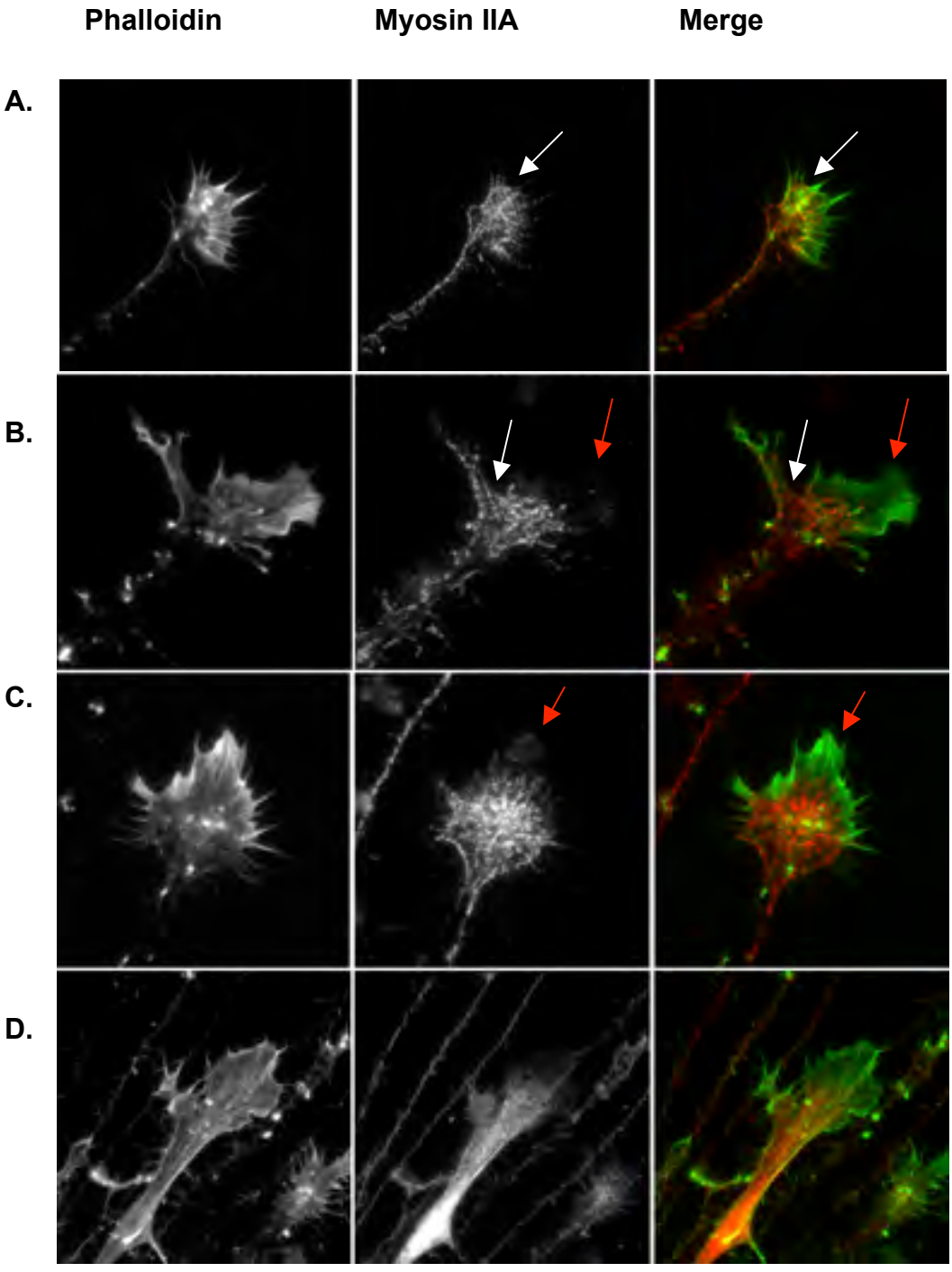
Phalloidin
Myosin IIA
Merge
A.
B.
C.
D.

Figure 39 Myosin IIA Immuno-electron staining in bundled edge filaments.

A. Low magnification image of growth cone, boxes mark location higher magnification insets in B and C. B and C. High magnification of boxed regions in A. Myosin IIA is seen labeling bundled filaments at the membrane edge. Gold particles have been pseudocolored yellow for easier visualization.

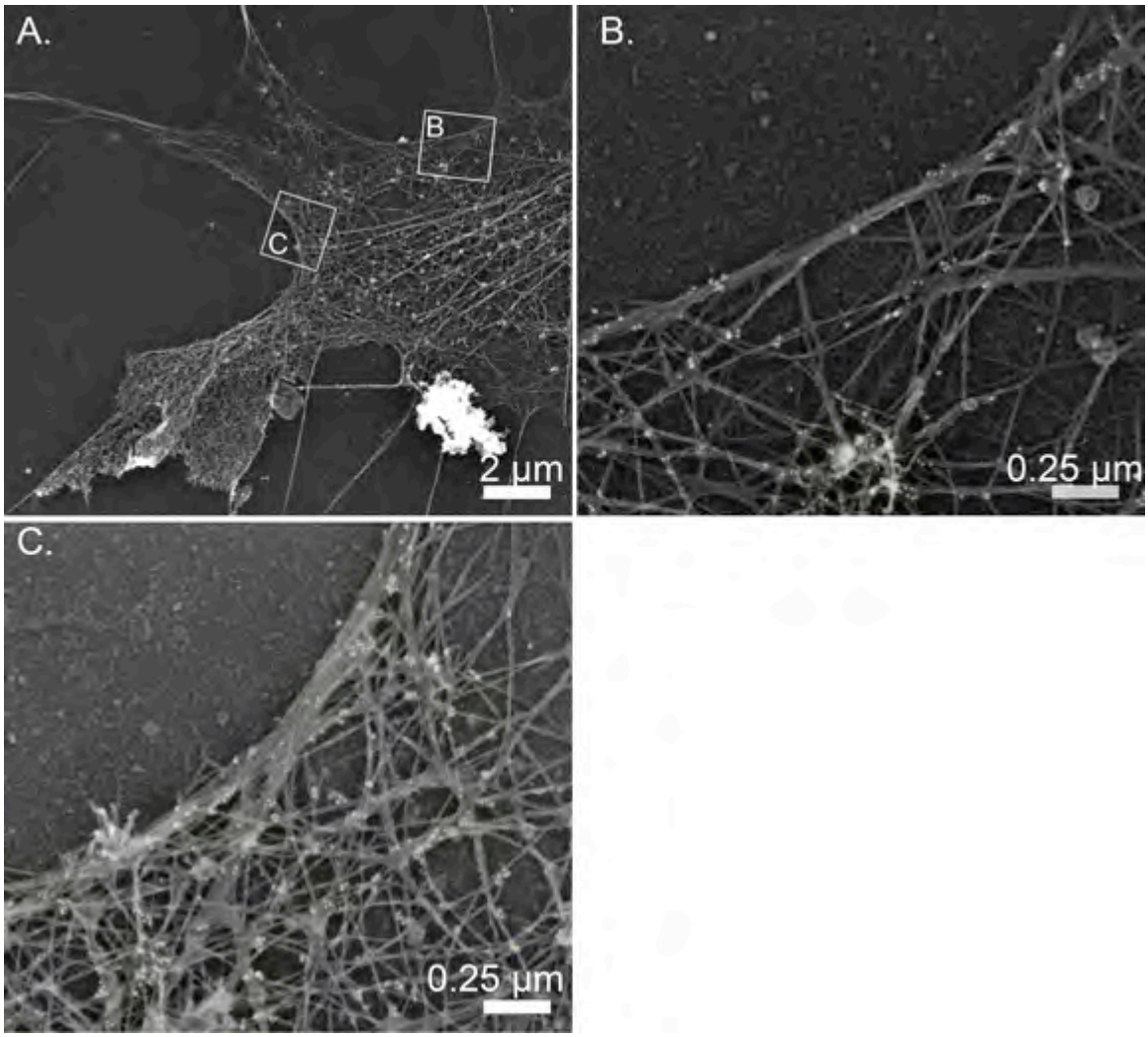
A.
B
C
2 µm
B.
0.25 µm
C.
0.25 µm

Figure 40 Myosin IIA Immuno-electron staining in a dendritic network.

A. Low magnification image of growth cone, box marks the location of higher magnification inset in B. B. High magnification of boxed region in A. Myosin IIA immunogold labeling appears largely excluded from the dendritic network. Gold particles have been pseudocolored yellow for easier visualization.

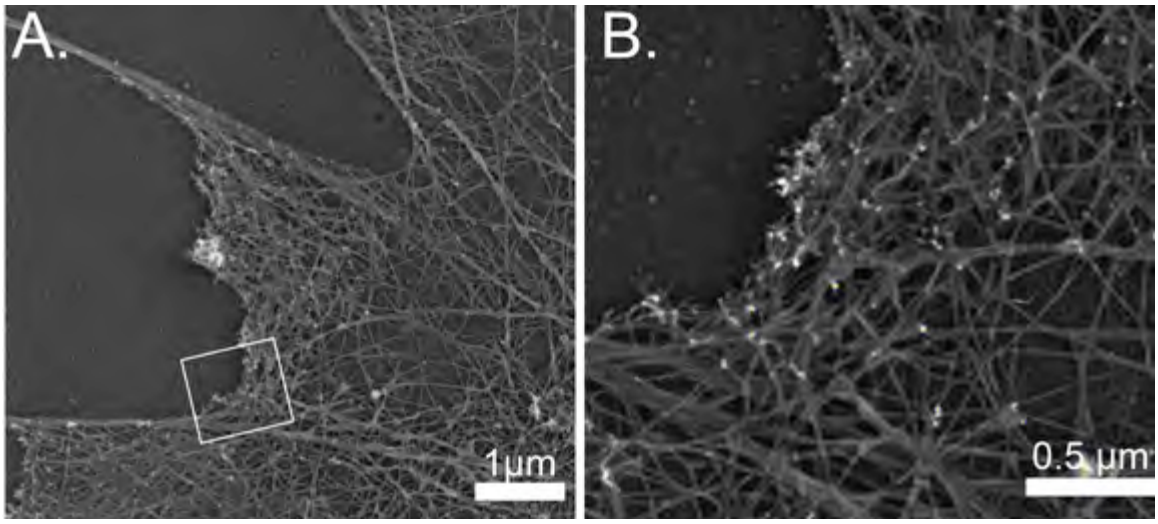
A.
1µm
B.
0.5 µm

4.5 Phosphotyrosine Immunostaining.

Phosphotyrosine staining, while non-specific to individual protein, is sensitive for localizing phosphorylated tyrosines found in many proteins involved in adhesion (Wu and Goldberg, 1993). It has been studied in growth cones and growth cone filopodia by other labs investigating ß1-integrin, vinculin, and veil advance (Wu et al., 1996). Phosphotyrosine immunostaining in melanoma cells in the laboratory showed exclusion of staining from the shafts of filopodia (Schober et al., 2007). As this was in conflict with published literature in growth cone filopodia (Steketee and Tosney, 2002), we repeated the staining in DRGs for comparison. Our initial triple staining of growth cones with anti-phosphotyrosine, tubulin, and phalloidin (Figure 41) showed primarily punctate staining along the entire length of growth cone filopodia. In many cases the staining extended to filopodia tips. In others, it was absent from the tip. We did observe staining along the shafts of filopodia associated with veils, which is in contrast with reports by Steketee that showed exclusion of staining in filopodia associated with veils (Steketee and Tosney, 2002). The difference in filopodia staining between B16F1 and neuronal filopodia suggests that DRG filopodia may contain adhesion proteins not found in melanoma filopodia, and should be evaluated further.

Figure 41 Anti-Phosphotyrosine Staining in the Growth Cone

Immuno-fluorescent staining using antibodies against phosphotyrosine and tubulin in chicken dorsal root ganglion neurons ~ 24 hours after plating. Anti-phosphotyrosine (blue), phalloidin (green), and tubulin (red) are shown in the merge. Insets show punctate phosphotyrosine staining along filopodia shafts and at the tips of some filopodia. Arrowhead points to smooth veil that stains heavily with phalloidin, but has no phosphotyrosine staining.

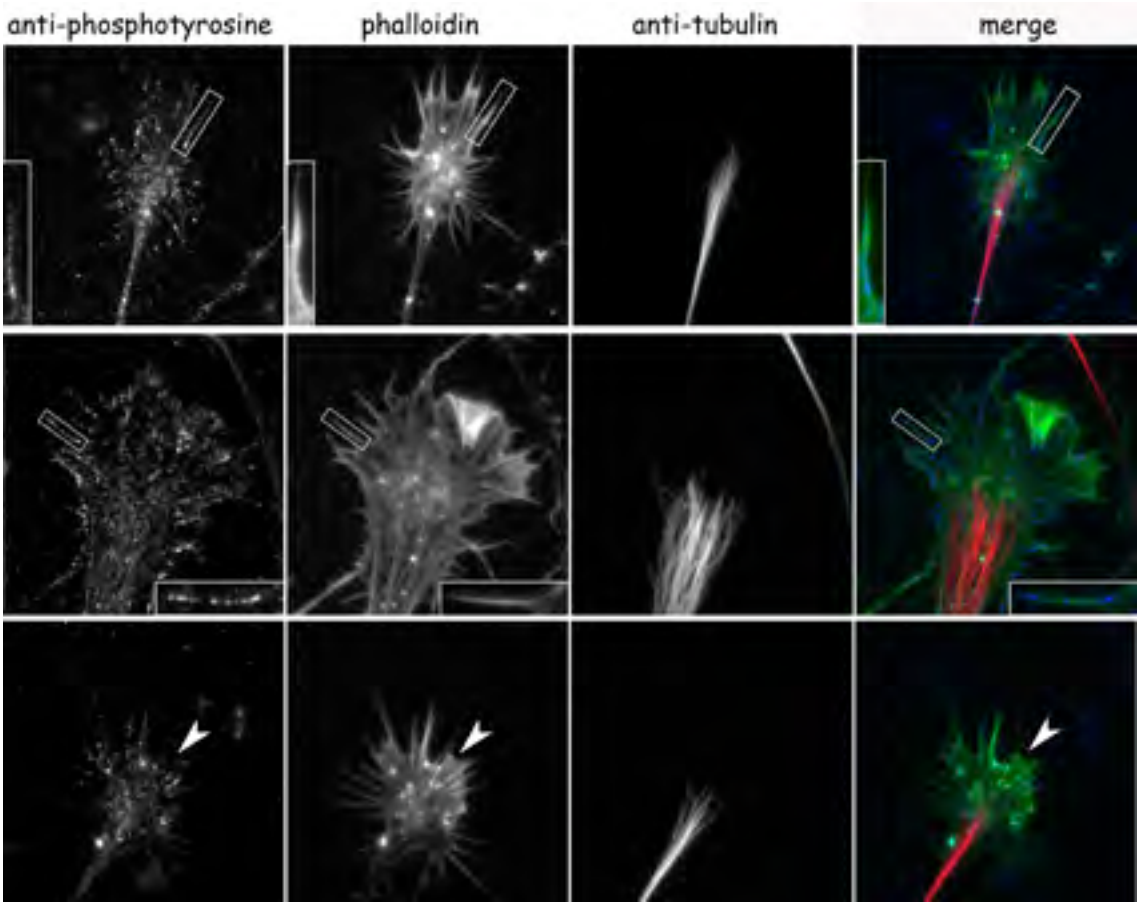
anti-phosphotyrosine
phalloidin
anti-tubulin
merge

4.6 Correlative Rhodamine-actin Incorporation

In the array treadmilling model, uncapped barbed ends are normally restricted to the extreme leading edge of lamellipodium (Mejillano et al., 2004), where the addition of actin subunits results in membrane advance (Pollard and Borisy, 2003). The distribution of barbed ends in neuronal veils was not previously evaluated. The novel veil-filopodia interactions we observed, suggested that growth cone veils might possess a different distribution of barbed ends.

The location of free barbed ends in a given specimen can be evaluated by extraction of the membrane followed by incubation with rhodamine-derivatized actin. Alexa-488 phalloidin is then added to stain the unlabeled actin from the pre-existing network. Rhodamine actin incorporation was seen at the periphery of the growth cone (Figure 42D, E) and in the central region of the growth cone, associated with pre-existing actin puncta. Rhodamine actin incorporation was highest in regions that had been protruding in the seconds before extraction (Figure 42 B, E, and boxed regions 1, 2). Incorporation was low or absent in regions that had been retracting at the time of extraction (Figure 42B, E, and boxed region 3). Spots of rhodamine phalloidin were observed at the ends of filopodia as expected (Figure 42 E, boxed region 2). Additionally, rhodamine actin incorporation was seen along the length of filopodia associated with protruding veils (Figure 42E, boxed region 1, filopodia in the center).

The EM (Figure 42 E, F) shows a veil that had begun to protrude from the crotch of two filopodia roots during the last live frame (Figure 42B, boxed region 1). Bright

Figure 42 Correlative Rhodamine Actin Incorporation

Chick DRG, 24 hours after plating. A live imaging sequence was obtained, the cell was extracted and incubated with rhodamine derivatized actin and ATP on the microscope stage. (A, B) Merge of last two live frames, and last live and lysed frames, respectively. Red indicate protrusion, Cyan indicates retraction. (C, D, E.) Alexa 488 phalloidin stains the endogenous actin (C), but not the rhodamine actin incorporated at the barbed ends (D). The merge (E) shows the rhodamine actin in green, and the phalloidin in red for easier visualization. The boxed regions numbered 1-3 (also marked in B) and contain: (1) A new veil that had begun protruding from the crotch of two filopodia in the last live frame and shows bright rhodamine actin incorporation. This veil is shown in the high magnification EM. Rhodamine actin speckles co-localize with the shaft of the filopodium in the center. (2) A protruding veil with filopodia, rhodamine actin incorporation is seen at the tips of the filopodia. (3) Decreased rhodamine actin was seen in a region of veil retraction (F) low magnification EM of the same cell. Boxed region shown in (G) corresponds to the same veil shown in (1). A dendritic network is seen arising off of filaments in the roots of two filopodial shafts.

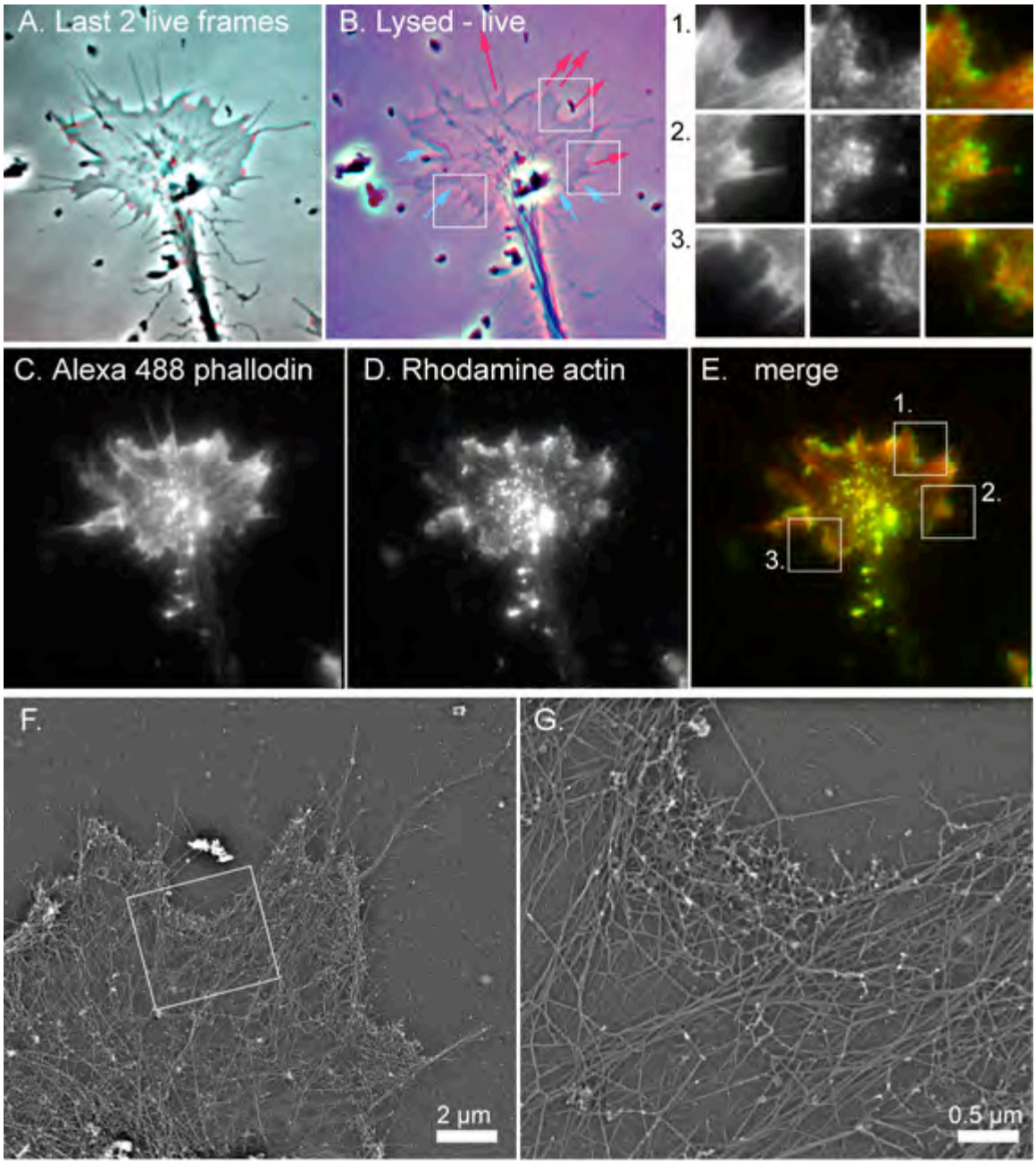
A. Last 2 live frames
B. Lysed - live
1.
2.
3.
C. Alexa 488 phallodin
D. Rhodamine actin
E. merge
1.
2.
3.
F.
2 µm
G.
0.5 µm

rhodamine actin incorporation was seen in the veil as well as along the shaft of the upper filopodia, but was excluded from the surrounding region. At high magnification (Figure 42), a dendritic network was observed arising from actin filaments in the roots of the two filopodia. The region surrounding the veil was very sparse.

These results suggest that free barbed ends in neuronal growth cones are concentrated at leading edge of actively protruding veils and filopodia tips, and sparse in regions of retraction. The appearance of demarcated rhodamine incorporation in newly initiated veils suggests that barbed ends can be rapidly generated from bundled filopodia roots to support veil initiation in previously quiescent or retracting regions.

4.7 EM with glutaraldehyde fixation in place of membrane extraction.

Membrane dynamics observed during phase contrast imaging could not be preserved during extraction. The filopodia fusion events captured in the CorEM studies described above, showed apparent fusion of filopodial shafts that had been brought into contact with one another. The use of CorEM with glutaraldehyde fixation in place of membrane extraction allowed us to evaluate the morphology of membrane-covered filopodia with a known protrusive history. In the CorEM, five of seven protruding filopodia appear to have a bulbous expansion at the tip (**Figure 43** A, B). A bulbous tip was defined as a tip having a diameter 2X greater than the diameter of the shaft at the widest point, with the widest point located no further than the diameter from the tip. Two of nine retracting veils had a bulbous tip, with the remainder of tips being of equal or less width to the shaft or cone-shaped with a narrow tapered tip (**Figure 43**C, D).

Figure 44 shows four non-correlative examples of connection events captured in other growth cones observed during the glutaraldehyde fixation experiment. In Figure 44A, two filopodia connect from the tips along the shaft. Small gaps exist between the shafts. In Figure 44B, the tip of one filopodium contacts the shaft of another. Figure 44C shows a circular hole in the membrane formed by two veils that contact one another. Similar holes were observed in the image sequences taken for the CorEM experiments. These holes were observed to seal themselves off. Figure 44D shows a connection between two filopodia from different neurons that are oriented in opposite directions.

4.8 Summary.

In the preliminary findings presented above, we showed a diverse group of observations taken from our CorEM and related follow-up studies. The observations pertaining to filopodia showed that neuronal filopodia posses the ability to fuse together. These fusions lead to the creation of novel branched filopodial structures. Additionally, we noted that the majority of protruding filopodia contained a globular structure on their tips, which was absent in most retracting, stalled, and axonal shaft filopodia. Future studies will be needed to better evaluate the significance of filopodial dynamics and tip structure.

The staining of edge bundles and actin poor veils with myosin II suggests that it may have a role in veil retraction. The incorporation of rhodamine actin into veils arising from filopodial roots suggests that growth cones can selectively generate barbed ends,

allowing the formation of new dendritic networks from bundled precursors. Future studies should evaluate the dynamic interplay between edge bundling and branching as of neuronal veils cycle between protrusion and retraction.

Figure 43 CorEM of membrane bound filopodia tips.

A, B. Protruding filopodia have a rounded, bulbous tip. C, D. Retracting filopodia have a narrower, pointed or flat tip.

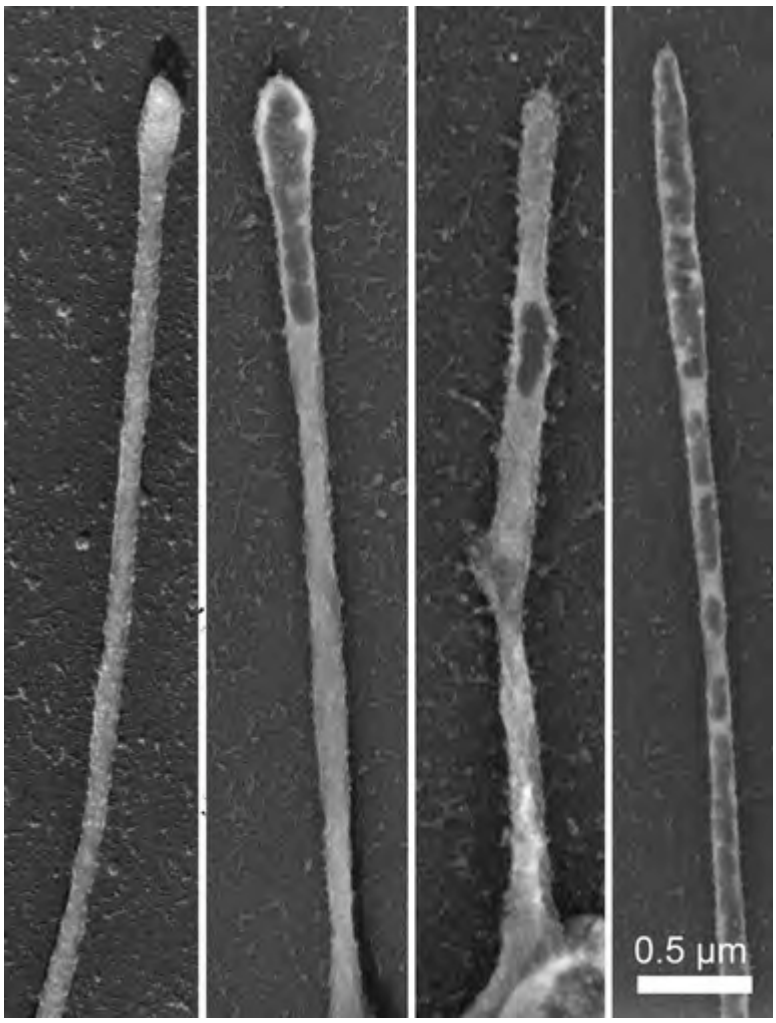
0.5 µm

Figure 44 EM of membrane bound filopodia and veil connection events.

A. Two filopodia connect from the tips along the shaft. B. The tip of one filopodium contacting the shaft of another. C. Creation of a circular hole where two veils contact one another. D. Connection between two filopodia from different neurons oriented in opposite directions.

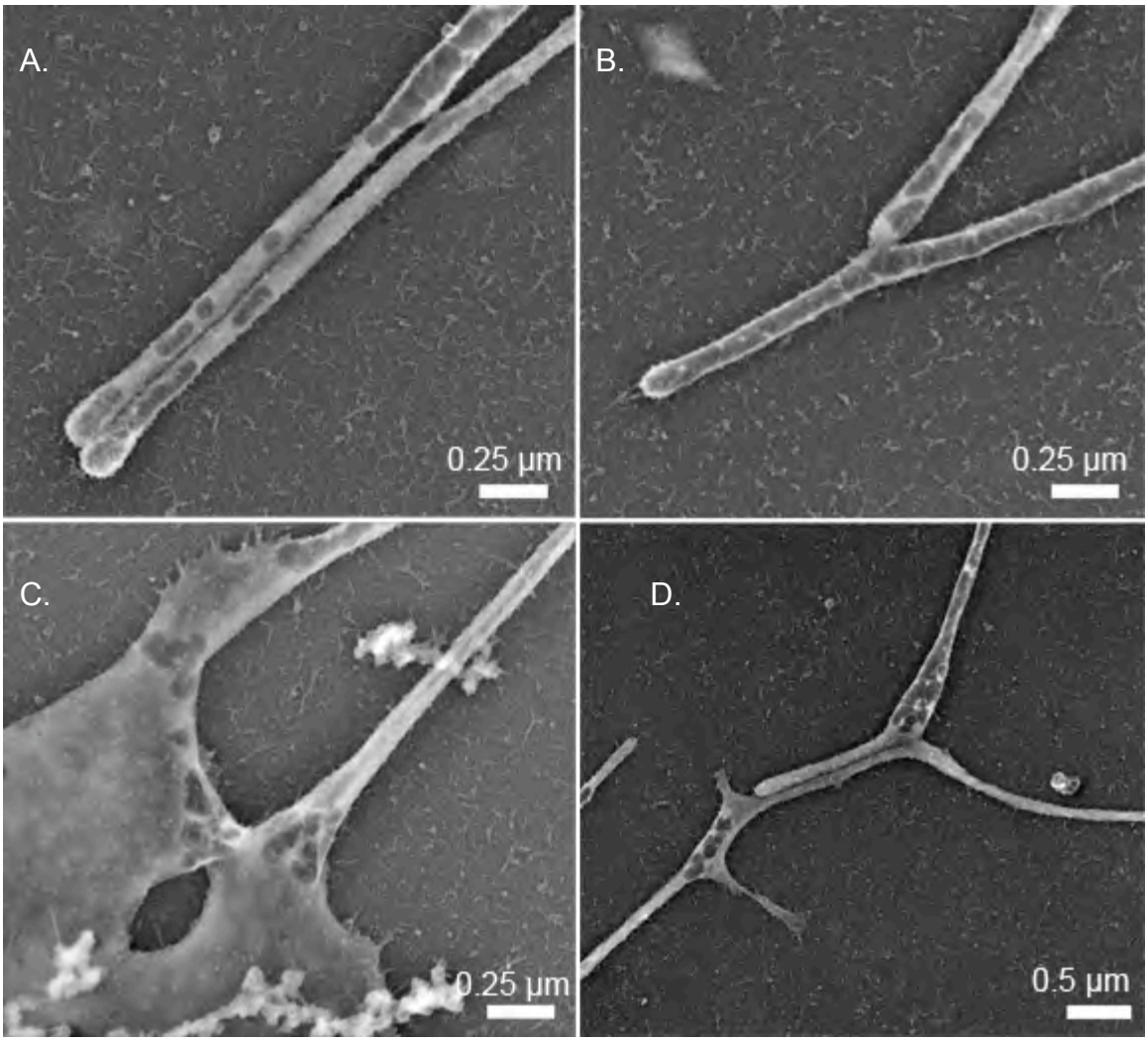
A.
0.25 µm
B.
0.25 µm
C.
0.25 µm
D.
0.5 µm

CHAPTER 5

ARP2/3 COMPLEX KNOCKDOWN STUDIES

5.1 General Introduction:

Motile cells use the actin cytoskeleton to power their movement. This cytoskeleton can be organized into different forms to suit different motility needs based upon environmental cues, complex signaling cascades, and/or the levels of various proteins that modify the organization of actin with the cytoskeleton. The two major actin based protrusive organelles are the filopodia and lamellipodia. Filopodia are spike-like structures that contain tightly bundled actin filaments, which arise by reorganization of filaments from a dendritic network (Svitkina et al., 2003). The lamellipodia is a sheet like structure filled with an orthogonal actin array which treadmills, adding subunits at the barbed ends of filaments at the leading edge while depolymerizing from pointed ends at the rear (Svitkina and Borisy, 1999).

Arp2/3 is a seven subunit complex purified from *Acanthamoeba* (Machesky et al., 1994) that was identified as the primary nucleator of the branched filaments in the lamellipodia (Svitkina and Borisy, 1999). Localized at the leading edge of protruding cells in regions of high actin polymerization, Arp2/3 binds to the pointed end of actin filaments and nucleates new branches at an angle of approximately 70˚ from the pre-existing “mother” filament (Svitkina and Borisy, 1999; Volkmann et al., 2001). The complex consists of two actin related proteins, Arp 2 and 3, and five novel proteins, ARPC1-5 (mammalian homologs: p41-arc, p34-arc, p21-arc, p20-arc, and p-16 arc, respectively) (Figure 45). Reconstitution studies in insect cells showed that all seven subunits were needed for normal nucleating activity (Gournier et al., 2001). However, it.

Figure 45 Proposed crystal structure of the Arp2/3 complex.

The p20 and p34 subunits are believed to form the core of the complex, Arp2 and 3 are thought to function in the nucleation interface, and p16, p20, and p41 are though t to be involved in activation of the complex. (Borths and Welch, 2002; Gournier et al., 2001; Robinson et al., 2001; Winter et al., 1999)

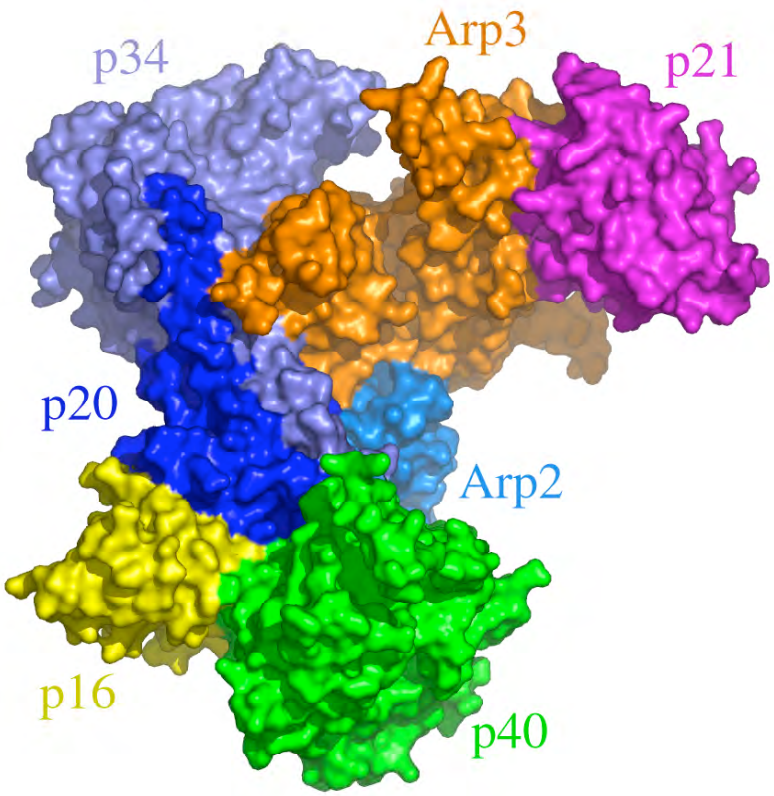

(Robinson et al., 2001)

was noted that complexes lacking either p41, p21, p16 or a combination of p21 and Arp3 could assemble, but had poor nucleating activity

Genetic studies of the Arp2/3 complex.

Genetic studies in budding yeast, Arabidopsis, and Drosophila have elucidated functions of the Arp2/3 complex. Yeast studies were performed shortly after the isolation of the complex (Machesky et al., 1994) and initially found Arp2 and 3 to be essential for viability (Huang et al., 1996; Winter et al., 1997). However, later studies found only the p40 subunit of the complex to be essential for survival (Winter et al., 1999). Deletions of the other subunits led to various growth defects, and problems with actin patch assembly and polarization that were subunit specific. Winter hypothesized that the differences were caused by individual subunit's roles in Arp activation, localization, and overall complex stabilization. The Arp2/3 complex was also shown to be important for normal morphology of many cell types in the mustard family plant Arabidopsis (Mathur et al., 2003). Arabidopsis genes WURM and DISTORTED1 are orthologs of Arp 2 and 3 respectively. Mutants of these two genes causes aberrant trichrome expansion, root hair, hypocotyls, and pavement cell defects. These defects were caused by distorted or absent fine actin structures, the appearance of F-actin aggregates, and vacuole fusion deficiencies.

In Drosophila, the Arp2/3 complex was shown to be critical for the formation of unique actin structural features. Loss of function mutations in the homologs of the Arp3 and p40 subunits showed defects in the ovarian ring canal expansion, but not in the

parallel bundled structures found in bristle shafts or nurse cell cytoplasm (Hudson and Cooley, 2002). Another developmental study using the p40 and Arp3 mutants showed CNS axon defects, characterized by defective commissural bundles (Zallen et al., 2002). In that study, the p40 mutant showed no axon defects, and the Arp 3 mutants showed moderate defects. The double mutant, however, showed severe defects, indicating an additive effect of the two mutations.

5.2 The role of Arp2/3 in neuronal growth cone and veil motility.

The results of the structural-kinetic analyses presented in Chapter 2 suggest a role for the Arp 2/3 complex in normal veil protrusion in the neuronal growth cone. They also suggest a novel role for Arp2/3 mediated veil formation along the sides of filopodia. However, while this data is suggestive, the question of function needs to be addressed using genetic studies. Studies of the mushroom body neurons of Drosophila containing null alleles for the Scar-Wasp-Arp pathway demonstrated that the Arp2/3 complex was not essential for axon growth in vivo (Ng and Luo, 2004). Strasser et al. drew a similar conclusion for hippocampal neurons in culture, in which Arp2/3 function had been diminished by expression of a dominant negative construct (2004). These studies raise the possibility that axon growth was driven by an Arp2/3 independent mechanism. Such a possibility has been presented by the discovery of two new families of actin nucleators, the formin (Kerkhoff, 2006; Michelot et al., 2005; Zigmond, 2004) and spire (Baum and Kunda, 2005; Quinlan et al., 2005) families that have been identified since the proposal of the array treadmilling model. Both have been shown to nucleate straight

actin filaments, but neither has been shown to generate branched actin filaments, raising the question of how they impact the array treadmilling model, and our general understanding of Arp2/3 function within this model. However, the conclusion that Arp2/3 is not essential for process extension does not preclude the possibility of it having a role in normal veil protrusion. Significantly, in the studies cited (Luo, 2002; Strasser et al., 2004), although axon outgrowth occurred, path finding was aberrant. Thus, further work is needed to directly address the function of Arp2/3 in growth cone motility per se. Using targeted depletion of the Arp2/3 complex by short interfering RNA (siRNA) we addressed these issues to better characterize the role of the Arp2/3 complex in cell and neuronal veil motility.

5.3 Results:

Choice of Cell Systems

The goal of this project was to evaluate the role of the Arp2/3 complex in generating a dendritic network, with a focus on its function in the growth cone, particularly in neuronal veils. We began by conducting preliminary studies of the effectiveness of Arp siRNA vectors in two tissue culture cell lines: one available in the lab, B16F1 melanoma, and a another, PC-12, donated by the Goldman laboratory. The motility, morphology, and actin cytoskeleton ultrastructure in B16F1 melanoma cells has been well characterized by our lab, making this line a logical choice. PC-12 (Rat, pheochromocytoma origin) cell lines are well published in the literature, and are easily transfected with high efficiency via electroporation. As an additional benefit, differentiation and process extension can

be controlled by media conditions. This allowed us to transfect with the knockdown vector (with or without the use of fluorescence activated cell sorting (FACS)), wait until knockdown had occurred, and then re-plate into differentiating media to study the effect on process extension and growth cone formation. Re-plating of primary neurons after process extension is currently not possible to our knowledge. So while neuronal tissue culture cell lines can only approximate primary neuronal cultures, they do offer a powerful system in which to begin to characterize certain aspects of protein knockdown in a neuronal system.

Primary neuronal cultures present additional unique challenges for siRNA experiments designed to test process extension after 72-96 hours after transfection with a siRNA plasmid. From a technical standpoint there are some clearly defined and non-trivial difficulties with obtaining functional data: (1) transfecting primary neuronal cultures in a high enough quantity to be able to perform a western blot analysis to demonstrate sufficient knockdown of the protein is virtually impossible by any technique. (2) primary neuronal cultures can not be FAC sorted to purify the culture for western blotting. (3) knockdown of a protein takes a finite amount of time – from 3-5 days – by which time substantial neurite outgrowth has occurred, and in our hands, the cultures no longer exhibit active growth cones.

Arp2/3 is localized in the growth cone veils in PC-12 cells.

Arp2/3 localization in motile fibroblasts and keratocytes has been established by our laboratory (Mejillano et al., 2004; Svitkina and Borisy, 1999). In these cells, Arp 2/3

staining is usually seen in band that co-localizes with actin at the extreme leading edge of the lamellipodia. It was also seen as the leading edge of neuronal veils in chick DRG growth cones, and in veils that formed along filopodia shafts (Figure 12). Arp2/3 localization has not been clearly demonstrated in the growth cones of PC-12 cells previously. PC-12 cells were immunostained with antibodies directed against the Arp3, p34, and p16 subunits of the Arp2/3 complex to evaluate the localization of the complex (Figure 46). The results were almost identical to those achieved in the chick DRG neurons shown in Chapter 2 (Figure 12, 13). Arp was localized to a band at the leading edge of the veils, though staining in the axon, central region, and cell body was more intense. As seen in chick DRG neurons, the staining was punctate, and distinct Arp puncta were observed dotting filopodia, both embedded and protruding from the growth cone (Figure 13B and C, puncta visible in the p34 inset, Figure 46). Control staining and immunoblotting demonstrated specificity of the p34 and Arp3 commercial antibodies (Figure 14 A-C). The p16 antibody was made and purified by our laboratory. myc-tagged Arp3 expressed in NG108 cells was recognized by both the anti-myc and anti-Arp3 antibodies and was localized appropriately to the leading edge of the cells (Figure 14 D).

5.4 Arp3-GFP localizes to the edge of protruding veils in PC-12 growth cones.

PC-12 cells were transfected with the Arp3-GFP plasmid, and live cell fluorescent imaging was performed. Arp3-GFP localized to the leading edge of the growth cone

Figure 46 Arp2/3 localization in PC-12 cells.

Immunofluorescent staining for Arp2/3 complex subunit p16. The left column contains p16 staining (green in merge), the center column contains phalloidin staining (red in merge), and the right column contains a merge of the two. High magnification insets of allow better visualization of staining in the small growth cone.

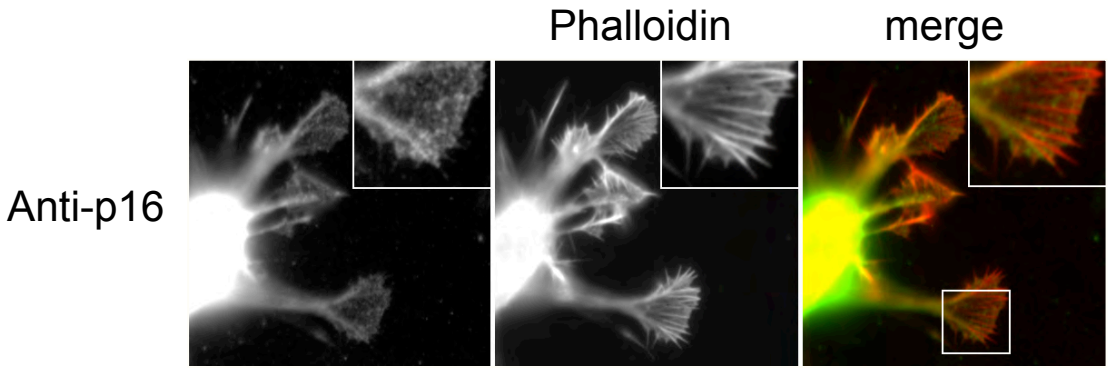
Phalloidin
merge
Anti-p16

(Figure 47A). However, intense fluorescence was also seen in the cell body, axon, and central domain. This brightness of both the cell body and the axon made it difficult to clearly visualize the expression at the leading edge of the veil. The neuronal veil is very thin by comparison to the central domain of the growth cone and the axon, and the volume difference could create the false impression of protein enrichment (Grzywa et al., 2006b). Conventional widefield microscopy cannot make this distinction. Total Internal Reflection Fluorescence (TIRF) microscopy, by comparison, images only the ~100nm closest to the ventral surface, creating an even optical field. Time-lapse sequences of PC-12 cells transfected with Arp3-GFP were acquired with TIRF, with still images taken at the end of the sequence in widefield for comparison. In widefield, the Arp3-GFP fluorescence was smooth but dim (Figure 47A). In TIRF, the staining became punctate, and was concentrated at the leading edge in protruding veils, decreased in retracting veils, and present along filopodia with associated veils (Figure 47B-C, also see Figure 15).

Strategy for Arp2/3 complex depletion.

A plasmid-based system for short hairpin RNA (shRNA) targeted depletion of proteins with a soluble GFP marker to allow identification of transfected cells was used to target the Arp2/3 complex for the depletion studies (Kojima et al., 2004). The plasmids and target construct designs are described in detail in the materials and methods (Figure 60, Figure 61). Our laboratory has used this system to successfully achieve knockdown of the cytoskeletal proteins fascin and capping protein

Figure 47 Localization of GFP-Arp3 expressed in PC-12 cells using TIRF microscopy.

A. PC-12 cell expressing GFP-Arp3 imaged using widefield fluorescence microscopy, the central region of the cell body is grossly overexposed in order to visualize the peripheral growth cone, giving the impression of enrichment in the central region. Scale bar = 5 μm. (right) B. The same cell imaged using TIRF microscopy a few seconds later, yielded an even optical field that revealed no enrichment in the central region. Red arrowhead marks bright Arp3 puncta along filopodium shaft. C. Higher magnification of boxed region in (B) showing Arp3 in two veils that protrude from the crotch of two pre-existing filopodia, away from the growth cone.

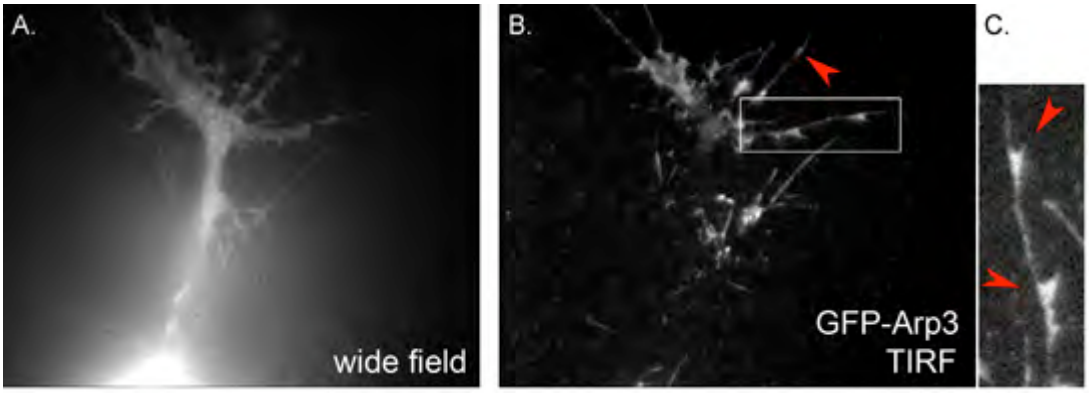
A.
wide field
B.
GFP-Arp3
TIRF
C.

(Mejillano et al., 2004; Vignjevic et al., 2006), and in both cases a strong phenotype was observed. Although capping protein is a dimer containing an alpha and beta subunit, targeted depletion of one subunit was sufficient to block the formation of active dimer. The non-targeted subunit also showed depletion at the protein level by immunoblot, although the cause is unknown. Arp2/3, however, is a seven protein complex, and partial complexes can form in the absence of a certain subunits and function, though they function at a very low level (Gournier et al., 2001). In order to keep the experiment technically simple, our goal was to disable the complex by depletion of a single subunit. *In vitro* work performed by Gournier, et al. using individual purified components of the complex, identified p20 and p34 subunits as essential to the assembly of the complex. The Arp3 subunit, while not necessary for complex assembly, was reported to be essential for the nucleating ability of the complex (2001).

Depletion of p34 subunit in PC-12 cells.

The central location of the p34 subunit in the Arp2/3 complex, and the reported inability of the complex to assemble in insect cells in the absence of p34, suggested that it would be a strong candidate for eliminating functional Arp2/3 by targeting only a single subunit. I designed two targeting constructs against the p34 subunit (T1, T2), and two control (T2*H, T2*NH) constructs containing a two nucleotide mismatch to the T2 targeting construct (Figure 48). An additional T2 targeting construct, containing a modified loop region (T2ML), was also made as an experiment to test a different loop coding sequence. The two base pair mismatch control constructs were used as

Figure 48 p34 siRNA target sequences.

All target sequences are shared with both the mouse and rat p34 genes. There was no homology to the human p34 gene, allowing us to use the human gene for rescue without mutagenesis. p34T1 (T1) and p34T2 (T2) were the primary p34 targeting constructs designed. T2ML contained the T2 target sequence, but contained a modified Agami loop, created as an experiment to test efficiency with alternate loop sequences. T2*NH was the mismatch control for the T2 targeting construct. The “NH” stands for non-human, indicating the construct did not target the rodent gene. The T2*H (human) construct also served as a mismatch control to the T2 targeting constructed, but additionally, it targeted the human p34 gene.

p34 Target and Mismatch Control Sequences

pSuper Vector	Fluor	Target Gene	Target sequence	Ref nt	Rat nt
p34T1	GFP	p34-Arc	tgccactgctcgagacaac	783-802	740-759
p34T2	GFP	p34-Arc	ggc**C**tatat**T**ca**T**acacg**A**	860-879	816-835
p34T2, modified loop	GFP	p34-Arc	ggc**C**tatat**T**ca**T**acacg**A**	860-879	816-835
p34T2* nonhum ctrl	GFP	p34-Arc	ggcAtatatGcatacacga	860-879	816-835
p34T2* human ctrl	GFP	p34-Arc	ggcctatattcaCacacgT	860-879	816-835

controls along with the empty siRNA vector in all experiments to evaluate specificity of the target sequence and off target effects. The first control construct, T2*H, also targeted the human rescue vector, and was designed for use with a fluorescently labeled rescue vector to distinguish between human and rodent targeting. The second control construct, T2*NH, did not target the human rescue vector, and was the primary control construct used in all experiments. The mismatch control targeting constructs were made after the initial immunoblot analysis demonstrated successful knockdown of p34. No mismatch controls constructs were designed for the T1 target. The depletion of p34 by the T1 targeting construct in the initial experiments was not as strong as we would have liked, and we felt that our efforts should be focused on the target with the strongest knockdown.

The PC-12 lysates were not sorted for the initial experiments; however a transfection efficiency was calculated, with a range of ~73-89%. The transfection efficiency of each sample was measured by scoring the number of GFP (+) cells in 100 cells immediately prior to the preparation of lysate. All samples were run in duplicate for each experiment. All blots were probed with an anti-tubulin antibody as a loading control. The knockdown data was then adjusted for both tubulin and transfection efficiency on a sample-by-sample basis as described in the materials and methods section (Chapter 7). In some samples, a negative result was achieved after adjusting for transfection efficiency. It is possible that this resulted from cells whose GFP signal was too faint to detect, yet experienced full knockdown, thus falsely underestimating the transfection efficiency.

Figure 49 Depletion of p34 Subunit.

(A) Representative immunoblot showing depletion of p34 protein from day 2 to day 4 after transfection using the T2 targeting construct. Tubulin immunoblotting was used as a loading control, and percent knockdown was calculated relative to tubulin staining and then adjusted for transfection efficiency. 15 µg of protein was loaded into each lane for all gels. ~14.9% of p34 protein remained at 96 hours. The control lane contains cells transfected with the pGSuper construct lacking the hairpin cassette. (B) Representative immunoblot showing levels of p34, Arp3, and p16 protein 96 hours after transfection with empty vector, T1, T2, and T2*NH (T2*NH was used in all experiments as the primary mismatch control construct). Transfection with the T2 targeting construct led to ~85% depletion of p34 protein, ~76% depletion of p16, and 90% depletion of Arp3 subunits. Transfection with the T1 targeting construct depleted only ~73% of p34 and p16, and ~95% of Arp3. (C) Representative immunoblot showing levels of VASP, Capping Protein (CP), and cofilin 96 hours after transfection with empty vector, T1, T2, and T2*NH targeting constructs.

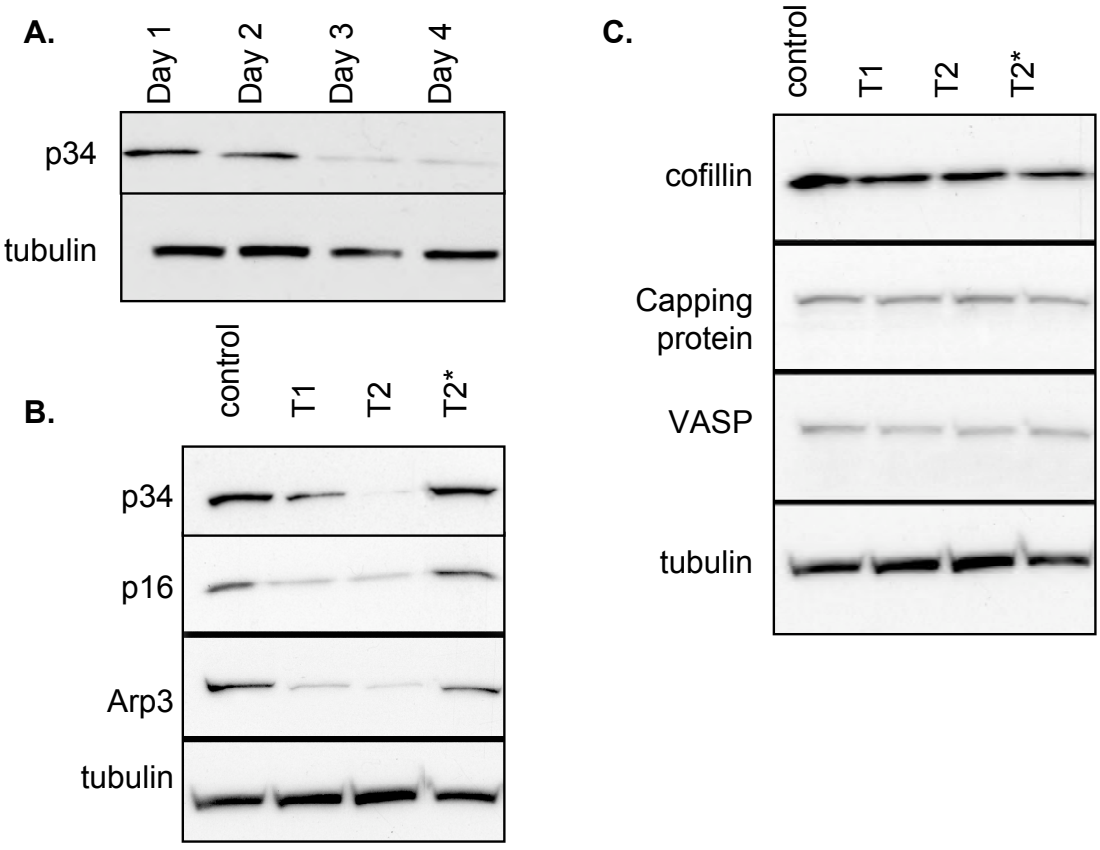
A.
Day 1
Day 2
Day 3
Day 4
p34
tubulin
B.
control
T1
T2
T2*
p34
p16
Arp3
tubulin
C.
control
T1
T2
T2*
cofillin
Capping protein
VASP
tubulin

Table 1 Summary of p34 depletion by immunoblot.

The average % remaining RAW refers to the average knockdown calculated from the digitized immunoblots, representing (N#) of separate experiments, but not adjusted for transfection efficiency. The % remaining transfection adjusted represents the average of the p34 protein remaining after each sample was adjusted for transfection. For the data reported in this table, transfection efficiency ranged from 73-89%.

Plasmid	Day post transfection	avg % remaining RAW	% remaining transfection adjusted	N #
Anti-p34				
T1	1	82.8	70.3	2
	2	101	83.6	2
	3	70.2	52.7	2
	4	41.4±16	27.4	4
T2	1	89.2	71.7	2
	2	78.5	61	2
	3	42.4	24.9	2
	4	28.9±9.4	14.9	4
T2ML	1	20.5	5.0	2
	2	12.2	-7.8	2
	3	31.7	15.7	3
	4	30.5±32	12.7	4
T2*NH	4	132.6	109.6	2
T2*H	4	84.6	72.6	2
Anti-p34 - FAC Sorted cells				
T1 FACS	4	11	-	2
T2 FACS	4	8.5	-	2
T2*NH FACS	4	36.7	-	2
Anti-p16				
T1	4	36.6	27.9	3
T2	4	41.4	23.7	3
T2*H	4	95.9	61	2
T2*NH	4	110.1	71.7	2
Anti-Arp3				
T1	4	15.6	3.6	2
T2	4	6.6	-4.4	2
T2*H	4	19.7	8.7	2
T2*NH	4	69.4	46.4	2
Anti-VASP				
T1	4	63.5	51.5	2
T2	4	71.2	60.2	2
T2*H	4	78.0	67	2
T2*NH	4	59.8	36.8	2
Anti-Capping Protein				
T1	4	98.5	86.5	1
T2	4	108.1	97.1	1
T2*H	4	79.5	68.5	1
T2*NH	4	100.7	77.7	1
Anti-Cofilin				
T1	4	80.5	68.5	1
T2	4	75.9	64.9	1
T2*H	4	63.3	52.3	1
T2*NH	4	61.8	38.8	1

Knockdown of the p34 protein using the T1 and T2 constructs reached a maximum at 72-96 hours in PC-12 cells as evaluated by immunoblot (Figure 49A, Table 1). The T2 construct resulted ~70% depletion of p34 protein, which was increased to ~85% when corrected for transfection efficiency (Table 1). The T1 construct depleted only ~59% of p34, which was increased to ~73% when corrected for transfection efficiency. The mismatch control (T2*NH) construct did not deplete the p34 subunit in PC-12 cells. Depletion of ~76% depletion of p16 and 90% of Arp3 by T2, and ~73% of p16 and ~95% of Arp3 was seen at 96 hours (Figure 49B). The mechanism of this depletion is unknown, but was also observed during capping protein depletion experiments performed in the laboratory (Mejillano et al., 2004). In these experiments of the ß subunit led to a comparable knockdown of the α subunit, which was then restored when rescue with the ß subunit was performed.

FACS was employed to reduce the need to correct for transfection efficiency, as it had been very effective in purifying population B16F1 melanoma cells in the laboratory. Four attempts were made to sort PC-12 cells transfected with T1, T2, T2*, and the control constructs. The control consisted of the same transfection factor containing a GFP expression cassette and only lacking the hairpin targeting sequence (EV). The first 2 trials, performed at 24 and 48 hours after electroporation resulted in recovery of only 28-84,000 cells, and were accompanied by near complete cell death 24 hours following the sort. The last two attempts, run at 72 hours following electroporation recovered ~150,000 cells per sample and a sufficient number of cells survived for lysate preparation. These samples were not adjusted for transfection efficiency. Immunoblot

analysis revealed that T1 depleted ~89%, T2 depleted ~91.5%, and, T2*NH depleted ~63.3% of p34 relative to the FAC sorted control (Table 1). We could not explain why the mismatch control construct reduced p34 in the FACS population, while it did affect it in the unsorted population.

The blots were also probed with antibodies against other common cytoskeletal proteins, VASP, cofilin, and capping protein, to determine if p34 depletion had caused effects on other related protein levels. No changes were observed in levels of capping protein. VASP (50, 48%) and cofilin (30, 35%) levels were decreased by both the T1 and T2 targeting constructs (Figure 49C). However, these levels were also decreased in both of the mismatch control samples. No knockdown was observed for VASP or cofilin in FAC sorted B16F1 melanoma cells (Figure 52).

Process Extension is impaired in PC-12 cells depleted of p34.

Electroporated PC-12 cells were re-plated and stimulated with NGF to extend processes (Figure 50A). Transfected cells were scored as GFP positive 72-96 hours after electroporation. The proportion of GFP (+) cells extending processes was ~17.7% (n=141) for the T2 construct, 36.9% (n=84) for the T1 construct, 46.8% (n=47) for T2*, and 77.3% (n=22) for the empty vector (Figure 50B). Non-transfected cells were scored as GFP negative. The proportion of GFP (-) cells extending processes was ~58% (n=88) for the T2 construct, 33.3% (n=54) for the T1 construct, 58.5% (n=41) for T2*, and 62.5% (n=32) for the empty vector (Figure 50B). For T2, inhibition of process extension was significant either when compared to GFP negative cells on the same dish

Figure 50 PC-12 cells depleted of p34

(A) Upper panel shows soluble GFP fluorescence, indicating transfection with a pGSuper construct. Lower panel shows phalloidin staining and phase contrast images. Left column is a high magnification image of a characteristic PC-12 cells challenged to differentiate 96 hours after transfection with T2 targeting construct. Note the numerous stress fibers and stumpy processes. The center column shows a low magnification image from the same coverslip, with an untransfected cell in the center showing normal process extension, surrounded by transfected cells that fail to extend processes. The right column shows a PC-12 cell transfected with the T2*NH targeting construct, that shows normal process extension. (B) Summary of process extension in p34 depleted PC-12 cells. Process length is measured in μm.

A.

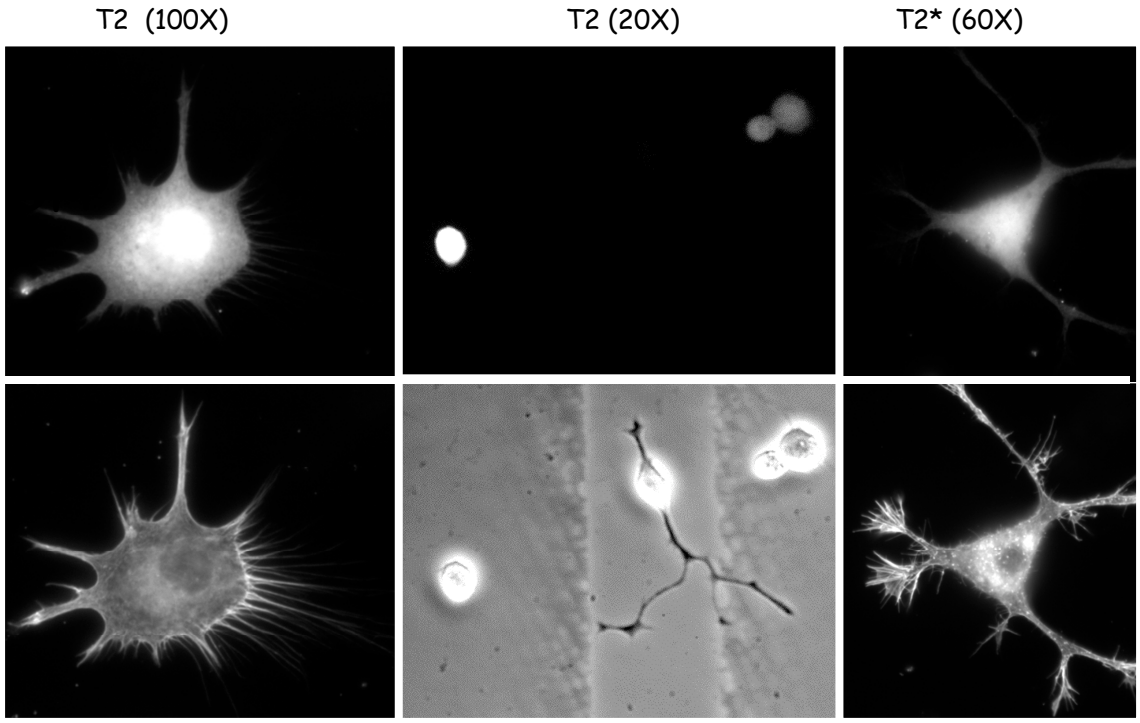

B.

phalloidin phase phalloidin

PC-12 cells, plated 72 hrs post transfection		cells counted	cells with processes	total process #	% cells with process	p value between GFP+ vs. GFP-	p value between target and control	avg process length	# of processes
GFP +	pGT2	141	25	48	17.7	0.0000	0.0000	121.9±85.9	48
GFP (-)	pGT2	88	51	101	58.0		0.2151	186.5±112	101
GFP +	pGT1	84	31	183	36.9	0.6715	0.0006	126.4±52.7	183
GFP (-)	pGT1	54	18	55	33.3		0.4472	82.2±81.2	55
GFP +	pGT2*	47	22	68	46.8	0.2771	1.0000	73.5±63.5	68
GFP (-)	pGT2*	41	24	42	58.5		0.2486	146.8±119	42
GFP +	EV	22	17	36	77.3	0.0207	-	95.1	36
GFP (-)	EV	32	20	33	62.5		-	80.0	33

or to GFP positive cells on other dishes transfected with the control empty vector. For T1, there was no significant difference in process extension between GFP (+) and (-) cells, though the decrease was significant for both groups when compared to control. There was no significant difference in process extension between GFP (+) and (-) cells transfected with T2*, and T2* did not differ significantly from control cells. The large standard deviation of the process lengths rendered all differences in length non-significant. GFP (+) cells transfected with T1 and T2, that had formed processes, were indistinguishable from wild-type, non transfected PC-12 cells. These results indicate that while p34 depletion with T1 and T2 targets does decrease process formation, it does not entirely suppress it. This could be a result of insufficient depletion of protein, formation of small amounts of active complex lacking the p34 subunit, or compensation by other cytoskeletal proteins.

PC-12 cells plated 24 hours after transfection with T1, T2, and T2* targeting constructs were able to form normal processes and growth cones. However, by 96 hours many knockdown cells assumed a spread out, almost polygonal shape that lacked discrete processes. These cells often appeared spiky, and had actin staining in what appeared to be numerous stress and retraction fibers. Cells transfected with T2* analyzed at 96 hours were indistinguishable from untransfected PC-12 cells. This was a qualitative observation, and was not quantified (Figure 51).

Figure 51 Cell shape maintenance in PC-12 cells plated immediately after transfection.

Upper panel GFP fluorescence, Lower panel phalloidin staining. PC-12 cell transfected with T2 can extend normal processes when challenged to differentiate 24 hours after transfection. By 96 hours after transfection, cells challenged to differentiate at 24 hours often appeared large by comparison to other PC-12 cells with wide, irregularly shaped processes and numerous stress/retraction fibers by phalloidin staining.

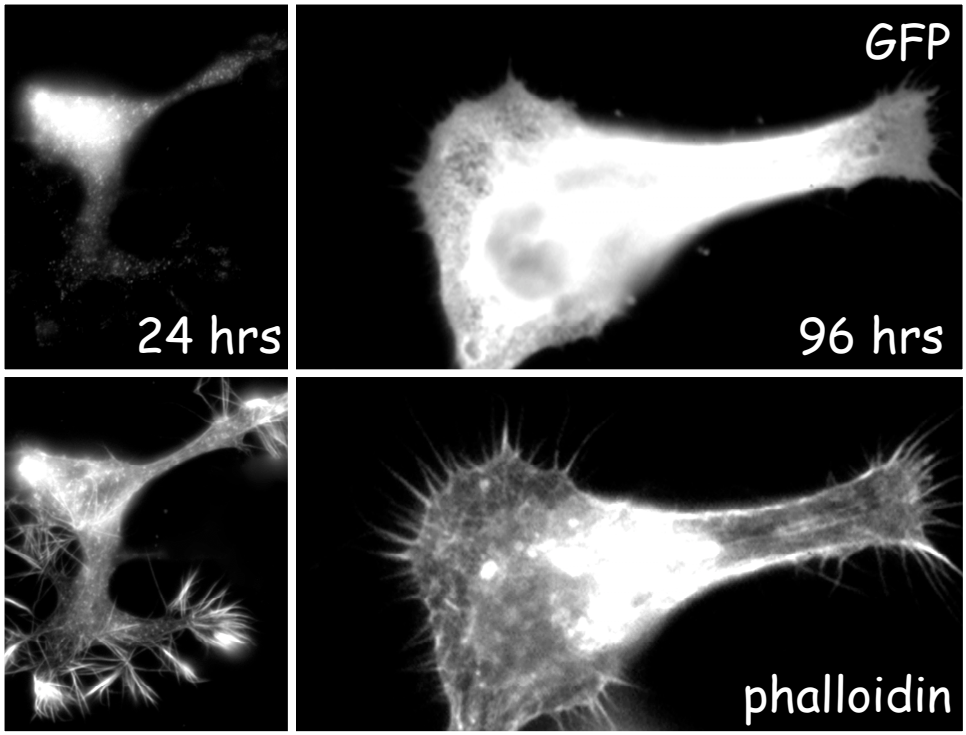
GFP
24 hrs
96 hrs
phalloidin

Evaluation of knockdown by immunostaining.

Immunostaining to evaluate loss of p34 in PC-12 lacking processes was uninformative. PC-12 cells, as do B16F1 melanoma, normally present with residual staining in the center of the cell body when stained for Arp3, p34, and p16, which does not stain the growth cones, as was shown in our control staining earlier. However, in the absence of an active growth cone, immunostaining against Arp subunits was identical for all PC-12 cells. Of the 48 processes examined in T2 transfected PC-12 cells plated after 72 hours, 9 had growth cones, and 5/9 did stain positive for p34. This may indicate insufficient knockdown of p34 occurred in these cells.

p34 knockdown in B16F1 melanoma cells.

The results of the p34 knockdown in PC-12 cells suggested that an interesting phenotype for p34 depletion might exist. However, the variability of immunoblot results with FACS and the presence of a persistent population of GFP (+) cells with a wild type phenotype precluded us from drawing strong conclusions from these results. We therefore pursued knockdown of p34 in the B16F1 melanoma cells that are commonly used in the laboratory. These motile fibroblasts are well studied by the lab and the actin organization at both the light microscopic and EM levels has been characterized. The knockdown of fascin and capping protein published by our laboratory was done in B16F1 cells, and a robust phenotype was observed in depletion of both proteins. We hoped that depletion of p34 in B16F1 cells might provide a more consistent phenotype for characterization, and allow us to better interpret our observations in PC-12 cells.

With the help of Llyuba Czech, a research associate in the lab, extensive western blot analysis on a FAC sorted population of B16 cells transfected with the empty vector, T2, and T2*NH was performed. In B16F1 cells, optimal knockdown was achieved at 5 days following transfection. At this point in time, the population contained ~20-30% non-transfected cells. After correcting for GFP negative cells, approximately 17.2% of p34, and 61.3% of the Arp3 protein remained (Figure 52). However, a 33% reduction in p34 was noted in cells transfected with T2*. No reduction, and in fact a ~33% excess, of Arp3 was found in cells transfected with T2*. A similar decrease in p34 had been seen with the T2* control after FACS in PC-12 cells, though it was not seen in the unsorted cells, indicating FAC sorting in PC-12 cells may have adversely affected the experiment. Transfection with the T1 construct resulted in only ~59% depletion of p34 in FAC sorted B16F1 cells by immunoblot, and as a result, extensive analysis was not performed for this construct.

The blots were also probed with antibodies against Cortactin, VASP, Fascin, and Gelsolin (Figure 52A). A three-fold increase in cortactin, a two-fold increase in VASP and Gelsolin, and a 50% reduction in fascin were noted (Figure 52B). However, these changes were noted in both the knockdown and mismatch control vectors, and the results were duplicated in a subsequent experiment. These preliminary results suggested the possibility of non-specific effects of the T2 targeting constructs in B16F1 melanoma cells.

B16F1 cells depleted of p34 displayed an interesting, but variable morphology that could usually be distinguished from control cells in phase contrast images

Figure 52 Western Blot Analysis of p34 Knockdown in FAC sorted B16F1 cells

A. Representative immunoblot from B16F1 cells transfected with empty vector, T2, and T2*NH. Cells were FAC sorted two days later, and lysate was collected for immunoblot analysis five days after transfection. It was estimated that ~25-30% of the cells were no longer GFP positive at day 5. A 50-fold protein concentration range of empty vector transfected control cells was run. A density slope was generated from controls, and experimental sample concentration was derived from this slope. Samples T2 and T2(*) were run in triplicate. B. Table summarizing knockdown results.

A.

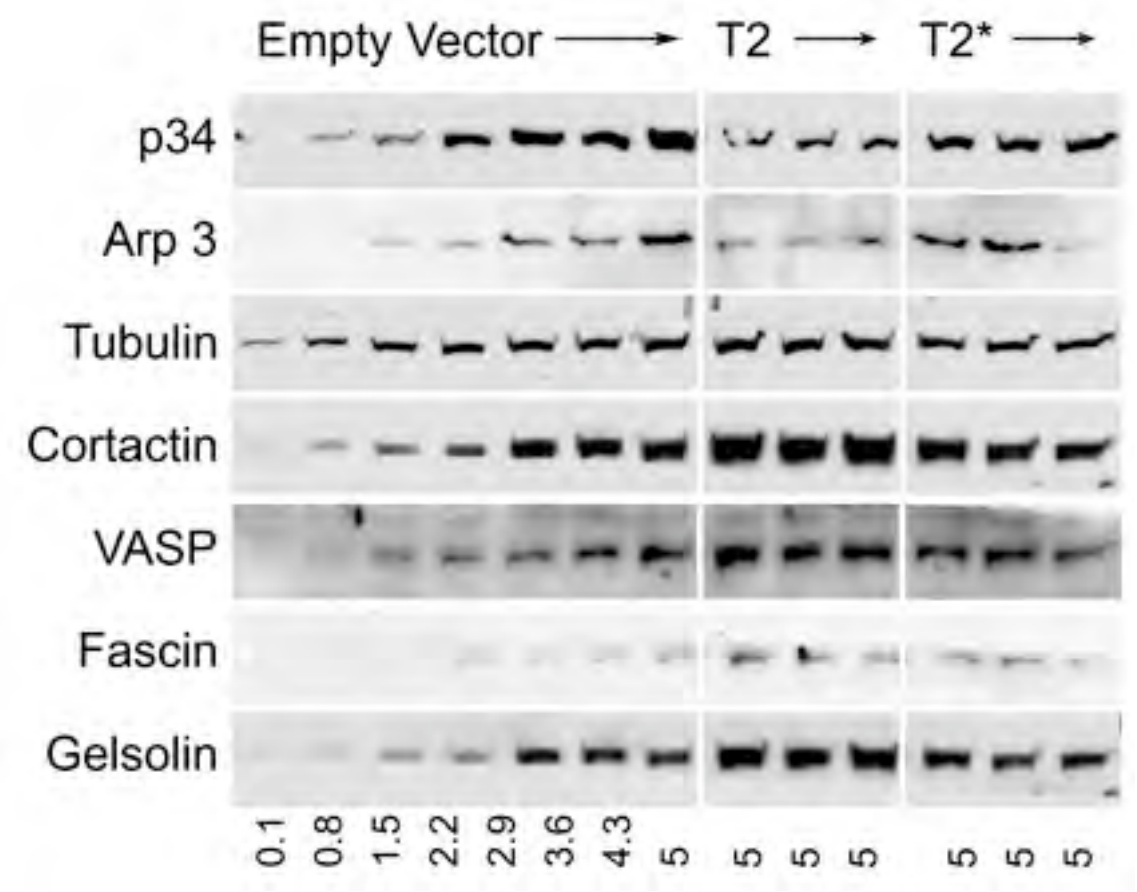

B.

Antibody	Plasmid	% remaining	Std Dev
p34	T2	17.2	11
	T2*	67.3	31
Arp3	T2	61.7	16
	T2*	133.9	43
cortactin	T2	276.3	8
	T2*	217.0	32
Gelsolin	T2	268.3	32
	T2*	194.7	6
Vasp	T2	179.0	26
	T2*	147.7	21
Fasicn	T2	52.0	9
	T2*	38.3	16

(**Error! Not a valid bookmark self-reference.**A). We characterized the knockdown phenotype by evaluating the presence or absence of lamellipodia formation and p34 immunostaining within two hours of plating on the third, fourth, and fifth days following transfection (**Error! Not a valid bookmark self-reference.**). From 3 to 5 days after transfection, ~22% of cells transfected with T2, and scored as GFP (+), were able to form lamellipodia, compared with 61% of cells transfected with T2* and 81% of cells transfected with the control construct. Over this same time period, ~17% of cells transfected with T2, and scored as GFP (+), stained positive for p34, compared with ~77% of cells transfected with T2* and 83% of cells transfected with the control construct. This represents a significant reduction in both lamellipodia and p34 immunostaining ($p < 0.0001$ for T2 compared to both T2* and EV). The T1 construct, on average, did not significantly reduce lamellipodia formation (61%) or p34 staining (65%) as measured on days 3 and 6 following transfection. We also noted that GFP (-) cells, on the same dish as those transfected with T2, also had significantly decreased lamellipodia formation and p34 staining when compared to EV controls. These results suggested that knockdown might be occurring in cells that were no longer expressing GFP, making it difficult to accurately measure transfection efficiency and, ultimately, knockdown with the T2 construct. This decrease was not seen in cells transfected with the T1 target.

An additional difficulty that arose during the experiments was the discovery that the p34 subunit, chosen for its central location in the complex, could not be fluorescently tagged to allow for rescue. Dr. Welch, who had donated the unlabelled construct to the

Figure 53 Phenotype of B16F1 melanoma cells depleted of p34.

A. Representative B16 cell (in GFP) transfected with T2 is surround by GFP negative cells. The cell remains unspread, and has long spinous processes projecting around its perimeter.

B. Lamellipodia formation in GFP (+) cells transfected with T1 & T2 was significantly reduced compared to GFP (-) cells transfected with the same vectors on days 3, 4, & 5 for T2, and day 3 for T1. Lamellipodia formation in GFP+ cells transfected with T2* was not significantly reduced compared to GFP (-) cells transfected with the same vector on days 3, 4, & 5. However, there were significant differences in lamellipodia formation between GFP (+) and (-) cells transfected with the empty vector.

C. p34 staining in GFP+ cells transfected with T1 & T2 was significantly reduced compared to GFP (-) cells transfected with the same vectors on days 3, 4, & 5 for T2, and day 3 for T1. p34 staining in GFP+ cells transfected with T2* was not significantly reduced compared to GFP (-) cells transfected with the same vector on days 3, 4, & 5. There were a slight difference in p34 staining between GFP (+) and (-) cells transfected with the empty vector on Day 6.

A

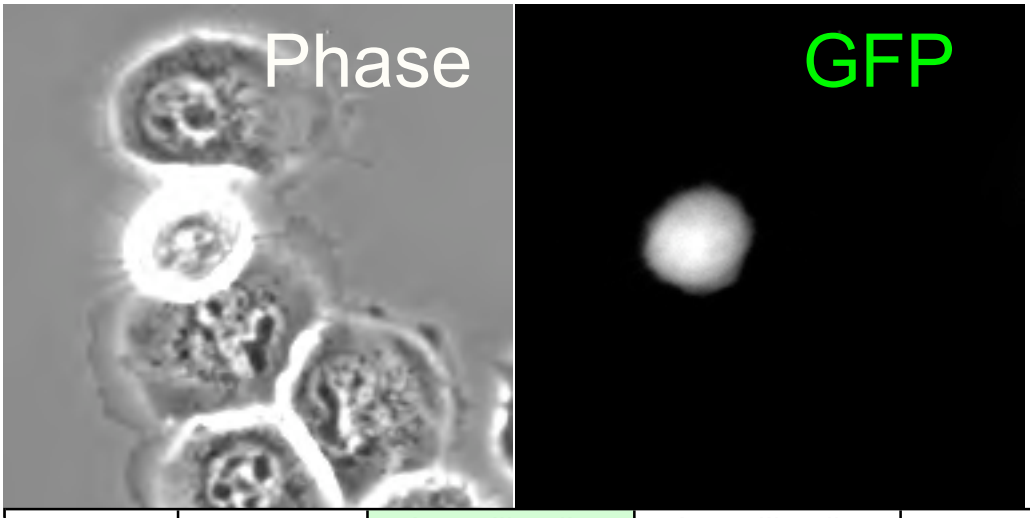

B.

Plasmid	Day# after transfection	Lamellipodia +	Lamellipodia -	Lamellipodia +	Lamellipodia -	p value
T2	3	26	74	42	58	0.0168
	4	18	82	35	65	0.0063
	5	23	77	59	41	0.0000
T2*	3	62	38	68	32	0.3763
	4	59	41	69	31	0.1421
	5	61	39	81	19	0.0017
T1	3	45	55	94	6	0.0000
	6	77	23	80	20	0.6077
EV	3	64	36	89	11	0.0000
	6	81	19	69	31	0.0504

C.

Plasmid	Day# after transfection	p34 staining +	p34 staining -	p34 staining +	p34 staining -	p value
T2	3	26	74	52	48	0.0001
	4	9	91	75	25	0.0000
	5	17	83	76	24	0.0000
T2*	3	71	29	75	25	0.5265
	4	71	29	73	27	0.7543
	5	90	10	30	70	0.0000
T1	3	52	48	93	7	0.0000
	6	79	21	86	14	0.1945
EV	3	79	21	88	12	0.0873
	6	85	15	95	5	0.0183

Figure 54 Confounding results seen with pG-Super p34 T1/T2 vectors:

Lamellipodia formation and p34 staining in GFP+ cells transfected with the siRNA vectors T1 & T2 was significantly reduced when compared to GFP+ cells transfected with pG-Super empty vector. Lamellipodia formation and p34 staining in GFP+ cells transfected with the T2* (mismatch control to T2) construct was not significantly reduced compared to GFP+ cells transfected with pG-Super empty vector. Lamellipodia formation and p34 staining in GFP (-) cells transfected with the T1 was not significantly reduced compared to GFP (-) cells transfected with pG-Super empty vector. Lamellipodia formation and p34 staining in GFP(-) cells transfected with the siRNA vectors T2 & T2* was significantly reduced compared to GFP(-) cells transfected with pG-Super empty vector. The expectation is that amongst the GFP (-) cells there should be no significant difference over empty vector, especially with the mismatch control (T2*). Therefore, both T2 & T2* vector appear to have some off target effects in addition to depletion of p34.

Day 5 after trans-fection	Lamellipodia		p34 staining	
	GFP (+) control cells	GFP (-) control cells	GFP (+) control cells	GFP (-) control cells
T2	0.0000	0.0000	0.0000	0.0000
T2*	0.7710	0.0003	0.1933	0.0178
T1	0.0068	0.2068	0.0000	0.2300

laboratory, had been unsuccessful in his attempts to create a functional GFP tagged construct, and it was thought that stearic hindrance caused by the large GFP moiety might impair the other Arp2/3 subunits from assembling properly (personal communication from Dr. Welch). As an alternative, I constructed a p34-pIRES-GFP construct that would express a soluble GFP tag along with unlabelled p34. Unfortunately, wild type cells transfected with this construct developed a hyper motile phenotype and no longer appeared normal, making us hesitant to use the construct. I then created a p34-myc tagged construct that was expressed in wild type cells without any change in phenotype. p34 did localize properly by anti-myc immunofluorescent staining. However, as it had no visible tag, rescue would only be evaluated by fixation and immunostaining, and motility during rescue could not be evaluated.

The results of the p34 knockdown experiments in both PC-12 and B16F1 melanoma cells suggested an effect on lamellipodia formation and process extension. However, inconsistencies in the immunoblots, mismatch control data, and the appearance numerous wild type cells transfected with the knockdown constructs made it impossible to draw any firm conclusions. These inconsistencies, combined with the inability to create a fluorescently labeled rescue construct, led us to pursue an alternate target for knockdown of Arp2/3.

5.5 Depletion of Arp3 subunit

The Arp3 subunit was chosen as the next target for siRNA depletion. We chose this subunit as it had been shown to be essential for Arp2/3 assembly (Gournier et al.,

2001), and a functional GFP tagged plasmid was present in the lab, and had been successfully expressed in B16F1 and PC-12 cells. In the time since the creation of targets for the p34 experiments, advances had been made in both siRNA target selection “rules”, as well as the silencing plasmid used by the lab. The new siRNA construct (pGSHIN-2) was used in conjunction with a reporter construct (p-REFLECT-R) (Figure 60B). Used together, this system would allow sensitive calculation of knockdown through analysis of fluorescence ratios (see materials and methods, Figure 61) as well as by traditional immunoblotting. The fluorescent analysis would be more rapid than immunoblotting, and would allow us to screen a greater number of target constructs in an effort to identify a strong knockdown reagent.

Six targets (T1-T6), with sequences conserved in both rat and mouse, were chosen using the Invitrogen BLOCK-iT™ RNAi Designer after inputting the mouse, human, and rat Arp3 genes (Figure 55) (Invitrogen, 2007). The T1 and T4 targets were also conserved in the human Arp3 genes. I cloned the all six targeting constructs into both the pGSHIN-2 expression vector, as well as the pReflect-R test vector. T2 was predicted to be a poor target, and was purposely chosen to provide a positive test for the fluorescence assay.

Western blot analysis was performed on B16F1 cells (FAC sorted 24 hours after transfection) 96 hours after transfection (Figure 56). While we did not adjust for transfection efficiency, it was noted that between 10 and 20% of the cells across the 6 constructs and control vectors were GFP negative at the time lysate was collected. Transfection with T4, T5, and T6 constructs resulted in >98% Arp3 depletion by

Figure 55 Target sequences for Arp3 siRNA experiments.

All sequences are shared with both the mouse and rat Arp3 genes. T1 and T4 are also conserved in the human Arp3 gene. T1, T3, T4, T5 and T6 were selected by importing the sequence of the mouse, rat, and human Arp3 genes Invitrogen's BLOCK-iT™ RNAi Designer software. T2 was purposely selected and predicted as an unfunctional target. Loop sequence is GCTTCCTGTCAC (miR23-loop).

Arp3 target sequences		
Target #	Target Sequence	Gene location
T1	gcagctgtattaaacacat	(464-482 of CDS)
T2	acattgtcctctctggtgg	(857-875 of CDS)
T3	gcccaagcctattgatgta	(981-999 of CDS)
T4	gcctgagttctaccaagta	(1065-1083 of CDS)
T5	ggagtcatgtcctaaagtt	(1147-1161 of CDS + 1-4 of 3'UTR)
T6	gcttggatctaagaagcta	(534-552 of 3'UTR)

Figure 56 Arp 3 Knockdown Verification

Representative immunoblots of B16F1 cells 96 hours after transfection with empty vector or T1-T6, probed for Arp3 and tubulin. Cells were FAC sorted 24 hours after transfection, and approximately 10-20% of the population was GFP negative. Three exposure times were used to amplify any remaining signal Arp3 signal. I did not detect any signal for Arp3 in samples transfected with T4, T5, or T6 after a 30 minute exposure. A weak signal was seen in the lysates of cells transfected with the T1, T2, and T3 vectors at 30 minutes that corresponded to a knockdown of approximately 93%, 91%, and 96% of Arp3, respectively.

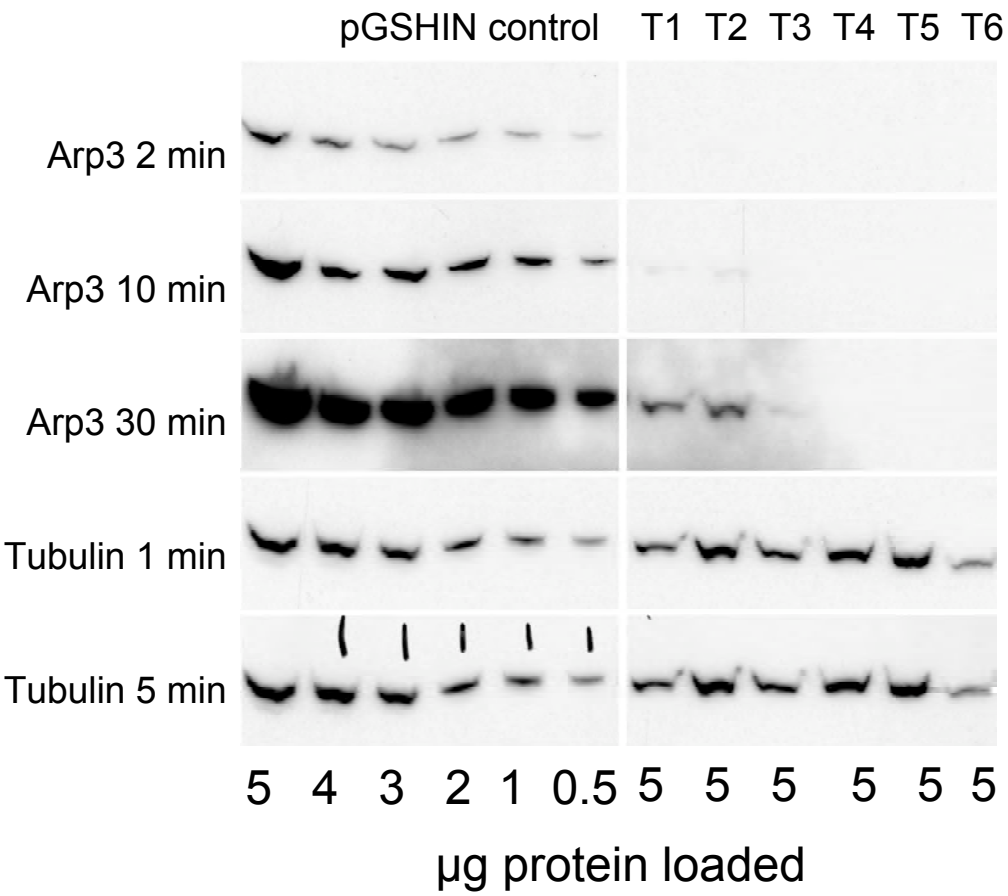
pGSHIN control
T1 T2 T3 T4 T5 T6
Arp3 2 min
Arp3 10 min
Arp3 30 min
Tubulin 1 min
Tubulin 5 min
5 4 3 2 1 0.5 5 5 5 5 5 5
µg protein loaded

Figure 57 KD index values for Arp3 T1-T6 constructs.

A. Representative images of the Rat2 cells transfected with pGSHIN2-GFP and pREFLECT-R. Each row contains four images of the same cells: phase contrast, GFP, dsRED, and a merge of the GFP and dsRED channels. The T4 (low KD index, strongest knockdown) and T2 (high KD index, weakest knockdown) targets are shown. (upper panel) The T4 test channel (Gtest/Rtest) shows very little signal in the dsRed channel, indicative of successful targeting and depletion of the dsRED with target sequence. The lack of dsRed causes the merge channel to appear green, instead of yellow, as in the control (Gtest/Rcontrol), which contains a non-targeted DSred transcript. (lower panel) The T2 test channel shows little depletion of the dsRed signal, and the test merge image is similar to the control merge. (B) A table summarizing the knockdown index calculated by Drs. Danciu and Kojima. The calculations are shown in the materials and methods (Figure 61). Briefly, the index was generated by evaluating the ratio of green fluorescence from the pGSHIN-2 empty vector (ctrl) or pGSHIN-2 target-containing vector (test) to red fluorescence from the pReflect-R empty vector (ctrl) or pReflect-R target containing vector. A KD index value of less than 1 indicates extremely strong knockdown. The T1 and T4 constructs provided the deepest knockdown. The T2 construct was intentionally designed as a poor target and only achieved 60% protein depletion.

A.

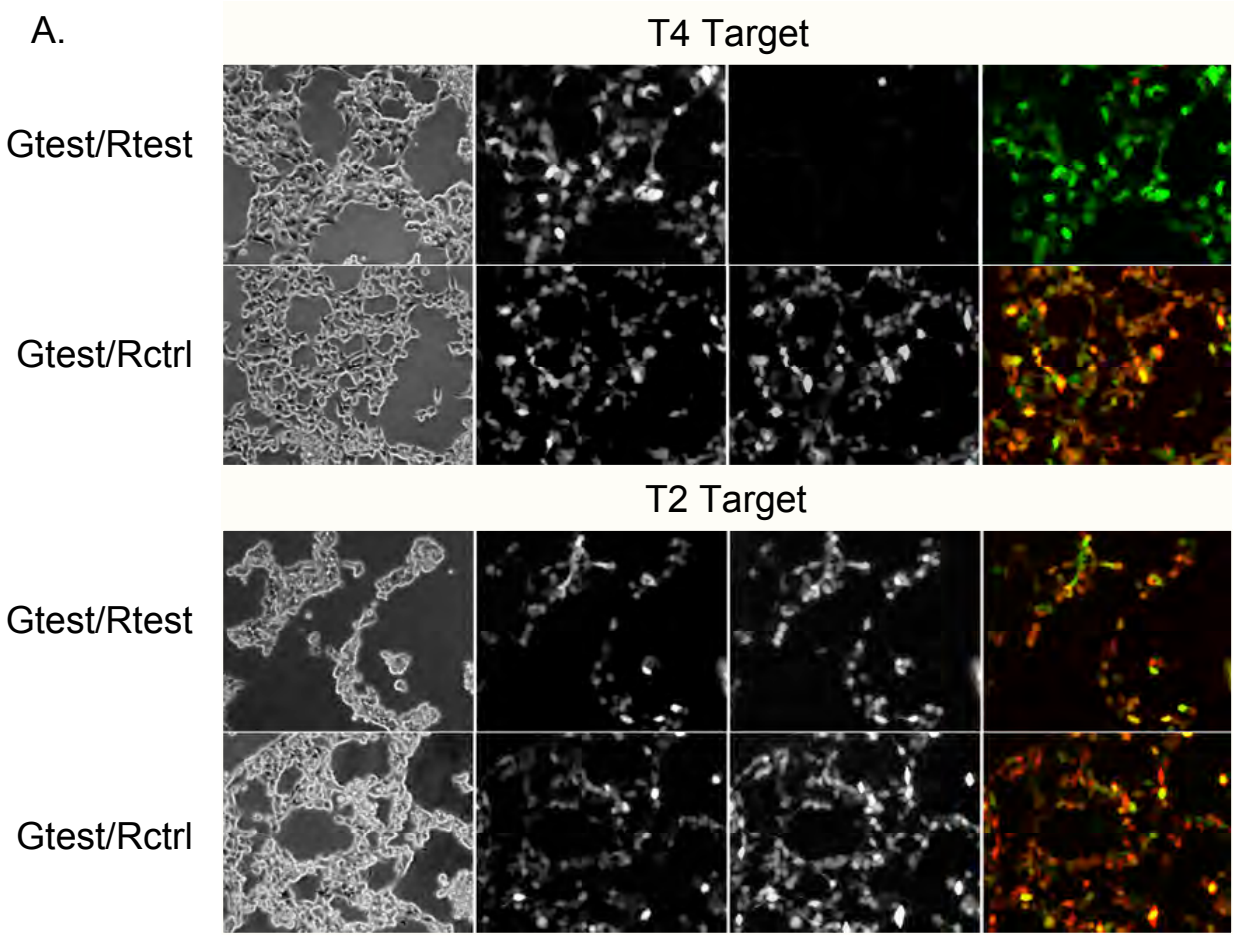

B.

pSHIN-G	pREF-R		T1	T2	T3	T4	T5	T6
test	test	median	0.045	0.387	0.065	0.047	0.103	0.083
		dev	0.072	0.328	0.077	0.099	0.089	0.100
		N	190.0	396.0	234.0	235.0	195.0	290.0
ctrl	test	median	2.780	1.323	2.274	1.920	2.007	1.760
		dev	1.514	0.921	1.501	1.499	1.623	1.272
		N	268.0	248.0	164.0	291.0	249.0	281.0
test	ctrl	median	3.629	2.099	3.197	6.937	4.808	4.396
		dev	1.778	1.254	1.772	4.285	4.707	3.436
		N	225.0	242.0	258.0	211.0	192.0	227.0
ctrl	ctrl	median	2.161	2.161	2.161	2.305	2.305	2.305
		dev	1.439	1.439	1.439	1.511	1.511	1.511
		N	245.0	245.0	245.0	202.0	202.0	202.0
KD index		value	**0.972**	**30.097**	1.934	**0.808**	2.448	2.466
		dev	**0.127**	**2.529**	0.208	**0.128**	0.285	0.267

immunoblot analysis. The T1, T2, and T3 constructs depleted approximately 93%, 91%, and 96% of Arp3, respectively.

Knockdown for each target was then evaluated using the combination pGSHIN-2 - pREFLECT-R fluorescence technique (Figure 57, Figure 61). To do this, separate plates of Rat2 cells were co-transfected with each of the 4 combinations of control and test expression and reporter vectors, fixed 48-72 hours later, and imaged. The control/test combinations used were: pGSHIN-2 control (lacking the hairpin cassette) + pREFLECT-R control (soluble DSred lacking the targeting sequence), pGSHIN-2 control + pREFLECT-R containing T1-T6, pGSHIN-2 containing T1-T6 + pREFLECT-R control, and pGSHIN-2 containing T1-T6 + pREFLECT-R containing T1-T6 (Figure 57A, B). A knockdown index for all 6 targets was calculated with Eric Brown (rotation student), and later repeated by Drs. Kojima and Danciu. By knockdown index calculations, the T1 and T4 constructs had depleted greater than 95% of the Arp3 protein on day 3 after transfection (Figure 57C). The T3, 5, and 6 constructs depleted approximately 90-95% of the total Arp3 protein. The T2 construct, designed to be a poor target, only depleted 60% of the Arp3 protein. The knockdown indices calculated for the functional targets (T1, T3-T6) was comparable to the depletion measured in the western blot analysis. It is unclear why the T2 target showed greater knockdown by immunoblot than by knockdown index.

Morphology of B16F1 melanoma cells lacking Arp3

Initial analysis of B16F1 melanoma cells depleted of Arp3 showed cells with decreased lamellipodia formation and increased edge actin bundles as evaluated by phalloidin staining (Figure 58). Cells transfected T4 showed the strongest phenotype. These cells showed reduced lamellipodia formation, and had sharp, bright phalloidin staining along the cell edges (Figure 58, lower panel, left) consistent with the appearance of edge actin bundles (Zand and Albrecht-Buehler, 1989). Cells transfected with the T5 and T6 targets also displayed bright phalloidin staining at the edges (Figure 58, lower panel center, right). These cells often produced lamellipodia, but they appeared much smaller than their non-transfected counterparts. These observations were qualitative, and were not quantified.

5.6 Discussion

Our kinetic-structural analysis of chick dorsal root ganglion growth cones revealed that a dendritic network, enriched with the actin nucleator Arp2/3, was present in protruding veils. These findings were consistent with the array-treadmilling model of lamellipodia protrusion described in fibroblasts (Svitkina and Borisy, 1999), and suggested a role for Arp2/3 in normal growth cone advance. However, the idea that neuronal process extension and growth cone advance could be driven by an Arp2/3 independent mechanism was raised in recent studies (Luo, 2002; Strasser et al., 2004). Two new families of actin nucleators (Quinlan et al., 2005; Zigmond, 2004) that nucleate straight actin filaments have been recently identified, and could potentially support this Arp2/3

Figure 58 Phalloidin staining of B16F1 depleted of Arp3.

Representative images acquired by Eric Brown (rotation student) in our laboratory showing non-transfected B16F1 melanoma cells stained with phalloidin (top panel), and B16F1 melanoma cells stained phalloidin and transfected with either the T4 (left), T5 (center), or T6 (right) target constructs, 5 days following transfection (bottom panel). Cells transfected with T4 have an angular appearance with increased staining of actin along the cell edges and decreased/absent lamellipodia when compared to non-transected cells. While still angular, cells transfected with the T5 and T6 constructs do form lamellipodia. Scale bar = 20 μm.

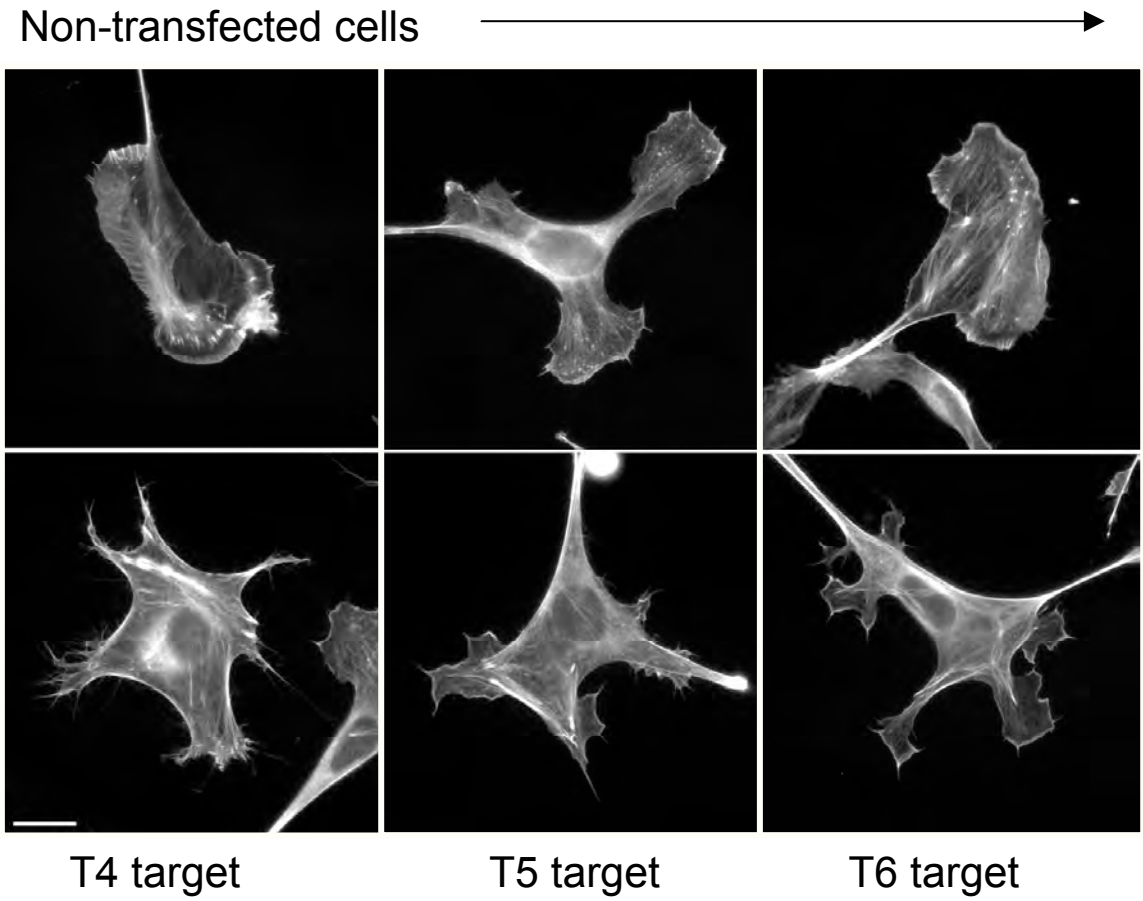

E. Brown

independent protrusion. Together, these findings indicated to us that the function of Arp2/3 in growth cone veil motility required a more thorough evaluation.

The results presented above document our experience evaluating the role of Arp2/3 using targeted depletion of the p34 and Arp3 subunits by short interfering RNA (siRNA). In the first approach, we generated two targeting reagents against the p34 subunit, which is located in the core of the Arp2/3 complex. The initial results looked promising, and we calculated a 70-90% reduction of p34 with the T1 construct, and an 85-90% reduction of p34 with the T2 construct in PC-12 cells. However, the mismatch control construct, which should have served as a control, also appeared to have some non-specific knockdown effect on p34 in FAC sorted cells, and on Arp3 and other cytoskeletal proteins in non- sorted cells. We were unable to determine the cause of this knockdown effect. In PC-12 cells, depletion of p34 was also accompanied by a significant reduction in process extension.

The inconsistencies encountered in both the immunoblots and process extension analyses in PC-12 cells, a cell line not previously used in our laboratory, led us to evaluate p34 knockdown in B16F1 melanoma cells. This cell line had been well characterized by the laboratory, and had displayed robust, consistent phenotypes in knockdown studies of fascin (Vignjevic et al., 2006) and capping protein (Mejillano et al., 2004) performed in the laboratory. The T2 construct reduced p34 protein levels by 82% in B16F1 melanoma cells, however, the T2* mismatch control construct also depleted ~32% of p34 compared to control. Additionally, a significant reduction in both lamellipodia formation and p34 immunostaining was observed with both constructs. .

However, similar to the PC-12 experiments, it was again noted that GFP (+) cells transfected with the T1 and T2 constructs that did form lamellipodia were indistinguishable from control cells. The inability to create a functional fluorescently tagged p34 rescue construct posed an additional challenge.

While a specific phenotype seemed to be indicated by the staining results, the immunoblots were not fully consistent in either cell line. In the end, the lack of uniform results by immunoblotting led us to question significance of the overall results, and led us to pursue knockdown of an alternate Arp2/3 subunit.

The Arp3 subunit was next chosen for depletion based upon the availability of functional fluorescent expression plasmid and the reported inability of active complex to form in its absence (Gournier et al., 2001). Six targets were selected against the Arp3 subunit: five of the targeting constructs were predicted to generate strong knockdown effect, while a sixth targeting construct, predicted to generate a very weak knockdown effect, was intentionally chosen as a positive control for a new system developed by the laboratory that would allow fluorescence-based evaluation of knockdown. Initial evaluation of knockdown by immunoblot indicated that all constructs, including the weak construct, depleted greater than 90% of Arp3, with 3 constructs depleting greater than 98% of Arp3. The knockdown index calculated by the fluorescence assay was comparable for all samples, with the exception of the weak target, which it found to deplete only ~60% of Arp3. Initial observations of B16F1 melanoma cells transfected with three of the strongest targets showed decreased lamellipodia formation

accompanied by the appearance of bright phalloidin stained bundles along the cell edges.

As we began to evaluate the knockdown phenotype of Arp3 depletion in B16F1 melanoma cells, Strasser et al. published their paper demonstrating growth cone advance in the presence of a dominant negative construct that inactivated Arp2/3 (2004). Such Arp2/3 independent protrusion could be understood in terms of the new actin nucleators described above. It could also possibly explain the presence PC-12 and B16F1 cells transfected with the knockdown vector but displaying normal phenotypes observed in our own experiments. However, they also reported that Arp2/3 was not enriched at the leading edge of neuronal veils in mouse hippocampal neurons, and was instead concentrated in the central domain of the growth cone (Strasser et al., 2004). Strasser supported the idea of an Arp-independent network by showing EMs of wild type hippocampal growth cones in which they observed few Y-junctions and a sparse actin network that did not resemble the dendritic meshwork found in fibroblast lamellipodia.

We found both the absence of the dendritic network and the Arp2/3 localization to be surprising. As my thesis project was based in the neuroscience program, it was decided at this point that I should evaluate Arp localization and actin organization in primary neurons, while further work characterizing the Arp3 knockdown reagent continued in the B16F1 cell line without me. Once a successful reagent was characterized in B16F1 melanoma cells, I would resume studies of process extension in PC-12 cells and primary neurons if feasible.

A consistent phenotype was not observed for any of the six Arp3 targets described above, leading Dr. Kojima to design additional targets against the Arp3 subunit. However, as of November 2006, a consistent phenotype had not been observed with these targets, either. The failure to generate a successful knockdown target for Arp2/3 with a consistent phenotype, despite three attempts targeting two separate subunits, remains puzzling. One explanation is that redundant pathways arising from the formin or spire families may support lamellipodia formation and veil protrusion when Arp2/3 levels are reduced. Another possible explanation is that while we were successful in knocking down capping protein by targeting only one of its two subunits, it may not be possible to completely disable a seven-subunit complex by targeting a single subunit and that partial complexes both form and possess nucleating ability *in vivo*, although such activity was not observed in vitro (Gournier et al., 2001). However, neither explanation can account for why only some Arp depleted cells appear normal, while the majority have a significantly altered morphology. The fact that several reports show that Arp depletion blocked lamellipodia and invadipodia formation (Harborth et al., 2001; Rogers et al., 2003; Yamaguchi et al., 2005), while others have reported continued motility (Di Nardo et al., 2005; Gupton et al., 2005; Ng and Luo, 2004; Strasser et al., 2004) suggests that the role of Arp2/3 in motility may be more complex than initially assumed.

CHAPTER 6

SUMMARY AND FUTURE DIRECTIONS

6.1 Summary.

The goal of this project was to evaluate the organization of the actin cytoskeleton and the function of the actin nucleator, Arp2/3, in motile growth cones. Structural-kinetic analyses were performed to correlate the actin cytoskeleton to the observed dynamic motility of neuronal growth cone veils. Immuno-staining, correlative immuno-electron microscopy, and expression of fluorescently tagged proteins was performed to localize cytoskeletal proteins within the growth cone. Finally, individual depletion of the p34 and Arp3 subunits of the Arp2/3 complex were pursued to dissect the role of Arp2/3 in the neuronal veils and lamellipodia. A summary of these results is provided below.

6.2 Structural-kinetic analysis of growth cone veil dynamics.

Neurons extend long processes and establish the wiring of the nervous system through the motility of the neuronal growth cone, which is located at the distal end of the axon. The growth cone is an actin and microtubule rich structure (Landis, 1983; Letourneau, 1996; Lewis and Bridgman, 1992), that projects smooth sheets and spikes, termed veils and filopodia respectively, at the light microscopic level. Rigorous studies of the actin cytoskeleton in motile fibroblasts had proposed an array treadmilling model of a dendritic actin network to describe protrusive motility in the lamellipodia (Borisy and Svitkina, 2000; Svitkina and Borisy, 1999); another sheet-like actin based protrusive organelle originally described by Abercrombie (Abercrombie et al., 1970; Abercrombie et al., 1971). This model relied upon the actin nucleator Arp2/3, a seven protein

complex, to create branches off the sides of pre-existing straight actin filaments. However, considerable debate over the organization of the cytoskeleton in the growth cone existed in the literature, and the equivalence of veils and lamellipodia was difficult to evaluate (Svitkina and Borisy, 1999). Additionally, studies showing growth cone advance in the absence of Arp2/3 (Ng and Luo, 2004; Strasser et al., 2004) along with the discovery of new families actin nucleators (Baum and Kunda, 2005; Kovar, 2006; Quinlan et al., 2005; Zigmond, 2004) raised further questions about the mechanism of protrusive motility in the growth cone. These uncertainties led us to perform structural kinetic analysis of growth cone veil dynamics using correlative light and electron microscopy to further evaluate the ultrastructure of motile neuronal veils under normal conditions.

Our analysis found that neuronal veil protrusion was associated with a dendritic network similar to that seen in motile fibroblasts. Immuno-localization of Arp2/3 and expression of a tagged Arp subunit showed that Arp2/3 was associated with this dendritic network. From this we concluded that the array treadmilling model of protrusion, similar to that characterized in motile fibroblasts, functioned in normal neuronal veil protrusion.

In addition to protrusion, we also characterized veil retraction, and presented the first report of the ultrastructure associated with retraction. Retracting veils almost always had a concave shape did not contain a dendritic network. Instead, bundled actin filaments oriented parallel to the membrane edge were seen in place of the dendritic network. Beyond the bundled filaments, the actin network was extremely sparse – even

after only a few seconds of retraction. We concluded that the absence of filaments, while striking, was consistent with the array treadmilling model, and would be expected if actin polymerization were turned off.

Finally, we showed that veils predominantly protruded in association with one or two filopodia, and that the filopodia served as boundaries that supported independent veil motility on both sides. Veils protruded rapidly, and new veils could form from the crotch of two pre-existing filopodia in less than 6 seconds. We also presented the novel finding that veils could be initiated de novo from filopodia shafts. These findings led us to expand the convergent elongation model, in which filopodia interact with the dendritic network from which they arise, to include new interactions with dendritic networks which they initiate.

Overall, the results suggest that complex dynamics exist between neuronal veils and filopodia that allow a great diversity of form to be created from the basic structural units of the actin cytoskeleton. This flexibility of form, the independence of motility, and the rapidity of initiation and disassembly allow growth cones to efficiently explore their environment and proceed rapidly down the chosen path.

6.3 Ancillary findings resulting from the CorEM studies.

These ancillary findings were seen during the course of our CorEM studies, and fell outside the scope of the published paper. We observed that filopodia interacted with each other in a more complex fashion than previously observed in melanoma cells. We observed that most protruding filopodia had a tip complex structure, similar to that

reported previously (Lewis and Bridgman, 1992; Svitkina et al., 2003), but that few retracting or stalled filopodia, and those located along the axon shaft, lacked this structure. Filopodia located along the axon shaft also tended to be more highly branched than those found in the growth cone. These observations suggest that neuronal filopodia may contain structural and functional characteristics that vary in a distinct fashion when compared to their counterparts studied in motile fibroblasts.

Initial immunostaining of myosin IIA in DRGs showed that it was enriched in regions of low actin density, and decreased in regions of high actin density. Immunogold labeling showed that myosin localized to actin bundles along concave membrane edges, but was restricted from dendritic networks, suggesting a role for myosin IIA in veil retraction.

Correlative rhodamine actin incorporation showed that the distribution of barbed ends in DRG growth cones was highest in regions of veil protrusion, and low in regions of veil retraction. Regions that converted from retraction to protrusion had increased incorporation, while regions of longstanding veil retraction showed little actin incorporation. We took this to suggest that DRGs maintain tight control over barbed end distribution in a manner similar to that observed in fibroblasts.

Phosphotyrosine immunostaining in melanoma cells in the laboratory showed exclusion of staining from the shafts of filopodia (Schober et al., 2007). As this was in conflict with published literature in growth cone filopodia (Steketee and Tosney, 2002) , we repeated the staining in DRGs for comparison. We did see staining along the shafts of filopodia, including those with associated veils, which is in contrast to reports by

Steketee that showed exclusion of staining in filopodia associated with veils. This suggests there neuronal filopodia may have properties that differ from melanoma filopodia.

Taken together, these findings represent important observations that may form foundations for future studies.

6.4 Depletion of Arp2/3 subunits resulted in an inconsistent phenotype.

We localized Arp2/3 subunits to the leading edge of growth cone veils in PC-12 cells using immunofluorescent staining and live cell imaging with GFP tagged Arp3. We initially targeted p34, a critical Arp2/3 subunit close to the core of the complex. By immunoblot, we achieved 75-90% depletion of the p34 protein in PC-12 cells at 96 hours, and 80% depletion of p34 in B16F1 melanoma cells at 120 hours. However, cells transfected with our mismatch control construct also showed ~33% reduction of p34 as well as a reduction in other Arp2/3 subunits and other cytoskeletal proteins.

PC-12 cells depleted of p34 had a significant reduction in process extension. However, the cells that did extend processes were indistinguishable from non-transfected cells. B16F1 melanoma cells depleted of p34 showed significantly reduced lamellipodia formation and p34 immunostaining, but cells that could form lamellipodia were again indistinguishable from wild type. We hypothesized that the inconsistent phenotype could have resulted from an insufficient depletion of the protein, the formation of small amounts of active complex without the p34 subunit, or by redundant pathways offered by other actin nucleators. However, these inconsistencies combined

with the inability to create a rescue construct led us to focus on depletion of an alternate Arp2/3 subunit, Arp3.

We generated six new targets against Arp3, including one that was designed to be ineffective, using a vector-based system that allowed optical quantification of depletion. 2/6 targets achieved > 95% knockdown, 3/6 achieved > 90% knockdown, and the ineffective target achieved only 60% knockdown by immunoblot. The initial studies showed a more consistent phenotype, with reduced lamellipodia formation, in B16F1 melanoma cells than that seen with p34 depletion. However, a proportion of transfected cells continued to appear indistinguishable from non-transfected cells. The persistence of normal cells transfected with our targeting constructs made it difficult for us to draw any firm conclusions about the role of Arp2/3 in lamellipodia formation from these results. These results indicate that we may need to simultaneously deplete more than one subunit, or target an alternate subunit(s), to fully inactivate Arp2/3 and evaluate its role in veil motility and ultrastructure organization. Additionally, Arp2/3 independent pathways that support actin-based protrusion should be evaluated.

6.5 Future Directions

The work summarized above contains unanswered questions which themselves point towards future investigations.

6.6 Arp2/3 knockdown in primary neurons, neuronal cell lines, and in vivo.

We have shown the presence of Arp2/3 in protruding neuronal veils. However, the precise role of Arp2/3 in the neuronal growth cone, and whether Arp2/3 is essential for motility remains unanswered. These questions remain critical to the field of cellular neurobiology. Without a clear understanding of the contribution of Arp2/3, and potentially other actin nucleators, to the organization of the cytoskeletal machinery in neuronal veils, it becomes difficult to evaluate the mechanisms by which upstream signaling molecules and environmental cues influence growth cone advance and pathfinding.

We attempted to address the role of Arp2/3 with our targeted depletion of the p34 and Arp3 subunits. However, the results were inconsistent and precluded us from drawing strong conclusions about the role of Arp2/3 in the growth cone advance. The lab has since created a third set of targeting constructs, but these also displayed an inconsistent phenotype. Perhaps, targeting only one of the seven proteins may not be sufficient to achieve complete inactivation of the Arp2/3 complex. There are reports in the literature that suggest that two mutations in separate subunits that were individually mild or without phenotype, once combined, resulted in a severe phenotype (Zallen et al., 2002). That result suggests that simultaneous knockdowns of more than one subunit may be necessary to completely inactivate Arp2/3. It may also be necessary to target subunits in the Arp2/3 complex other than p34 and Arp3. . From this we may infer that there is some redundancy within the system that allows normal morphology to persist, but we do not know the location of this redundancy.

In addition to the challenge of creating a successful reagent to target Arp2/3, there are still technical difficulties to knocking down proteins in primary neurons that we need to resolve. The most significant of these challenges is that we have no technique to halt process extension during the period of protein depletion (3-5 days). In the meantime, we can evaluate reagents in easier to manipulate systems such as PC-12 or B16F1 melanoma.

An alternate route would be to transfect either individual neurons or small regions of one side of the chick brain or dorsal root ganglion with the Arp2/3 knockdown reagent or Arp3 GFP using the Cline Lab technique for targeted in vivo electroporation (Bestman et al., 2006; Haas et al., 2002). This would allow us to directly study the role of Apr2/3 in neuronal pathfinding in an intact animal, and determine the contribution of Arp2/3 to normal growth cone pathfinding.

6.7 Evaluation of other actin nucleators in neuronal veil motility and ultrastructure.

Reports in non-neuronal cells have shown that Arp2/3 depletion blocked lamellipodia and invadipodia formation (Harborth et al., 2001; Rogers et al., 2003; Yamaguchi et al., 2005). Our own preliminary studies also showed that Arp2/3 depletion reduced process extension and decreased lamellipodia formation. However, two studies in the neuronal literature (Luo, 2002; Strasser et al., 2004), and others in the non-neuronal literature. (Di Nardo et al., 2005; Gupton et al., 2005) have reported continued motility in the absence of Arp2/3, suggesting that Arp2/3 independent mechanisms for protrusion exist.

Two potential candidates that may support Arp2/3 independent protrusive motility are spire and formin families, which represent two recently discovered actin nucleators (Evangelista et al., 2003; Quinlan et al., 2005). Specifically, future studies should be conducted to evaluate their individual contributions to the organization of actin filaments in the dendritic network and their role in protrusive motility of neuronal veils. The first steps would include localization via immunofluorescent staining and live cell imaging with fluorescently tagged proteins in the growth cone. This would be would followed by targeted depletion of these proteins along with morphometric and structural-kinetic analysis of knockdown cells. We hypothesize that the combined results of formin, spire, and Arp2/3 knockdowns will help us to create a more accurate model of veil motility in the growth cone. As discussed above, any targets created would be evaluated in neuronal and non-neuronal tissue culture lines, before proceeding in primary neurons and in vivo experiments.

6.8 Fascin depletion should be performed to evaluate the role of neuronal filopodia in growth cone motility, veil organization, and path-finding.

The structural-kinetic analysis of veil dynamics revealed that the majority of veil protrusion was associated with filopodia, and suggested that novel interactions between veils and filopodia exist in neuronal cells. As fascin is the primary bundler of actin filaments in filopodia (Vignjevic et al., 2006), the role of fascin in growth cone motility should be carefully evaluated. The fascin siRNA constructs already available in the lab have been shown to deplete melanoma cell of filopodia very effectively (Vignjevic et al.,

2006). Correlative microscopy of the veil in the absence of numerous filopodia would allow us to evaluate the dependence of neuronal veil organization on filopodia. Turning and outgrowth assays would allow us to evaluate the role of fascin neuronal path-finding.

6.9 CorEM of myosin II in neuronal growth cones.

We observed that retracting veils had bundled actin filaments that ran parallel to the membrane edge in place of a dendritic network. In keratocytes, myosin II has been shown to generate bundled actin filaments at the rear of the lamellipodium (Svitkina et al., 1997) that appear similar to the edge bundles observed in the retracting veils. Myosin II is present in growth cones (Bridgman, 2002), has been associated with retrograde flow (Brown and Bridgman, 2003b), and is implicated in growth cone(Brown and Bridgman, 2003a; Diefenbach et al., 2002; Medeiros et al., 2006) retraction. A recent computer model based on myosin inhibition in neurons showed that myosin contraction, when distributed within a dendritic network with filopodia, can lead to concave membrane shapes and possibly induce further filopodia formation (Shlomovitz and Gov, 2007). Our preliminary staining for myosin II showed enrichment on bundled edge filaments, with much lower staining in dendritic networks. Thus potential role for myosin in generating the observed bundles and concave shape is suggested and should be further evaluated. CorEM studies with immunoelectron staining should be performed to localize mysosin IIA to retracting veils. Alternatively, myosin II knockout animals have been generated (Conti et al., 2004; Tullio et al., 2001), and neurons

derived from these animals could be studied using CorEM to evaluate the role of myosin in veil retraction and ultrastructure.

CHAPTER 7

MATERIALS AND METHODS

7.1 Tissue & Cell culture.

Rat pheochromocytoma cells (PC-12).

Cells were obtained from ATCC [ATCC # CRL-1721] and were cultured in Dulbelcco's modified eagle medium (DMEM) supplemented with 10% Horse serum (HS), 5% Fetal bovine serum (FBS), 1:100 Penicillin Streptomycin, 1:100 Sodium Pyruvate. For fluorescence and EM experiments, cells are plated onto glass cover slips coated with poly-D/L-ornithine, followed by 20mg/mL mouse laminin (Invitrogen). For live cell imaging, cells were transferred into L-15 medium (Gibco) before observation. Process extension was elicited by transferring cells into DMEM supplemented with 5% FBS and 50-100ng/mL 2.5S mouse NGF.

Mouse/Rat Neuroblastoma cells (NG108).

Undifferentiated cells were cultured in Dulbelcco's modified eagle medium (DMEM) supplemented with 10% Fetal bovine serum (FBS), 1:100 Penicillin Streptomycin, and 1X HAT (hypoxanthine). To differentiate the cells into extending processes, they were replated in DMEM, 1:100 Penicillin Streptomycin, and 0.1X HAT (hypoxanthine). For fluorescence and EM experiments, cells are plated onto glass cover slips coated with poly-D/L-ornithine, followed by 20mg/mL mouse laminin (Invitrogen). For live cell imaging, cells were transferred into L-15 medium (Gibco) before observation.

B16F1 mouse melanoma cells.

Cells were cultured in Dulbelcco's modified eagle medium (DMEM) supplemented with 10% Fetal bovine serum (FBS), 1:100 Penicillin Streptomycin. For fluorescence and EM experiments, cells were plated onto glass cover slips coated with 20mg/mL mouse laminin (Invitrogen), followed by 1% sterile filtered BSA in DPBS. For live cell imaging, cells were transferred into L-15 medium (Gibco) before observation.

Chicken dorsal root ganglion neurons (DRG):

Whole chicken DRGs were isolated from E7-E9 chick embryos as described in (Smith, 1998). Briefly, whole DRG explants were cultured in D-MEM/F-12 (Invitrogen; 11039-021) with 15 mM HEPES buffer, L-glutamine, and pyridoxine HCl; without phenol red and pyridoxal HCl base media supplemented with: 1 mg/ml bovine serum albumin fraction V powder (Sigma; A-9647), 5 µg/mL crystalline bovine pancreas insulin (Sigma; I-6634), 0.025 µL sodium selenite (Sigma; S-9133), 10 µg/mL chick transferrin (Intercell Technology; F-811), and 5-10 ng/mL 7s-NGF (Sigma). DRG explants were plated on ethanol cleaned glass coverslips or glass bottom imaging dishes coated with poly-D/L-ornithine or poly-D-Lysine overnight, followed by 20mg/mL mouse laminin (Invitrogen) for 2-4 hours. Dissociated sensory neuron cultures from DRGs were isolated by incubation in 4 mL 5X trypsin EDTA in PBS at 37˚C for 30 minutes, followed by trypsin inactivation by incubation in 5% horse serum in PBS, and finally by trituration through a fire-polished glass Pasteur pipet until the DRGs were dissociated to the eye (5-6X).

7.2 Immunofluorescent staining of fixed cells:

Before staining, the cells are usually extracted to expose the cytoskeleton and corresponding epitopes and are fixed (order of extraction/fixation can be modified to accommodate different antibodies). Extraction with a strong non-ionizing detergent (1% Triton-X) solubilizes the cell membrane rapidly, and stabilizers such as phalloidin (to stabilize actin specifically) and high molecular weight polyethyleneglycol (PEG) in PEM buffer help stabilize the cytoskeleton and prevent artifact. Briefly, culture media is removed from the dish and cells are rinsed with PBS to remove serum. Cells are extracted by incubating for 3-5 minutes at room temperature in extraction buffer and then rinsed two times in PBS for 5 minutes. Extraction buffer contains: 1% Triton-X, 4% PEG MW 40,000 (SERVA), 10μM phalloidin, and 10 μm taxol in PEM buffer (100 mM PIPES, ph 6.9; 1 mM MgCl2; 1 mM EGTA). Fixation method is determined by the intrinsic properties of each primary antibody. Glutaraldehyde, formaldehyde, and methanol fixation are routinely used in the lab:

1. Glutaraldehyde Fixation (many lab antibodies): 0.2% glutaraldehyde made in 0.1M cacodylic acetate, quench two times in 2mg/mL sodium borohydrate for 10 minutes to reduce background auto-fluorescence.
2. Formaldehyde Fixation (p34 – upstate): 4% formaldehyde in PBS for 30 minutes at room temperature
3. Methanol Fixation (Fascin): 100% methanol cooled to –20˚C for 10 minutes in –20˚C freezer (used for samples that must be denatured to allow binding of antibody to the epitope)

4. Alternatively, for a few primary antibodies the extraction step was omitted for simultaneous extraction and fixation (0.5% Triton-X 100 and 0.2% glutaraldehyde in 0.1M cacodylic acid) or fixation by para-formaldehyde with post-extraction in 1% Triton-X 100 in PBS for 3 minutes.

7.3 Antibodies used.

Commercial Primary antibodies.

Anti-p34 (Upstate Biotech), Anti-Arp3 (Upstate Biotech), Anti-tubulin-α (Sigma), Anti-fascin (DAKO), Anti-cofilin, Anti-actin. Anti-myosin IIA (Sigma), Anti-phosphotyrosine, (Sigma),

Borisy Lab generated primary antibodies.

(peptide-derived, rabbit polyclonal made by John Peloquin): Anti-p16, Anti-CPα 498 (used for immunoblots),

Gift Primary Antibodies.

p33A (anti-p34) - Laura Machesky, R22 (anti-CP pan ß), Anti-CP-α, and R26 (anti-CP ß2) - Dr. Dorothy Schafer, Anti-VASP – Dr. Frank Gertler.

Secondary Antibodies.

All secondary antibodies for immunofluorescence and immunoblotting are obtained from Jackson Laboratories or Sigma.

7.4 Microscopy.

Light Microscopy

Light and fluorescence microscopy were performed using an inverted microscope (Diaphot 300; Nikon) equipped with Plan, 63X objective, and (TMD) 10X objectives and a back illuminated, cooled CCD camera (model CH250, Roper Scientific) or a slow-scan cooled CCD camera (model CH350, Photometrics) driven by MetaMorph Imaging software (Universal Imaging Corp). For live cell imaging, cells were kept at 36-37˚C by means of an objective heating system. For overnight imaging, the media in culture dishes was overlayered with mineral oil to reduce evaporation. Filter cubes and filter wheel sets were used for fluorescence imaging.

Correlative light and electron microscopy (+/- immunoelectron staining).

Samples for platinum replica electron microscopy were prepared as described in Svitkina and Borisy, 1998. Briefly, whole DRG explants were plated onto gold, poly-D-Lysine, and laminin coated grid-finder coverslips attached via vacuum grease to plastic imaging dishes with a hole bored in the bottom. Explants were allowed to grow for ~24 hours before imaging with a 60X heated objective on a Nikon Diaphot 300 microscope with motorized stage. Phase contrast images of the selected growth cone(s) were acquired every 2-3 seconds for 30 seconds to 3 minutes, until the growth cone appeared in a stable state of well attached protrusion. Culture media was vacuum aspirated and extraction solution (1% Triton X-100, 4% PEG (MW 40,000) (Serva, Heidelberg / New York)) in buffer PEM supplemented with 10 µg/ml taxol and 10 µM

Figure 59 Correlative Light and Electron Microscopy Technique

A. An imaging dish is constructed by attaching a coverslip with a gold-coated locator grid to the bottom of a 35 mm plastic imaging dish via vacuum grease. B. Hi magnification of locater grid. C. Individual growth cones are imaged for 1 – 10 minutes D. While imaging continues, media is aspirated from the dish and exchanged for extraction solution. Fixation with glutaraldehyde is performed following removal of extraction solution, and rinsing with PBS. E. A platinum replica is of the growth cone is created, mounted onto an EM grid, and imaged. F. From there, a region of interest can be identified, and its motility at the point of extraction can be reconstructed by merging the lysed and final live images from the image sequence.

Correlative Light & Electron Microscopy

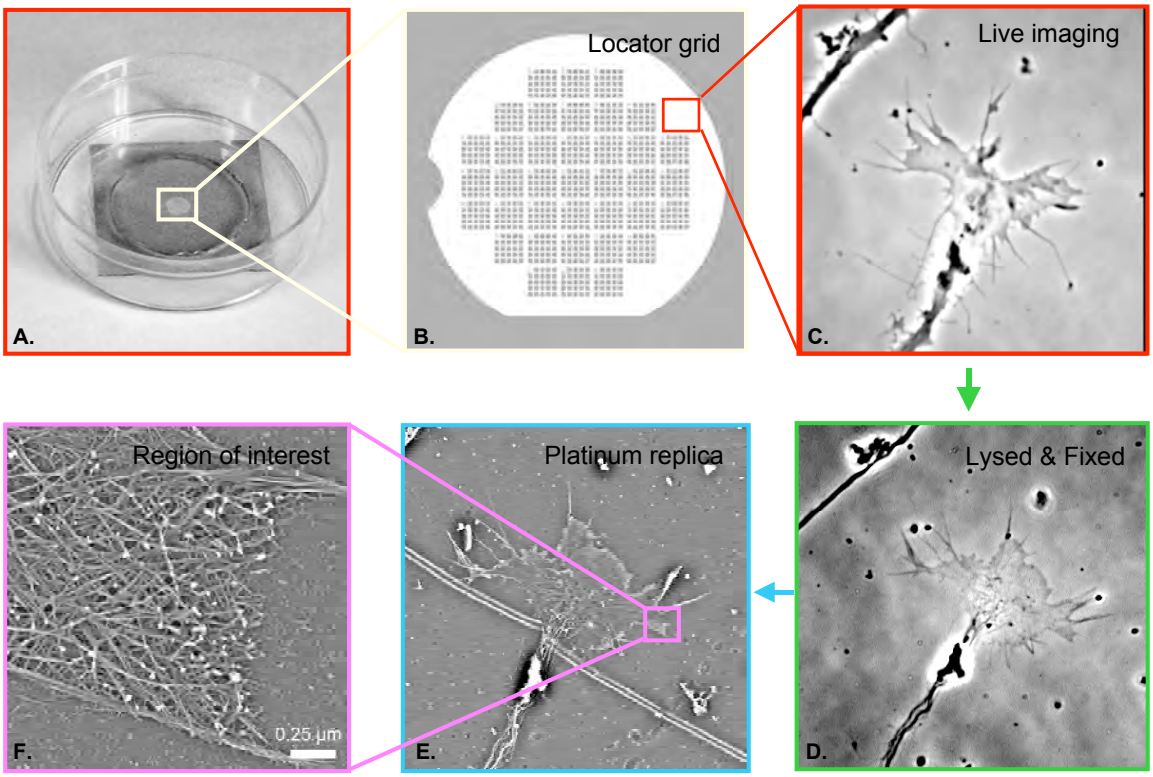

phalloidin) was immediately added while imaging continued. Phase contrast images were obscured for approximately 4-6 seconds during this process. Extraction solution was aspirated after 4 minutes, the dish was rinsed 2X in buffer PEM, and then the sample was incubated with 2% glutaraldehyde in 0.1M cacodylic acid for 20 minutes to fix the cytoskeleton.

At this point, some samples were stained for filamentous actin by a 10 minute incubation with 1:100-200 dilution of fluorescently labeled phalloidin in PBS. To prevent photodamage to the cytoskeleton prior to visualization in the EM, fluorescent imaging was minimized,--generally no more than 2-3 fluorescent images were acquired with short exposure time (~100 ms). Samples were prepared for immunoEM localization of biomarkers as follows: fixed cytoskeletal preparations were quenched by applying 2 mg/mL sodium borohydride ($NaBH_4$) in PBS (2X, 10 minutes each) at room temperature. Dishes were rinsed in PBS (3X, 5 min), PBS was removed, and coverslips were wiped around the central finder grid to allow primary antibody application in PBS (Arp3, 1:10), and incubated 30-45 min at room temperature. After rinsing in PBS (3X, 5 min), coverslips were rinsed 1X with buffer A (20 mM Tris-HCl, pH 8.0, 0.5 M NaCl, 0.05% Tween 20) containing 0.1% BSA, and coverslips were again wiped around the central finder grid before applying secondary gold-conjugated antibody in Buffer A with 1.0% BSA, overnight at room temperature in a moist sealed dish. Dishes were rinsed in buffer A containing 0.1% BSA (3 X, 5 min) and fixed again in 2% glutaraldehyde in 0.1M cacodylic acid for 20 minutes.

Without washing, glutaraldehyde was removed, 0.1% tannic acid solution was added (Mallinckrodt, Inc., Paris, Kentucky; Cat. # 1764) and dishes were incubated for 20 min at room temperature. Specimens were rinsed in water (3X, 5 min). 0.1-0.2% aqueous uranyl acetate solution was added and samples were incubated for 20 min at room temperature. Dishes were rinsed with distilled water and then samples were dehydrated through 5 min incubations in graded ethanols (10%, 20%, 40%, 60%, 80%, and two times 100%, 5 min in each). Dishes were incubated in 0.1-0.2% uranyl acetate in 100% ethanol for 20 min, then washed 2X in 100% ethanol and 2X in 100% ethanol dried over molecular sieves, 5 min in each. Samples were placed in the critical point dryer and ethanol was substituted with liquid CO2 at 5-10˚C by 10 exchanges for 5 min each. Samples were then placed in a vacuum evaporator and shadowed with 2-2.8 nm platinum, followed by carbon evaporation coating of 2-3 nm. Individual samples were located under the microscope and mounted on EM grids for observation.

Correlative light, fluorescence, and EM with Rhodamine-actin Incorporation Assay.

Cells were imaged and extracted as above. Following extraction, the samples were rinsed 1X in PEM buffer, followed by 1X in P buffer. The samples were then incubated in 0.4-0.5 µm freshly dialyzed rhodamine-actin in P buffer containing 1 mM ATP for 4 minutes on the stage [rhodamine-conjugated actin was prepared by John Peloquin]. Rinse 2X with P Buffer, incubate 20 minutes with 0.2% glutaraldehyde in 0.1M cacodylic acid. Fluorescent images were acquired, glutaraldehyde removed, and the samples

were then incubated with 1:100 Alexa 488 conjugated phalloidin in DPBS for 10 minutes on the stage (phalloidin does not bind to rhodamine labeled actin). Samples were rinsed 2X in PBS, fluorescent images acquired, followed by fixation and processing for platinum replica microscopy as described above. Rhodamine derivatized actin was prepared by John Peloquin, and purified with help from Yvonne Aratyn.

7.5 Growth Cone Tracking, Kymography, and Linescan Analyses

Low magnification (10X, phase contrast objective) time-lapse movies were made to track axonal outgrowth. Images were acquired every 3 minutes over 3-8 hours. Growth cone translocation tracks were obtained by recording the location of the center of the growth cone in each frame of the image sequence using NIH Image J software (Abramoff et al., 2004). Instantaneous velocities were calculated from differences in growth cone position in successive frames. Persistence of translocation over a 1 hr period was calculated as the ratio of the straight line distance between start and end points and the actual path distance obtained by summing the distances between every pair of successive frames.

For kymography, phase-contrast time-lapse sequences were obtained on a Nikon Diaphot 300 microscope using a 63x objective. Movies were 2 min to 8 hours long with frames taken every 2-3 seconds for shorter movies and every 3 minutes for sequences longer than 15 minutes. Kymographs were produced using the NIH ImageJ software ‘kymograph’ function after the image sequence was first processed with the ‘enhance contrast’ function to maximize the contrast of the veil edge against the

background (Abramoff et al., 2004). A 1-pixel-wide path was drawn perpendicular to the direction of veil protrusion or retraction (x axis, measured in μm). Time is measured along the y axis in seconds, with 2-3 seconds between each line depending on acquisition rate of the specific timelapse. Slopes of these lines were used to calculate the velocities, and projections of these lines along the x axis (time) were used to calculate the duration of protrusions essentially as described (Hinz et al., 1999). The direction of veil protrusion was represented in text figures by color merging successive frames,--either by merging two live frames or by merging the lysed and last live frames of the image sequence. In all cases, the later image was put in the red channel and the earlier image in the blue and green channels. Merging the images thus resulted in color coding of protruding domains as red and retracting domains as cyan.

Linescan analyses of actin intensity were performed using the NIH ImageJ software, “plot profile” function, using a 3 to 7 pixel wide line on phalloidin stained growth cones. Values were normalized to obtain relative intensities.

7.6 Statistics

Significance was determined using a two-tailed Student’s t-test, p values are given in the text, p values less than 0.05 were considered significant.

7.7 Transient expression of proteins and siRNA hairpin constructs.

PC-12 cells.

Cells were pelleted in a clinical centrifuge, culture media was aspirated, and cells were re-suspended in 250 µL transfection media (50 mL culture media with 350 µL 1M Hepes buffer, pH 7.1). A mixture containing 7µL sheared/denatured salmon sperm DNA (20 mg/mL) (Amresco), 12 µL ddH_2O, and 7 µL experimental vector (1 µg/µL) was added to cells, and mixture was transferred to electroporation cuvette (BTX640). Electroporation was performed on a Biorad Gene Pulser Xcell at 960 V, 250 µF resistance. I routinely achieved 70-90% transfection efficiency using this technique.

B16F1 and NG108 cells.

Transient expression of proteins and shRNA was performed with FuGENE6 (Roche) according to manufacturer's recommendations.

Chick Dorsal Root Ganglion neurons (DRG).

Nucleofection is a term coined by Amaxa Biosystems, and refers to a proprietary technique that combines lipofection and electroporation, in a species and cell type specific fashion. Dissociated sensory neurons were isolated as described above. Neurons were pelleted in 5% horse serum by spinning for 5 minutes at 100XG in a benchtop centrifuge (Greg Smith lab). The media was aspirated, and the cells were resuspended in 100 µL Amaxa chicken neuron transfection solution. 5µg of endotoxin-free maxi prepped DNA was immediately added, and the entire mixture was transferred to the nucleofection cuvette. Cells were nucleofected on setting "O-03". 1 mL of pre-warmed culture media was added to the cuvette following nucleofection, and the entire

mixture was transferred to imaging dishes or wells containing media and coated coverslips. Cells were imaged 24-96 hours after plating, GFP expression was first noted at approximately 24 hours after nucleofection.

7.8 Immunoblotting:

Cells were collected by pelleting the contents of a 90% confluent 100 mm plate of PC-12 cells on a clinical centrifuge at 1800 rpm for 5 minutes. Culture media was aspirated and cells were re-suspended in 2 mL ice cold PBS (GIBCO) and re-pelleted. PBS is aspirated and cells are then re-suspended into lysis buffer containing 10mM Tris pH 7.5, 150 mM NaCl, 1% Triton-X 100, 10% glycerol, and protease inhibitor table (Roche). Lysates were incubated on ice for 10 minutes, and the lysate was then cleared by centrifugation for 15 minutes at 14,000 rpm at 4˚C. 4X sample buffer was added to supernatants, samples were boiled for 5 minutes at 100˚C, and were loaded onto a gel. Protein concentration was determined using BCA reagent (Pierce) to ensure equal loading of gel lanes. SDS-Page electrophoresis and immunoblotting onto PVDF was performed according to standard protocols. All samples were loaded in duplicate at the minimum, samples were frequently loaded in triplicate. All knockdown results represent a minimum of three separate experiments performed at separate times.

7.9 Densitometry and quantification of protein depletion

Blots were first probed with antibodies against the targeted protein, followed by other Arp subunits and/or cytoskeletal proteins such as capping protein, fascin, cortactin, and VASP. Tubulin staining for loading control was performed last. The antibody was very sensitive and provided an extremely strong signal that was difficult to strip. Densitometry analysis was performed on the scanned films (300 dpi, 8 bit grayscale) using NIH Image 1.6.3 software. To perform the densitometry, a box was drawn around the largest band on the film. The integrated density within the box was measured, as well as in a box directly below the band (background). This was repeated for all bands on the gel. The integrated density of the tubulin bands was measured as above. The background density was subtracted from each band. The amount of targeted protein remaining in the depleted cells was calculated as the density of the targeted protein in transfected cells (E), corrected for transfection efficiency/cell purity, divided by the density of the targeted protein in the sham transfected cells (C), corrected for tubulin loading using the following formula:

$$\frac{\text{Density target (E)} - \left\{\text{Density target (C)} \times \left(\frac{\text{Density Tubulin (E)}}{\text{Density Tubulin (C)}}\right) \times \text{\% NON-transfected cells}\right\}}{\text{Density target (C)} \times \left(\frac{\text{Density Tubulin (E)}}{\text{Density Tubulin (C)}}\right)}$$

To more accurately quantify knockdown, later studies used 8 control samples, spanning a 50-fold range of protein concentration from 0.1 to 5 µg. The integrated densities were

plotted, and the slope obtained and used to determine the amount of protein remaining in the experimental samples. Values were then adjusted for transfection efficiency as above

7.10 Fluorescence Activated Cell Sorting (FACS).

In order to quantify the level of protein knockdown, a relatively pure population of transfected cells was needed. Electroporation was used for transfection of the PC-12 cells, and yielded a variable population of transfected cells, normally reaching 65-90%, sometimes higher. Lipofection, using FuGene6, in B16F1 melanoma and NG108 neuroblastoma resulted in approximately 30% transfection rate. FACS was employed to further purify the population of transfected cells. This technique worked effectively for B16F1 melanoma cells. However, in PC-12 cells, loss of a large percentage of sorted cells to apoptosis following sorting, despite numerous attempts to refine the sorting protocol, limited its utility. For all cell lines, the percentage of transfected cells was determined directly prior collecting the cells to prepare lysate.

7.11 Molecular Biology

Vector Construction.

Vector construction was accomplished as follows – certain si/shRNA plasmids are described in greater detail in separate sections.

p34 constructs: pcDNA3.1(+) p34 rescue vector: constructed by A. Mongiu. p34 human cDNA in pBluescript SK- was a gift from Dr. Matt Welch (A006085). The p34

insert was excised and sub cloned into pcDNA3.1(+) mammalian expression vector (Invitrogen), **p34-pIRES-GFP**.

Arp3-GFP constructs: human Arp3, gift of Dr. Matt Welch, **Arp3-mRFP** constructed by A. Mongiu, Arp 3 was excised and sub cloned into pmRFP (gift of Roger Tsien), **Arp3-paGFP,** constructed by A. Mongiu**,** Arp 3 was excised and sub cloned into paGFP, **Arp3 Venus,** constructed by KT**.**

pEGFP-actin: sub-cloned into pECFP and YFP (Clontech) for pECFP/YFP-actin by A. Mongiu,

p34 siRNA targeting vectors: pG-Super T1, and T2: constructed by A. Mongiu/AK as described in greater detail below. **p34 pG-Super T2*H and T2*NH mismatch control vectors:** constructed by A. Mongiu/JM. T2*H is homologous to the human gene, and will target the rescue vector. T2*NH does not target the rescue vector. **p34 pG-Super T2*MLA** contained an experimental modification to the hairpin loop region. All p34 constructs were sub-cloned into **pDsRed-Super** by A. Mongiu.

Arp3 siRNA targeting vectors: pG-SHIN2 T1, T2, T3, T4, T5, and T6 shRNA and p-Reflect-R T1, T2, T3, T4, T5, and T6 vectors, constructed by A. Mongiu, **pG-SHIN2 T1* and T4*** mismatch controls, constructed by D. Applewhite.

pGSuper vector.

pGSuper is derived from the pSuper construct (Brummelkamp et al., 2002) that expresses a hairpin siRNA with an added soluble GFP marker under a separate promoter to allow identification of cells transfected with the plasmid (Kojima et al., 2004)

(Figure 60A). Briefly, 19 nucleotide target sequences to the gene of interest are chosen, and forward and reverse 64-mer oligonucleotides are designed based on framing the target sequence and its complementary sequence into a template containing the appropriate ends and hairpin sequence (Brummelkamp et al., 2002). The criteria used for selecting the 19 nucleotide target sequence include: the nucleotides "AA" immediately preceding the sequence, a 40-60% G/C content, and homology only to the target gene as determined by genomic BLAST (NCBI) of the appropriate database. Sequences that are mismatched by less than two nucleotides to other genomic DNA are not selected. The synthesized oligos (Sigma Genosys) are annealed, phosphorylated, and then ligated into the empty pGSuper vector.

pC-Super and pDSRed-Super construct:

A modification of pGSuper, obtained by removing the GFP and exchanging it with CFP obtained from pECFP vector (Clontech) or DsRed.

pG-SHIN-2 and pReflect-R:

pG-2SHIN and pReflect-R represent the second generation of shRNA vectors from our laboratory. The vectors comprise a two part system that was designed to allow optical evaluation of shRNA driven protein depletion. pG-SHIN-2 (Small Hairpin Interfering Nucleotides) is similar to the pG-Super vector referenced above pGSHIN can be co-transfected with another laboratory vector designed by Dr. Kojima, pReflect-R (RNAi Evaluation by Fluorescence Level from Expressed Carrier of Target) to rapidly evaluate

Figure 60 pGSuper Plasmid and pGSHIN, p-Reflect siRNA vectors.

A. The pGSuper plasmid is a modification of the pSuper siRNA plasmid (Brummelkamp et al., 2002) . The addition of a soluble **G**FP marker driven under separate promoter allows easy visual/automated identification of cells transfected with the plasmid (Kojima et al., 2004).

B. The PGSHIN/pReflect-R system, is a two vector system that allows fluorescence quantification of siRNA based protein depletion. The knockdown construct is similar to pGSuper, and expresses soluble GFP and a hairpin siRNA under separate promoters. The reporter plasmid, p-Reflect-R, expresses a soluble DsRed protein from an mRNA transcript that also contains the 19nt shRNA target sequence between the stop codon and the poly-A tail. Control plasmids contain no target or express no hairpin siRNA. The plasmids are cotransfected, and the ratio of red to green fluorescence is used to determine knockdown.

A.

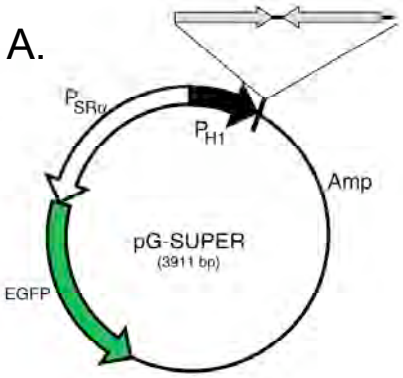

B.

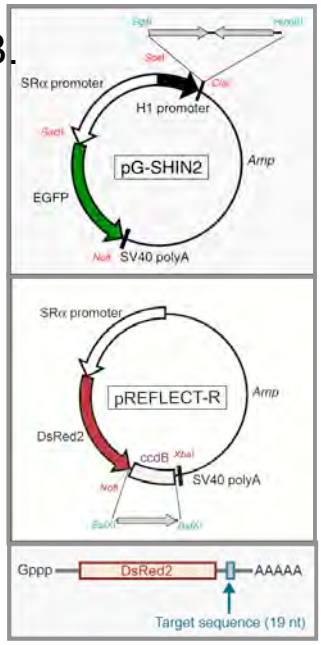

Knockdown

Reporter

System designed by Dr. Kojima, Borisy Laboratory

Figure 61 Determination of knockdown using pGSHIN/p-Reflect-R system.

1. 4 sets of cells are co-transfected with pGSHIN/p-Reflect-R plasmids for each target: p-Reflect-R (R) test/ pGSHIN (G) test, R test/G control, R control/G test, R control/G control. 2. The expected R:G ratio is determined by the formula shown. 3. The observed R:G ratio obtained from R test/ G test is divided by the expected ratio, generating the “knockdown index”. The lower the knockdown index, the higher knockdown.

1. Transfect all 4 combinations of test and control vectors

- **Rtest / Gtest**
- **Rctrl / Gtest**
- **Rtest / Gctrl**
- **Rctrl / Gctrl**

2. $$\frac{\frac{R_{test}}{G_{control}} \times \frac{R_{control}}{G_{test}}}{\frac{R_{control}}{G_{control}}} = \text{expected R/G} = \boxed{\frac{R_{test}}{G_{test}}}$$

3. $$\frac{\text{observed } R_{test}/G_{test}}{\text{expected } R_{test}/G_{test}} = \text{KD index}$$

$$\boxed{\downarrow \text{KD index} = \uparrow \text{KD}}$$

knockdown efficiency of shRNA targets using fluorescence microscopy rather than western blot analysis (Figure 60B). Briefly, the pReflect-R contains the DsRed2 protein with a copy of the shRNA target sequence inserted between the stop codon and the poly-A tail. Cells co-transfected with pG-SHIN2 and p-Reflect-R containing the same target sequence initially express soluble GFP and DsRed fluorescence. However, the DsRed fluorescence is quenched as the RNA expression is blocked by the expressed shRNA. Measuring the ratio of red: green fluorescence of the test targets, corrected by controls (p-Reflect-R test with pG-SHIN2 control vector, and p--R control vector with pG-SHIN2 test vector) leads to the calculation of a knockdown index that more easily and accurately predicts strength of gene knockdown (Figure 61). This system was employed for the Arp3 knockdown.

Design and control of siRNA experiments.

The siRNA experiments used several different controls to ensure that observed phenotypes corresponded to protein depletion rather than off-target effects. The controls include: the use of multiple target sequences, mismatch control siRNA vectors, rescue, suppression, and knockdown verification. Two unique target sequences were designed for p34, and six were later generated for the Arp3 siRNA experiments. As it is difficult to predict which targets will be most effective based on sequence alone, the selection of a larger number of targets improves the chances of obtaining a high knockdown efficiency on the first attempt. Additionally, observation of the same phenotype with separate targeting indicates that the effect is likely due to target gene

depletion, rather than an off target effect. siRNAs have been shown to be highly specific, with only a single nucleotide change needed to ablate their ability to target RNA for degradation. A two nucleotide change from the parent siRNA target is used in our controls, often in the form of a silent third codon mutation that does not change the coding sequence. These constructs are shown to be unique in the genome, and should have no ability to target, and should therefore demonstrate wild type phenotype. To demonstrate that the observed phenotype is due only to the target gene depletion, rescue with the full length gene (either silently mutagenized to be resistant to siRNA degradation or of another species with more than 2 nucleotide differing from the siRNA target) is performed. Restoration of wild type phenotype indicates that the observed phenotype is caused specifically by depletion of the target gene. The Stratagene Quick Change Site Directed Mutagenesis Kit is used to induce point mutations into the full length genes. Simultaneous transfection of cells with siRNA and rescue vector should suppress the silencing phenotype, unless there are additional off-target effects. Observation of phenotype by live cell phase/fluorescent imaging for phenotype and localization of WT protein, fixed cell immunofluorescent staining to demonstrate loss of target protein and/or restoration by rescue, and immunoblotting to detect the amount of remaining protein are employed as described elsewhere in the materials and methods.

7.12 Morphometric parameters and outgrowth assays.

Processes/neurites were defined as extension from the cell body greater than 2 times the length of the longest line through the cell body. Neurite outgrowth was examined on

poly-D/L-ornithine and laminin coated glass cover slips. Outgrowth was challenged at either immediately following transfection with the siRNA vector, or 72-96 hours following transfection. Cells challenged at 72-96 hours were examined 24 hours after plating to quantify process formation and length in the presence of reduced p34 protein levels. Cells challenged immediately after transfection were allowed to grow in the incubator for 72-96 hours, at which point they were fixed, stained with phalloidin, and examined under the microscope to determine their ability to maintain normal cell shape and/or processes with a dwindling supply of Arp2/3.

CHAPTER 8

REFERENCES

Abercrombie, M., J.E. Heaysman, and S.M. Pegrum. 1970. The locomotion of fibroblasts in culture. II. "RRuffling". *Exp Cell Res*. 60:437-44.

Abercrombie, M., J.E. Heaysman, and S.M. Pegrum. 1971. The locomotion of fibroblasts in culture. IV. Electron microscopy of the leading lamella. *Exp Cell Res*. 67:359-67.

Abramoff, M.D., P.J. Magelhaes, and S.J. Ram. 2004. Image Processing with ImageJ. *Biophotonics International*. 11:36-42.

Alberts, B. 2002. Molecular biology of the cell. Garland Science, New York. xxxiv, 1463, [86] pp.

Alberts, B. 2004. Essential cell biology. Garland Science, New York. 1 v. (various pagings) pp.

Argiro, V., M.B. Bunge, and M.I. Johnson. 1984. Correlation between growth form and movement and their dependence on neuronal age. *J Neurosci*. 4:3051-62.

Baum, B., and P. Kunda. 2005. Actin nucleation: spire - actin nucleator in a class of its own. *Curr Biol*. 15:R305-8.

Bentley, D., and A. Toroian-Raymond. 1986. Disoriented pathfinding by pioneer neurone growth cones deprived of filopodia by cytochalasin treatment. *Nature*. 323:712-5.

Bestman, J.E., R.C. Ewald, S.L. Chiu, and H.T. Cline. 2006. In vivo single-cell electroporation for transfer of DNA and macromolecules. *Nat Protoc*. 1:1267-72.

Borisy, G.G., and T.M. Svitkina. 2000. Actin machinery: pushing the envelope. *Curr Opin Cell Biol*. 12:104-12.

Borths, E.L., and M.D. Welch. 2002. Turning on the Arp2/3 complex at atomic resolution. *Structure (Camb)*. 10:131-5.

Bray, D. 1979. Mechanical tension produced by nerve cells in tissue culture. *J Cell Sci*. 37:391-410.

Bray, D. 1984. Axonal growth in response to experimentally applied mechanical tension. *Dev Biol*. 102:379-89.

Bray, D., and K. Chapman. 1985. Analysis of microspike movements on the neuronal growth cone. *J Neurosci*. 5:3204-13.

Bray, D., and P.J. Hollenbeck. 1988. Growth cone motility and guidance. *Annu Rev Cell Biol*. 4:43-61.

Bray, D., C. Thomas, and G. Shaw. 1978. Growth cone formation in cultures of sensory neurons. *Proc Natl Acad Sci U S A*. 75:5226-9.

Bridgman, P.C. 2002. Growth cones contain myosin II bipolar filament arrays. *Cell Motil Cytoskeleton*. 52:91-6.

Bridgman, P.C., and M.E. Dailey. 1989. The organization of myosin and actin in rapid frozen nerve growth cones. *J Cell Biol*. 108:95-109.

Bridgman, P.C., S. Dave, C.F. Asnes, A.N. Tullio, and R.S. Adelstein. 2001. Myosin IIB is required for growth cone motility. *J Neurosci*. 21:6159-69.

Brown, J., and P.C. Bridgman. 2003a. Role of myosin II in axon outgrowth. *J Histochem Cytochem*. 51:421-8.

Brown, M.E., and P.C. Bridgman. 2003b. Retrograde flow rate is increased in growth cones from myosin IIB knockout mice. *J Cell Sci*. 116:1087-94.

Brummelkamp, T.R., R. Bernards, and R. Agami. 2002. A system for stable expression of short interfering RNAs in mammalian cells. *Science*. 296:550-3.

Cajal, S. 1909. Histologie du système nerveux de l'homme et des vertébrés. Instituto "Ramón y Cajal", Madrid.

Cajal, S. 1967. The structure and connexions of neurons. Elsevier Publishing Co., London : New York. pp. 220-53 pp.

Chien, C.B., D.E. Rosenthal, W.A. Harris, and C.E. Holt. 1993. Navigational errors made by growth cones without filopodia in the embryonic Xenopus brain. *Neuron*. 11:237-51.

Clark, S.E., D.J. Moss, and D. Bray. 1983. Actin polymerization and synthesis in cultured neurones. *Exp Cell Res*. 147:303-14.

Clarke, E., and L.S. Jacyna. 1987. Nineteenth-century origins of neuroscientific concepts. University of California Press, Berkeley. 98-100. pp.

Conti, M.A., S. Even-Ram, C. Liu, K.M. Yamada, and R.S. Adelstein. 2004. Defects in cell adhesion and the visceral endoderm following ablation of nonmuscle myosin heavy chain II-A in mice. *J Biol Chem*. 279:41263-6.

Dent, E.W., and F.B. Gertler. 2003. Cytoskeletal dynamics and transport in growth cone motility and axon guidance. *Neuron*. 40:209-27.

Di Nardo, A., G. Cicchetti, H. Falet, J.H. Hartwig, T.P. Stossel, and D.J. Kwiatkowski. 2005. Arp2/3 complex-deficient mouse fibroblasts are viable and have normal

leading-edge actin structure and function. *Proc Natl Acad Sci U S A*. 102:16263-8.

Diefenbach, T.J., V.M. Latham, D. Yimlamai, C.A. Liu, I.M. Herman, and D.G. Jay. 2002. Myosin 1c and myosin IIB serve opposing roles in lamellipodial dynamics of the neuronal growth cone. *J Cell Biol*. 158:1207-17.

Evangelista, M., S. Zigmond, and C. Boone. 2003. Formins: signaling effectors for assembly and polarization of actin filaments. *J Cell Sci*. 116:2603-11.

Flanagan, L.A., J. Chou, H. Falet, R. Neujahr, J.H. Hartwig, and T.P. Stossel. 2001. Filamin A, the Arp2/3 complex, and the morphology and function of cortical actin filaments in human melanoma cells. *J Cell Biol*. 155:511-7.

Forscher, P., and S.J. Smith. 1988. Actions of cytochalasins on the organization of actin filaments and microtubules in a neuronal growth cone. *J Cell Biol*. 107:1505-16.

Fox, J.W., E.D. Lamperti, Y.Z. Eksioglu, S.E. Hong, Y. Feng, D.A. Graham, I.E. Scheffer, W.B. Dobyns, B.A. Hirsch, R.A. Radtke, S.F. Berkovic, P.R. Huttenlocher, and C.A. Walsh. 1998. Mutations in filamin 1 prevent migration of cerebral cortical neurons in human periventricular heterotopia. *Neuron*. 21:1315-25.

Gallo, G., and P.C. Letourneau. 2004. Regulation of growth cone actin filaments by guidance cues. *J Neurobiol*. 58:92-102.

Goldberg, D.J., and D.W. Burmeister. 1986. Stages in axon formation: observations of growth of Aplysia axons in culture using video-enhanced contrast-differential interference contrast microscopy. *J Cell Biol*. 103:1921-31.

Gournier, H., E.D. Goley, H. Niederstrasser, T. Trinh, and M.D. Welch. 2001. Reconstitution of human Arp2/3 complex reveals critical roles of individual subunits in complex structure and activity. *Mol Cell*. 8:1041-52.

Grzywa, E.L., A.C. Lee, G.U. Lee, and D.M. Suter. 2006a. High-resolution analysis of neuronal growth cone morphology by comparative atomic force and optical microscopy. *J Neurobiol*.

Grzywa, E.L., A.C. Lee, G.U. Lee, and D.M. Suter. 2006b. High-resolution analysis of neuronal growth cone morphology by comparative atomic force and optical microscopy. *J Neurobiol*. 66:1529-43.

Gupton, S.L., K.L. Anderson, T.P. Kole, R.S. Fischer, A. Ponti, S.E. Hitchcock-DeGregori, G. Danuser, V.M. Fowler, D. Wirtz, D. Hanein, and C.M. Waterman-Storer. 2005. Cell migration without a lamellipodium: translation of actin dynamics into cell movement mediated by tropomyosin. *J Cell Biol*. 168:619-31.

Haas, K., K. Jensen, W.C. Sin, L. Foa, and H.T. Cline. 2002. Targeted electroporation in Xenopus tadpoles in vivo--from single cells to the entire brain. *Differentiation*. 70:148-54.

Harborth, J., S.M. Elbashir, K. Bechert, T. Tuschl, and K. Weber. 2001. Identification of essential genes in cultured mammalian cells using small interfering RNAs. *J Cell Sci*. 114:4557-65.

Harrison, R.G. 1910. The outgrowth of the nerve fiber as a mode of protoplasmic movement. *J Exp Zool*. 9:787–848.

Hartwig, J.H., and P. Shevlin. 1986. The architecture of actin filaments and the ultrastructural location of actin-binding protein in the periphery of lung macrophages. *J Cell Biol*. 103:1007-20.

Hartwig, J.H., and T.P. Stossel. 1975. Isolation and properties of actin, myosin, and a new actinbinding protein in rabbit alveolar macrophages. *J Biol Chem*. 250:5696-705.

Heidemann, S.R., P. Lamoureux, and R.E. Buxbaum. 1990. Growth cone behavior and production of traction force. *J Cell Biol*. 111:1949-57.

Henley, J., and M.M. Poo. 2004. Guiding neuronal growth cones using Ca2+ signals. *Trends Cell Biol*. 14:320-30.

Higgs, H.N. 2001. Actin nucleation: nucleation-promoting factors are not all equal. *Curr Biol*. 11:R1009-12.

Higgs, H.N., and T.D. Pollard. 1999. Regulation of actin polymerization by Arp2/3 complex and WASp/Scar proteins. *J Biol Chem*. 274:32531-4.

Higgs, H.N., and T.D. Pollard. 2001. Regulation of actin filament network formation through ARP2/3 complex: activation by a diverse array of proteins. *Annu Rev Biochem*. 70:649-76.

Hinz, B., W. Alt, C. Johnen, V. Herzog, and H.W. Kaiser. 1999. Quantifying lamella dynamics of cultured cells by SACED, a new computer-assisted motion analysis. *Exp Cell Res*. 251:234-43.

Huang, M.E., J.L. Souciet, J.C. Chuat, and F. Galibert. 1996. Identification of ACT4, a novel essential actin-related gene in the yeast Saccharomyces cerevisiae. *Yeast*. 12:839-48.

Hudson, A.M., and L. Cooley. 2002. A subset of dynamic actin rearrangements in Drosophila requires the Arp2/3 complex. *J Cell Biol*. 156:677-87.

Invitrogen. 2007. BLOCK-iT™ RNAi Designer. Vol. 2007.

Jeng, R.L., and M.D. Welch. 2001. Cytoskeleton: actin and endocytosis--no longer the weakest link. *Curr Biol*. 11:R691-4.

Kalil, K., and E.W. Dent. 2005. Touch and go: guidance cues signal to the growth cone cytoskeleton. *Curr Opin Neurobiol*. 15:521-6.

Kerkhoff, E. 2006. Cellular functions of the Spir actin-nucleation factors. *Trends Cell Biol*. 16:477-83.

Kleinebrecht, J., J. Selow, and W. Winkler. 1982. The mouse mutant limb-deformity (ld). *Anat Anz*. 152:313-24.

Kojima, S., D. Vignjevic, and G.G. Borisy. 2004. Improved silencing vector co-expressing GFP and small hairpin RNA. *BioTechniques*. 36:74-9.

Kovar, D.R. 2006. Molecular details of formin-mediated actin assembly. *Curr Opin Cell Biol*. 18:11-7.

Lambert de Rouvroit, C., and A.M. Goffinet. 2001. Neuronal migration. *Mech Dev*. 105:47-56.

Lamoureux, P., R.E. Buxbaum, and S.R. Heidemann. 1989. Direct evidence that growth cones pull. *Nature*. 340:159-62.

Landis, S.C. 1983. Neuronal growth cones. *Annu Rev Physiol*. 45:567-80.

Letourneau, P.C. 1996. The cytoskeleton in nerve growth cone motility and axonal pathfinding. *Perspect Dev Neurobiol*. 4:111-23.

Lewis, A.K., and P.C. Bridgman. 1992. Nerve growth cone lamellipodia contain two populations of actin filaments that differ in organization and polarity. *J Cell Biol*. 119:1219-43.

Lin, C.H., E.M. Espreafico, M.S. Mooseker, and P. Forscher. 1996. Myosin drives retrograde F-actin flow in neuronal growth cones. *Neuron*. 16:769-82.

Lin, C.H., and P. Forscher. 1995. Growth cone advance is inversely proportional to retrograde F-actin flow. *Neuron*. 14:763-71.

Loisel, T.P., R. Boujemaa, D. Pantaloni, and M.F. Carlier. 1999. Reconstitution of actin-based motility of Listeria and Shigella using pure proteins. *Nature*. 401:613-6.

Luo, L. 2002. Actin cytoskeleton regulation in neuronal morphogenesis and structural plasticity. *Annu Rev Cell Dev Biol*. 18:601-35.

Ma, L., R. Rohatgi, and M.W. Kirschner. 1998. The Arp2/3 complex mediates actin polymerization induced by the small GTP-binding protein Cdc42. *Proc Natl Acad Sci U S A*. 95:15362-7.

Machesky, L.M., S.J. Atkinson, C. Ampe, J. Vandekerckhove, and T.D. Pollard. 1994. Purification of a cortical complex containing two unconventional actins from Acanthamoeba by affinity chromatography on profilin-agarose. *J Cell Biol*. 127:107-15.

Machesky, L.M., and R.H. Insall. 1998. Scar1 and the related Wiskott-Aldrich syndrome protein, WASP, regulate the actin cytoskeleton through the Arp2/3 complex. *Curr Biol*. 8:1347-56.

Machesky, L.M., E. Reeves, F. Wientjes, F.J. Mattheyse, A. Grogan, N.F. Totty, A.L. Burlingame, J.J. Hsuan, and A.W. Segal. 1997. Mammalian actin-related protein 2/3 complex localizes to regions of lamellipodial protrusion and is composed of evolutionarily conserved proteins. *Biochem J*. 328 (Pt 1):105-12.

Marsh, L., and P.C. Letourneau. 1984. Growth of neurites without filopodial or lamellipodial activity in the presence of cytochalasin B. *J Cell Biol*. 99:2041-7.

Mathur, J., N. Mathur, B. Kernebeck, and M. Hulskamp. 2003. Mutations in actin-related proteins 2 and 3 affect cell shape development in Arabidopsis. *Plant Cell*. 15:1632-45.

Medeiros, N.A., D.T. Burnette, and P. Forscher. 2006. Myosin II functions in actin-bundle turnover in neuronal growth cones. *Nat Cell Biol*. 8:215-26.

Mejillano, M.R., S. Kojima, D.A. Applewhite, F.B. Gertler, T.M. Svitkina, and G.G. Borisy. 2004. Lamellipodial versus filopodial mode of the actin nanomachinery: pivotal role of the filament barbed end. *Cell*. 118:363-73.

Michelot, A., C. Guerin, S. Huang, M. Ingouff, S. Richard, N. Rodiuc, C.J. Staiger, and L. Blanchoin. 2005. The Formin Homology 1 Domain Modulates the Actin Nucleation and Bundling Activity of Arabidopsis FORMIN1. *In* Plant Cell.

Mogilner, A., and G. Oster. 1996. Cell motility driven by actin polymerization. *Biophys J*. 71:3030-45.

Mullins, R.D., J.A. Heuser, and T.D. Pollard. 1998. The interaction of Arp2/3 complex with actin: nucleation, high affinity pointed end capping, and formation of branching networks of filaments. *Proc Natl Acad Sci U S A*. 95:6181-6.

Ng, J., and L. Luo. 2004. Rho GTPases regulate axon growth through convergent and divergent signaling pathways. *Neuron*. 44:779-93.

Nozumi, M., H. Nakagawa, H. Miki, T. Takenawa, and S. Miyamoto. 2003. Differential localization of WAVE isoforms in filopodia and lamellipodia of the neuronal growth cone. *J Cell Sci*. 116:239-46.

Pantaloni, D., R. Boujemaa, D. Didry, P. Gounon, and M.F. Carlier. 2000. The Arp2/3 complex branches filament barbed ends: functional antagonism with capping proteins. *Nat Cell Biol*. 2:385-91.

Pantaloni, D., C. Le Clainche, and M.F. Carlier. 2001. Mechanism of actin-based motility. *Science*. 292:1502-6.

Pollard, T.D., L. Blanchoin, and R.D. Mullins. 2000. Molecular mechanisms controlling actin filament dynamics in nonmuscle cells. *Annu Rev Biophys Biomol Struct*. 29:545-76.

Pollard, T.D., and G.G. Borisy. 2003. Cellular motility driven by assembly and disassembly of actin filaments. *Cell*. 112:453-65.

Quinlan, M.E., J.E. Heuser, E. Kerkhoff, and R.D. Mullins. 2005. Drosophila Spire is an actin nucleation factor. *Nature*. 433:382-8.

Ramón y Cajal, S. 1890. A quelle époque apparaissent les expansions des cellules nerveuses de la moelle épinè›re du poulet.

. *Anat Anz* 21:1-13.

Robinson, R.C., K. Turbedsky, D.A. Kaiser, J.B. Marchand, H.N. Higgs, S. Choe, and T.D. Pollard. 2001. Crystal structure of Arp2/3 complex. *Science*. 294:1679-84.

Rochlin, M.W., K. Itoh, R.S. Adelstein, and P.C. Bridgman. 1995. Localization of myosin II A and B isoforms in cultured neurons. *J Cell Sci*. 108 (Pt 12):3661-70.

Rogers, S.L., U. Wiedemann, N. Stuurman, and R.D. Vale. 2003. Molecular requirements for actin-based lamella formation in Drosophila S2 cells. *J Cell Biol*. 162:1079-88.

Schaefer, A.W., N. Kabir, and P. Forscher. 2002. Filopodia and actin arcs guide the assembly and transport of two populations of microtubules with unique dynamic parameters in neuronal growth cones. *J Cell Biol*. 158:139-52.

Schober, J.M., Y.A. Komarova, O.Y. Chaga, A. Akhmanova, and G.G. Borisy. 2007. Microtubule-targeting-dependent reorganization of filopodia. *J Cell Sci*. 120:1235-44.

Schumacher, N., J.M. Borawski, C.B. Leberfinger, M. Gessler, and E. Kerkhoff. 2004. Overlapping expression pattern of the actin organizers Spir-1 and formin-2 in the developing mouse nervous system and the adult brain. *Gene Expr Patterns*. 4:249-55.

Sellers, J.R. 2000. Myosins: a diverse superfamily. *Biochim Biophys Acta*. 1496:3-22.

Shlomovitz, R., and N.S. Gov. 2007. Membrane waves driven by actin and Myosin. *Phys Rev Lett*. 98:168103.

Small, J.V., G. Isenberg, and J.E. Celis. 1978. Polarity of actin at the leading edge of cultured cells. *Nature*. 272:638-9.

Smith, C.L. 1998. Cultures of chick peripheral ganglia. *In* Culturing Nerve Cells. G. Banker and K. Goslin, editors. MIT Press, Cambridge, MA. 261-287.

Smith, S.J. 1988. Neuronal cytomechanics: the actin-based motility of growth cones. *Science*. 242:708-15.

Steketee, M.B., and K.W. Tosney. 2002. Three functionally distinct adhesions in filopodia: shaft adhesions control lamellar extension. *J Neurosci*. 22:8071-83.

Stossel, T.P., J. Condeelis, L. Cooley, J.H. Hartwig, A. Noegel, M. Schleicher, and S.S. Shapiro. 2001. Filamins as integrators of cell mechanics and signalling. *Nat Rev Mol Cell Biol*. 2:138-45.

Stossel, T.P., and J.H. Hartwig. 1975. Interactions between actin, myosin, and an actin-binding protein from rabbit alveolar macrophages. Alveolar macrophage myosin Mg-2+-adenosine triphosphatase requires a cofactor for activation by actin. *J Biol Chem*. 250:5706-12.

Stossel, T.P., and J.H. Hartwig. 2003. Filling gaps in signaling to actin cytoskeletal remodeling. *Dev Cell*. 4:444-5.

Strasser, G.A., N.A. Rahim, K.E. VanderWaal, F.B. Gertler, and L.M. Lanier. 2004. Arp2/3 is a negative regulator of growth cone translocation. *Neuron*. 43:81-94.

Suter, D.M., and P. Forscher. 2000. Substrate-cytoskeletal coupling as a mechanism for the regulation of growth cone motility and guidance. *J Neurobiol*. 44:97-113.

Svitkina, T.M., and G.G. Borisy. 1999. Arp2/3 complex and actin depolymerizing factor/cofilin in dendritic organization and treadmilling of actin filament array in lamellipodia. *J Cell Biol*. 145:1009-26.

Svitkina, T.M., E.A. Bulanova, O.Y. Chaga, D.M. Vignjevic, S. Kojima, J.M. Vasiliev, and G.G. Borisy. 2003. Mechanism of filopodia initiation by reorganization of a dendritic network. *J Cell Biol*. 160:409-21.

Svitkina, T.M., A.B. Verkhovsky, K.M. McQuade, and G.G. Borisy. 1997. Analysis of the actin-myosin II system in fish epidermal keratocytes: mechanism of cell body translocation. *J Cell Biol*. 139:397-415.

Tilney, L.G., E.M. Bonder, and D.J. DeRosier. 1981. Actin filaments elongate from their membrane-associated ends. *J Cell Biol*. 90:485-94.

Tosney, K.W., and N.K. Wessells. 1983. Neuronal motility: the ultrastructure of veils and microspikes correlates with their motile activities. *J Cell Sci*. 61:389-411.

Tseng, Y., K.M. An, O. Esue, and D. Wirtz. 2004. The bimodal role of filamin in controlling the architecture and mechanics of F-actin networks. *J Biol Chem*. 279:1819-26.

Tseng, Y., and D. Wirtz. 2004. Dendritic branching and homogenization of actin networks mediated by arp2/3 complex. *Phys Rev Lett*. 93:258104.

Tullio, A.N., P.C. Bridgman, N.J. Tresser, C.C. Chan, M.A. Conti, R.S. Adelstein, and Y. Hara. 2001. Structural abnormalities develop in the brain after ablation of the gene encoding nonmuscle myosin II-B heavy chain. *J Comp Neurol*. 433:62-74.

Verkhovsky, A.B., and G.G. Borisy. 1993. Non-sarcomeric mode of myosin II organization in the fibroblast lamellum. *J Cell Biol*. 123:637-52.

Verkhovsky, A.B., T.M. Svitkina, and G.G. Borisy. 1995. Myosin II filament assemblies in the active lamella of fibroblasts: their morphogenesis and role in the formation of actin filament bundles. *J Cell Biol*. 131:989-1002.

Vignjevic, D., S. Kojima, Y. Aratyn, O. Danciu, T. Svitkina, and G.G. Borisy. 2006. Role of fascin in filopodial protrusion. *J Cell Biol*. 174:863-75.

Vignjevic, D., D. Yarar, M.D. Welch, J. Peloquin, T. Svitkina, and G.G. Borisy. 2003. Formation of filopodia-like bundles in vitro from a dendritic network. *J Cell Biol*. 160:951-62.

Volkmann, N., K.J. Amann, S. Stoilova-McPhie, C. Egile, D.C. Winter, L. Hazelwood, J.E. Heuser, R. Li, T.D. Pollard, and D. Hanein. 2001. Structure of Arp2/3 complex in its activated state and in actin filament branch junctions. *Science*. 293:2456-9.

Wallar, B.J., and A.S. Alberts. 2003. The formins: active scaffolds that remodel the cytoskeleton. *Trends Cell Biol*. 13:435-46.

Watanabe, N., and T.J. Mitchison. 2002. Single-molecule speckle analysis of actin filament turnover in lamellipodia. *Science*. 295:1083-6.

Welch, M.D., A.H. DePace, S. Verma, A. Iwamatsu, and T.J. Mitchison. 1997. The human Arp2/3 complex is composed of evolutionarily conserved subunits and is localized to cellular regions of dynamic actin filament assembly. *J Cell Biol*. 138:375-84.

Wiesner, S., E. Helfer, D. Didry, G. Ducouret, F. Lafuma, M.F. Carlier, and D. Pantaloni. 2003. A biomimetic motility assay provides insight into the mechanism of actin-based motility. *J Cell Biol*. 160:387-98.

Winter, D., A.V. Podtelejnikov, M. Mann, and R. Li. 1997. The complex containing actin-related proteins Arp2 and Arp3 is required for the motility and integrity of yeast actin patches. *Curr Biol*. 7:519-29.

Winter, D.C., E.Y. Choe, and R. Li. 1999. Genetic dissection of the budding yeast Arp2/3 complex: a comparison of the in vivo and structural roles of individual subunits. *Proc Natl Acad Sci U S A*. 96:7288-93.

Wu, D.Y., and D.J. Goldberg. 1993. Regulated tyrosine phosphorylation at the tips of growth cone filopodia. *J Cell Biol*. 123:653-64.

Wu, D.Y., L.C. Wang, C.A. Mason, and D.J. Goldberg. 1996. Association of beta 1 integrin with phosphotyrosine in growth cone filopodia. *J Neurosci*. 16:1470-8.

Wylie, S.R., and P.D. Chantler. 2001. Separate but linked functions of conventional myosins modulate adhesion and neurite outgrowth. *Nat Cell Biol*. 3:88-92.

Wylie, S.R., and P.D. Chantler. 2003. Myosin IIA drives neurite retraction. *Mol Biol Cell*. 14:4654-66.

Wylie, S.R., P.J. Wu, H. Patel, and P.D. Chantler. 1998. A conventional myosin motor drives neurite outgrowth. *Proc Natl Acad Sci U S A*. 95:12967-72.

Yamada, K.M., B.S. Spooner, and N.K. Wessells. 1970. Axon growth: roles of microfilaments and microtubules. *Proc Natl Acad Sci U S A*. 66:1206-12.

Yamada, K.M., B.S. Spooner, and N.K. Wessells. 1971. Ultrastructure and function of growth cones and axons of cultured nerve cells. *J Cell Biol*. 49:614-35.

Yamaguchi, H., M. Lorenz, S. Kempiak, C. Sarmiento, S. Coniglio, M. Symons, J. Segall, R. Eddy, H. Miki, T. Takenawa, and J. Condeelis. 2005. Molecular mechanisms of invadopodium formation: the role of the N-WASP-Arp2/3 complex pathway and cofilin. *J Cell Biol*. 168:441-52.

Zallen, J.A., Y. Cohen, A.M. Hudson, L. Cooley, E. Wieschaus, and E.D. Schejter. 2002. SCAR is a primary regulator of Arp2/3-dependent morphological events in Drosophila. *J. Cell Biol.* 156:689-701.

Zand, M.S., and G. Albrecht-Buehler. 1989. What structures, besides adhesions, prevent spread cells from rounding up? *Cell Motil Cytoskeleton*. 13:195-211.

Zigmond, S.H. 2004. Formin-induced nucleation of actin filaments. *Curr Opin Cell Biol*. 16:99-105.

Zigmond, S.H., M. Evangelista, C. Boone, C. Yang, A.C. Dar, F. Sicheri, J. Forkey, and M. Pring. 2003. Formin leaky cap allows elongation in the presence of tight capping proteins. *Curr Biol*. 13:1820-3.